SCALABLE TECHNOLOGIES TO CONTROL LIQUID WETTING AND ADHESION ON FIBER BASED SUBSTRATES

A Dissertation
Presented to
The Academic Faculty

by

Lu Jiang

In Partial Fulfillment
Of the Requirements for the Degree
Doctor of Philosophy in the
School of Chemical and Biomolecular Engineering

Georgia Institute of Technology
August 2017

SCALABLE TECHNOLOGIES TO CONTROL LIQUID WETTING AND ADHESION ON FIBER BASED SUBSTRATES

Approved by:

Dr. Dennis W. Hess, Co-Advisor
School of Chemical and Biomolecular Engineering
Georgia Institute of Technology

Dr. Yunlin Deng
School of Chemical and Biomolecular Engineering
Georgia Institute of Technology

Dr. Victor Breedveld, Co-Advisor
School of Chemical and Biomolecular Engineering
Georgia Institute of Technology

Dr. Meisha L. Shofner
School of Materials Science and Engineering
Georgia Institute of Technology

Dr. J. Carson Meredith
School of Chemical and Biomolecular Engineering
Georgia Institute of Technology

Date Approved: July 14th, 2017

ACKNOWLEDGEMENTS

First and foremost, I would like to thank my advisors Dr. Dennis W. Hess and Dr. Victor Breedveld, for their constant support of not only my work, but more importantly my ideas. There was never a point during my time at Georgia Tech where I did not feel that I could stop by their office and sort out my problems. I will forever be grateful of the knowledge and expertise that I have gained from their advising. I would also like to thank my committee members, Dr. Carson Meredith, Dr. Yulin Deng and Dr. Meisha Shofner for their help both during and after our committee meetings.

Thanks to the Hess and Breedveld group members, Dr. Zhenguan Tang, Dr. Lester Li, Dr. Linkun Xie, Dr. Won Tae Choi, Dr. Cornelia Rosu and Dr. Haisheng Lin for listening to my problems, and lending a helping hand whenever I need it. Special thanks to Dr. Zhenguan Tang, who is my loving husband now, for giving me a lot of helpful suggestions when I was struggling with my research. I was very fortunate to have been the mentor of many talented hardworking undergraduates. Rahmat M. Clinton, Kevin J. Park-Lee, Eliott J. Orzan and Hanyang Li, thanks for putting up with me and helping me to develop as a leader.

I would like to thank Georgia Tech Renewable Bioproducts Institute (RBI) for funding support. Finally, I would like to especially thank my family and my friends for their unwavering support of my desire to get a PhD.

TABLE OF CONTENTS

LIST OF TABLES

LIST OF FIGURES

SUMMARY

As a biodegradable, inexpensive and universally accessible material used in packaging, printing and cleaning, paper has been explored by many researchers for future applications in fields such as microfluidic devices, medical testing strips, liquid packaging and disposable medical apparel. However, the hydrophilic and oleophilic nature of paper often limits its use in these potential applications. Superamphiphobicity is defined by water and oil contact angles of > 150° and requires the specific combination of low surface energy and hierarchical structures. The existing methods reported in industry and academia for fabricating surfaces with extreme liquid repellency often involve sophisticated processes, loss of mechanical strength, lack of quantification of mechanical durability of the surface or failure to repel liquids with extremely low surface tension (lower than 27.5 mN/m (n-hexadecane)).

While superhydrophobic paper surfaces have been fabricated by several research groups, the oleophobicity of paper remains hard to attain and only a few groups have achieved superamphiphocity on paper surfaces. The paper surfaces are usually formed with nanoparticle incorporation, which may cause adhesion problems between the coating and the surface. The superamphiphobic paper surfaces previously reported by our group used a solvent exchange process, which significantly reduced paper strength and therefore limited its practical applications. In addition, all test liquids were found to be sticky on the surface fabricated with this method. None of the studies on superamphiphobic paper surfaces have reported repellency towards liquids with surface tension lower than that of hexadecane or resulted in roll off surfaces. Therefore, insights

into the critical design parameters involved in the formation of superamphiphobic fiber based surfaces such as paper and investigation of superamphiphobic papermaking techniques that are simple, cost effective, do not degrade bulk mechanical properties and are easy to scale up would greatly facilitate consumer applications.

In this thesis, we explored how wetting properties change with surface chemistry and the topology of the fiber network through controlled plasma etching with combined coating techniques and pulp pretreatment (refining, debonder addition). Commercially available debonders containing a quaternary ammonium surfactant were used to remove fines generated during pulp refining to attain a porous surface with thin fibers. After an oxygen plasma treatment, a hierarchical structure with both micro- and nano-scale roughness was generated on paper surfaces. Finally, immersion in a fluorosilane solution created a coating that resulted in a highly amphiphobic paper surface. The liquid repellency of the surface is close to that of the sumperamphiphobic paper reported by our group, but a more environmentally benign process was used that generated a mechanically stronger product comparable to copy paper. This is the first time that debonding agents have been used to alter the paper structure to establish anti-wetting properties. A detailed discussion of the factors that control the wetting of fiber-based materials (specifically for paper) was offered.

Based on this improved understanding of the design mechanism for superamphiphobic surfaces on paper, we combined the plasma etch process with the deposition of an extremely thin film to vary the micro- and nano-scale roughness systematically. This allowed the investigation of possible synergistic effects without interference from variations brought by chemical modification. This approach minimizes

the cost and material waste, improves the mechanical strength, and has yielded the best liquid repellency on paper surfaces that has been reported to date.

Applying the same fundamental knowledge gained from studies of wetting control on paper, stainless steel meshes with unique wetting properties for oil-water separation have been created. Hydrophilic/oleophobic stainless steel (SS) meshes were fabricated via a one-step solution-based coating method using methyltrimethoxysilane (MTMS). The mesh dimensions were varied to study their effect on wettability and separation efficiency. The coated mesh allows water fluxes as high as 7.16×10^4 $L \cdot m^{-2} \cdot h^{-1}$, with water recovery up to 91.1 % and separation efficiency higher than 99.9 % solely driven by gravity. Compared with existing oil-water separation units, this filter system is more environmentally friendly and suitable for drinking water treatment, since the coating does not contain fluorine. The result of dynamic sand impact tests showed that the coated surface is resilient towards mechanical impact; even with attached sand particles, the mesh still functioned efficiently.

Numerous studies have been published on creating hydrophobic or even amphiphobic surfaces on materials including metal, glass, polymer sheet, fabric, wood, and paper. However, researchers all employ different test conditions and equipment; a comprehensive suite of well-defined mechanical tests is missing. No group has evaluated the mechanical durability among different kind of liquid repellent surfaces under the same mechanical test conditions. More direct comparison between some major types of coating with standardized methods is important to understand the weakness of each method and tailor future applications for these functional surfaces. In the final chapter of this thesis, paper and glass slides were used as substrates, and liquid repellent coatings

were applied to the surfaces through various modification processes. Wetting properties were compared under tape peeling, dynamic impact, pressing, rotary abrasion and bending tests.

CHAPTER 1

INTRODUCTION

While the fabrication of superhydrophobic surfaces has been studied in great detail over the past decades, creating superamphiphobic surfaces that also are highly oil repellent remains a challenge. Despite the advances in rendering rigid inorganic substrate super liquid repellent through sophisticated fabrication techniques, reports on fiber based porous superamphiphobic surfaces are limited. Successful fabrication of superior liquid repellent surfaces on fiber based products like paper, will make possible cheap and "green" materials for food packaging, microfluidic devices and self-cleaning surfaces. However, most of the existing methods are often associated with sophisticated process or affect the bulk properties of the substrate, and thus inhibit products' general use. The primary objective of this thesis is to fabricate mechanically robust liquid repellent surfaces on fiber based material. To set the stage for studies to achieve this goal, background knowledge on surface energy and wetting, mechanism of fabricating superamphiphobic surfaces, existing oil-water separation materials and mechanical durability evaluation methods are presented in the following sections.

1.1 Surface Energy and Wetting

The topic of wetting has received tremendous interest from both fundamental and applied points of view. [1-8] The wetting of a liquid on a surface is determined by the surface energy of both the liquid and the solid substrate. The surface energy quantifies the disruption of intermolecular bonds that occur when new surface is created.

Specifically, it is defined as the work needed to generate new surface area and has units of J/m^2or N/m. High surface energy solid materials include metals and inorganic compounds such as oxides, silicates and nitrides, while low energy materials are mainly organic compounds including polymers. Fluorinated materials, such as polytetrafluoroethylene, are known to have the lowest surface energy due to the high electronegativity of F in C-F bonds, which lead to a reduced dispersive part of the surface energy. [6,9,10] Other factors such as polarizability and local attractive force may also have contributed to the extreme surface properties of fluorinated compounds.

The surface energy of a liquid is usually referred to as surface tension (surface energy relative to air). As a general rule, the greater the proportion of polar groups in a molecule, the stronger the attractive intermolecular forces. For example, water has high surface tension compared to oils due to its large proportion of O-H groups. The strongly attractive intermolecular forces give rise to a tendency to form droplets on a surface; as a result, hydrophobicity is generally easier to achieve than oleophobicity.

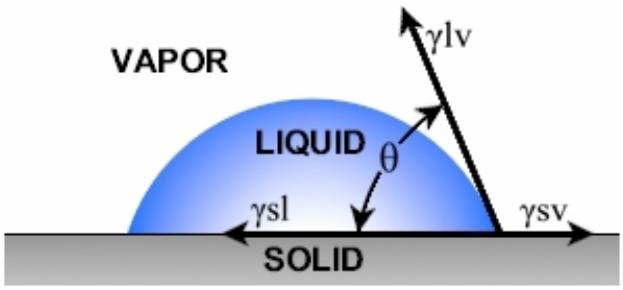

Figure 1.1: Droplet of liquid deposited on a flat surface (Ramehart.com).

From a microscopic point of view, the apparent contact angle is often used to evaluate surface wettability. For smooth surfaces, the apparent contact angle is an equilibrium angle calculated by Young's equation, which represents a force balance on the three-phase contact line:

$$cos\theta_{eq} = \frac{\gamma_{sv} - \gamma_{sl}}{\gamma_{lv}} \qquad (1.1)$$

where $\gamma_{sv}, \gamma_{sl}, \gamma_{lv}$ refer to the surface tensions at the solid-vapor, solid-liquid and liquid-vapor interfaces, respectively (Figure 1.1). It must be noted that even the highest water contact angles will not exceed 125°- 130° for flat, homogeneous surfaces, irrespective of the surface chemistry. [11] Intrinsic properties of materials alone are therefore not enough to achieve high contact angles for all liquids and this is where modification of the physical surface structure comes into play. Numerous studies have reported improved wetting properties on specially structured or roughened surfaces. [12-14] The most recognized models for predicting wetting phenomena on a rough surface are the Wenzel and Cassie-Baxter models.

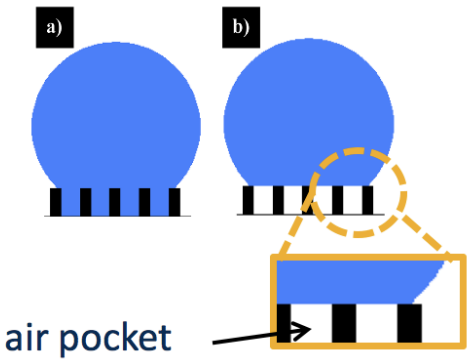

Figure 1.2: Droplet of liquid deposited on a rough surface in the (a) Wenzel state and (b) Cassie-Baxter states. [11]

Specific application of the two models depends on whether the solid-liquid contact area is continuous or discontinuous (Figure 1.2). When the liquid droplet is fully in contact with a rough surface, it is said to be in the Wenzel state and its apparent contact angle can be calculated by introducing a roughness factor r into Young's equation:

$$\cos\theta_W = r \cdot cos\theta_{eq} \tag{1.2}$$

Here, the roughness ratio is defined as the specific contact area divided by the projected area, and θ_W is the apparent Wenzel contact angle of the liquid on the surface. According to this equation, if the surface is hydrophilic/oleophilic (contact angle smaller than 90°), roughening the surface will make it more hydrophilic/oleophilic. However, if the surface is hydrophobic/oleophobic, roughening the surface will make it more liquid repellent.

In the other wetting scenario shown in Figure 1.2, the liquid droplet is supported by air pockets trapped between the surface asperities. This type of inhomogeneous wetting is described by the Cassie-Baxter model:

$$cos\theta_{CB} = \emptyset_s\left(1 + cos\theta_{eq}\right) - 1 \tag{1.3}$$

In this case, the fraction of the solid in contact with the liquid $\emptyset_s$, is introduced into Young's equation. According to this model, it is possible to achieve an apparent contact angle of liquid greater than 90° even with an equilibrium contact angle below 90°. To attain high liquid contact angles on a surface, the surface must be able to suspend the droplet in the Cassie-Baxter state.

Hysteresis is another important parameter needed to fully describe the wetting behavior on surfaces. Instead of having a fixed contact angle, a liquid droplet can actually exhibit a range of contact angles on the surface where the largest and smallest values are called advancing and receding contact angle respectively. Hysteresis is the difference between these two angles and describes the adhesion of liquids to the substrate. Tilting the substrate and adding/removing liquid volume are two major methods to determine the contact angle hysteresis (Figure 1.3). Another well recognized method to describe the liquid adhesion on surface is roll-off angle measurement which points out the tilting angle at which a liquid drop starts to roll off the surface.

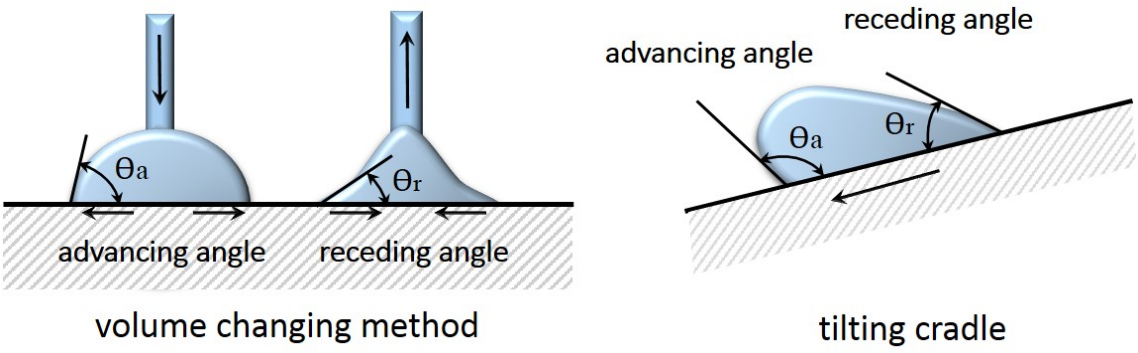

Figure 1.3: Measurements of contact angle hysteresis (weistron.com).

1.2 Superamphiphobic Surfaces on Fiber-Based Materials

Definition and Theories

Because of their promising application in many fields, superhydrophobic and superoleophobic surfaces (with static contact angles greater than 150°) have received

tremendous attention over the past decades. [2,11,12,15-18] This kind of super non-wetting surface has been referred to as superamphiphobic. While there is still no widely accepted definition of superamphiphobicity, most publications use this term to refer to surfaces that display extremely high repellency towards water and low surface tension oils. [19,20] Another term that people are apt to confuse with "superamphiphobic" is "superomniphobic" which instead define a surface that can repel virtually any liquid including water, oils and alcohols. [21,22] The lack of definition of well accepted standard test liquids is another reason for the controversial definition of "superamphiphobic". Some common liquids used are water, diiodomethane, and hexadecane, while other liquids such as soybean oil, peanut oil, olive oil, rapeseed oil or even coffee and milk are sometimes employed. [20,23-31]

As mentioned in the previous section, oleophobicity is more difficult to achieve on a surface than hydrophobicity because of the relatively low surface tension of oils (non-polar liquids). Not only are a low energy surface and dual-scale roughness needed, but so-called reentrant surface structures where the sidewalls of the structure are sloped inward to create an overhang profile are also critical for achieving superoleophobicity (Figure 1.4). [12]

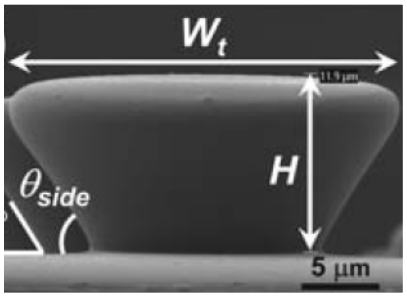

Figure 1.4: Reentrant structure fabricated on PDMS. [32]

Tuteja's group has given a detailed discussion on why surfaces possessing re-entrant structure ($\psi < 90°$) are necessary for establishing extremely high liquid apparent contact angles (see Figure 1.5a and b). [33] To support their hypothesis, they fabricated two different families of structures: randomly-deposited electrospun fiber mat and precisely fabricated "microhoodoo" surfaces on Si wafers that both possess reentrant texture. By careful engineering of reentrant curvature and solid surface energy, they were able to achieve extremely high repellency towards a wide range of polar and nonpolar liquids on the surfaces.

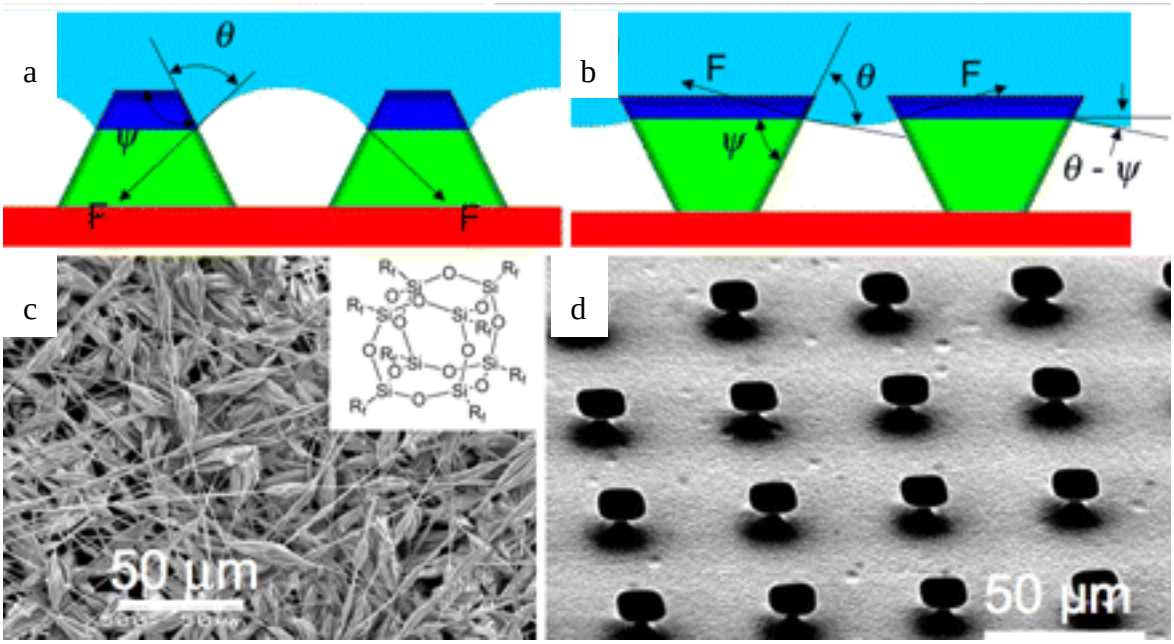

Figure 1.5: (a,b) Schematic diagrams illustrating possible liquid-vapor interfaces on two different surfaces having the same solid surface energy and the same equilibrium contact angle (θ), but different geometric angles (ψ). (c) an SEM micrograph of an electrospun surface containing 44.4 wt% fluorodecyl POSS and possessing the beads-on-strings morphology. The inset shows the molecular structure of fluorodecyl POSS molecules. The alkyl chains (Rf) have the molecular formula $-CH_2CH_2(CF_2)_7CF_3$. (d) an SEM micrograph of a microhoodoo structure on Si wafer surface. The samples are viewed from an oblique angle of 30°. [33]

Compared to rigid inorganic surfaces with finely constructed cleanroom-fabricated structures, cellulose-based paper naturally has reentrant structures. From the SEM images of Figure 1.6a we can see that the bottom half of cylindrical fibers can serve as reentrant structures. Paper has many merits over other materials as a superamphiphobic substrate, such as good biodegradability, low cost and worldwide availability. Achieving super liquid repellency on paper substrates would offer numerous potential applications in consumer fields such as liquid and food packaging (see Figure 1.6b) and disposable medical gowns (Figure 1.6c).

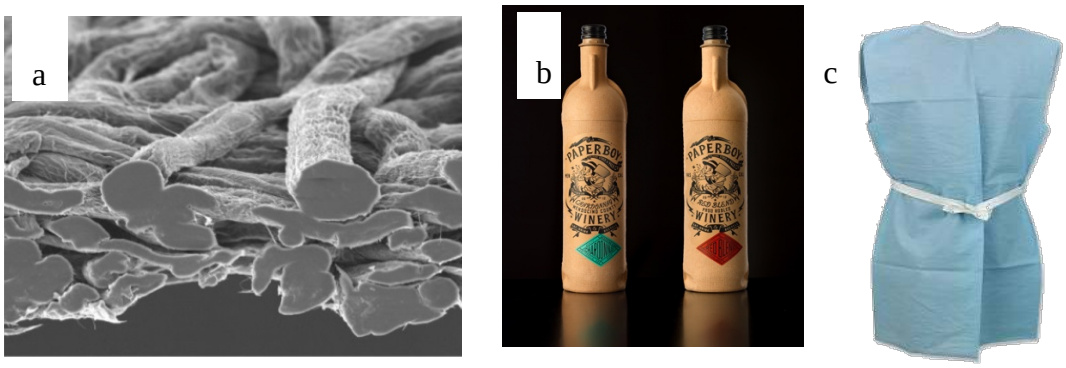

Figure 1.6: Cross section of softwood kraft fiber (photo from RBI) (b) fully recyclable, molded-pulp wine bottle (greenerpackage.com) (c) disposable medical gowns (medical-supplies-equipment-company.com).

In order to investigate wetting on fiber-based surfaces, the model of Cassie-Baxter can be used with some modification: [34-36]

$$cos\theta^* = \frac{D(\pi-\theta_{eq})}{L} cos\theta_{eq} + \frac{D}{L} sin\theta_{eq} - 1 \qquad (1.4)$$

In Equation 1.4, the apparent contact angle of the liquid is determined by the inter-fiber spacing *L*, the fiber diameter *D* and equilibrium contact angle θ_{eq}. If the *L/D* ratio can be varied, then the apparent contact angle of any liquid can be altered accordingly. With the

appropriate increase in *L/D* ratio, the apparent contact angles of water and oils can potentially reach 150°, which meets the superamphiphobic definition. However, unlike metal meshes and woven fabrics, cellulose based paper does not have a well-defined structure. Special treatment needs to be applied during the manufacturing process to establish an optimal (average) *L/D* ratio for corresponding coatings on fibers. Average wood fibers have diameters between 10 and 20 μm; if only the value of inter-fiber spacing *L* is increased, the paper would be far too porous for general application. Thus the *L/D* ratio should be increased through both reducing *D* and enlarging *L*.

Despite the research progress in fabricating superhydrophobic paper, achieving superoleophobicity remains a challenge. Although paper surfaces exhibit oil and water contact angles greater than 150° have been reported through careful engineering of surface structure, process scalability and preservation of the mechanical strength and stability of the product are non-trivial issues that need to be solved. The production process must be cheap and easy for factory scale-up if wide application of paper as food packaging or medical testing strips is desired. Especially for paper use in packaging, paper strength and surface coating stability are critical for product reliability due to the weight contained in the paper along with the frequent bending and friction experienced during use.

Existing Fabrication Techniques

As discussed in the previous section, both surface roughness and surface chemistry are crucial for the fabrication of superamphiphobic surfaces. Chu *et al.* classified the existing fabrication techniques into three categories (Figure 1.7) according

to the sequence of surface roughing and functionalization with low surface energy coating materials (usually fluorinated chemicals). [19] Some representative techniques for fabricating superamphiphobic fiber-based surfaces will be discussed in this section.

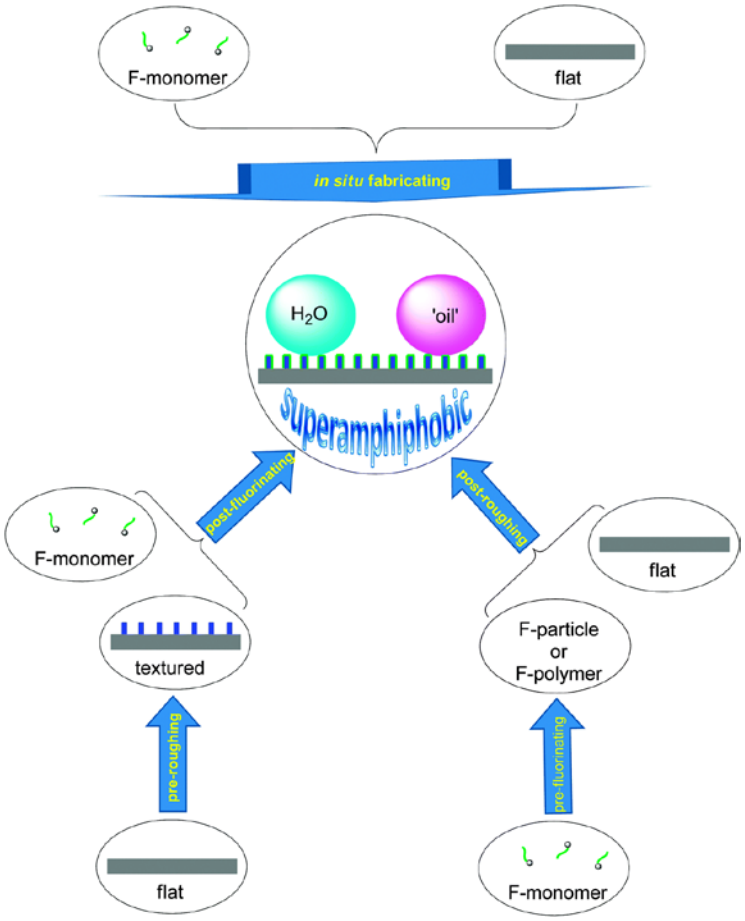

Figure 1.7: Three strategies towards the fabrication of superamphiphobic surfaces: pre-roughnening + post-fluorination; pre-fluorination + post-roughening; and one-pot *in situ* fabrication. [19]

One of the most frequently used methods to create superamphiphobic surfaces is spray or immersion coating with fluorinated nanoparticles or nanotubes (Figure 1.8). [37,38] Although superamphiphobic surfaces result from such procedures, mechanical

stability is generally compromised due to inadequate bonding between nanoparticles and substrates. Also, the morphology of the surface is not well-controlled during multiple spraying steps. In addition, many studies have reported adverse effects of nanoparticles on respiratory, cardiovascular and nervous systems. [39-41]

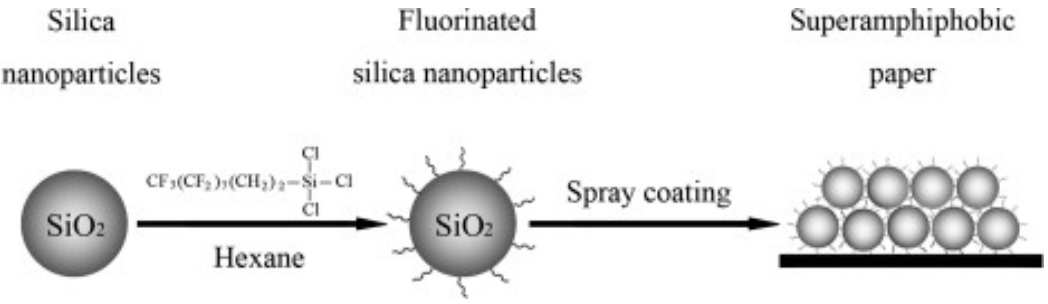

Figure 1.8: Scheme illustration of the preparation of a superamphiphobic paper. [37]

Zhou *et al.* have successfully prepared a superamphiphobic fabric by particle free polymer coating (Figure 1.9). [42] Their work is the first example of fabricating superamphiphobic fabric using a particle-free coating method, where the surface roughness was generated by the coating made with a specific solvent. However, without the suitable microscale roughness brought by the conventional fabric fibers, the method did not work as well on either paper or glass slides. Another method to create reentrant structures that achieve superamphiphobicity is electrospinning. [33,43,44] However, the resulting fibers typically lack sufficient strength for practical applications and the mechanical adhesion between the fibers and substrate requires further improvement to withstand frequent handling or other mechanical stresses.

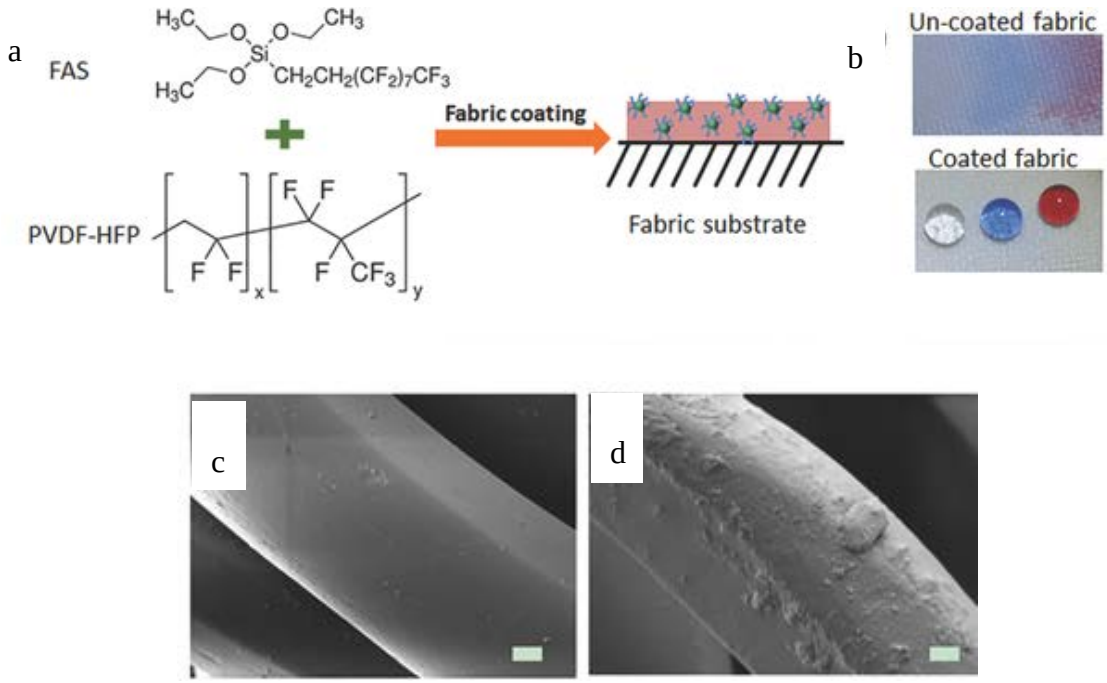

Figure 1.9: a) Chemical structures of coating materials and procedure for coating treatment, b) water, olive oil, and silicone oil drops on the uncoated fabric and the coated fabric (10 μL each, and the dyes in the droplets showed no influence on the contact angles). c) SEM images of polyester fiber uncoated and (d) coated in acetone-based coating solution (scale bar = 2 μm). [42]

An alternative approach to establishing surface roughness is the use of plasma etching. This technique has been used for decades to selectively remove the amorphous phase of a material, leaving behind the crystalline segments. [34,45-47] In our group, we have exposed paper surfaces to an oxygen plasma to uncover nanoscale roughness on cellulose fibers (Figure 1.10). [48,49] This approach is not subject to adhesion problems between substrate and nanoparticles, because the roughness is revealed in the cellulose structure by selective etching, thereby taking advantage of the inherently stable structure of this renewable material. Removal of material during plasma etching also enhances the paper porosity which reduces the liquid-solid contact area.

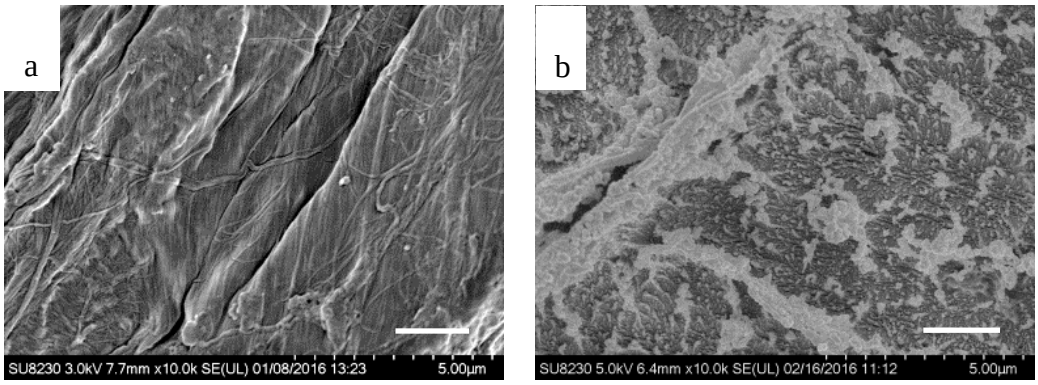

Figure 1.10: Fiber surface before and after oxygen plasma etch. The scale bars represent 2 µm.

Morphology changes after plasma etching do not impart liquid repellency to paper until a low surface energy material is applied to the surface. Application can be achieved via many techniques such as dip coating (brief liquid exposure), [35,50] solution-immersion method, [51-53] spray coating, [37,54] electrodeposition, [55,56] spin coating [57,58] and vapor deposition. [59,60] Among these, dip coating and solution-immersion are the simplest but usually require large amounts of coating solution. Spray coating also uses large volumes of liquids (although some of this can be recycled), while electrodeposition is time consuming and can result in contamination from the solutions employed. Spin coating is inherently a batch process, and electrospinning produces low strength nanofibers with adhesion concerns analogous to those of spray coating. Vapor deposition has few requirements for either the substrate or the coating material, and high-purity, high-density films can be formed rapidly, although this approach generally requires a vacuum system and substrate heating. [61] The ability to cover large areas readily makes vapor deposition an attractive technology for mass production. Use of vapor deposition for film formation on paper does not cause the surface to buckle or warp

which may be encountered when washing and drying processes are invoked. Although vapor deposition is often performed in batch systems, continuous processing on substrates such as glass [62] and fiber mats is common, thereby allowing high volume production. [63,64] In addition, most methods for creating superamphiphobic surfaces link the morphology change and chemistry modification by incorporation of fluorinated nanoparticles or nanofibers. [26,31] The reported coating thicknesses range from a few hundred nm to a few μm, although many of these studies do not specify layer thickness. Such thick layers limit the ability to alter nanoscale roughness and inhibit identification of the role played by nanoscale roughness in controlling wettability. [33,65] Independent control of the surface chemical and topological features is needed in order to better understand and control the complex mechanism of wetting.

1.3 Oil-Water Separation Using Materials with Unique Wetting Properties

The separation of oily wastewater and cleanup of oil spills is a worldwide concern because of the catastrophic impact of the large amount of oil-water mixture on our environment. Materials with special wetting properties have received tremendous attention during the recent years due to their potential to be used in oil-water separation. The separation mechanism is the materials' opposing affinities towards oil and water, thus hydrophobic and oleophilic, or hydrophilic and oleophobic materials have both been reported in the literature for successful separation of oil-water mixture or oil-water emulsions. [66-71] For example, Wang *et al.* have successfully fabricated superhydrophobic steel mesh by depositing dual scale silica coated polystyrene particles topped with hexadecyltrimethoxysilane coating. [72] The coated steel mesh shows multi-

scale hierarchical structure (see Figure 1.11a-d) and excellent oil-water separation ability (see Figure 1.11e).

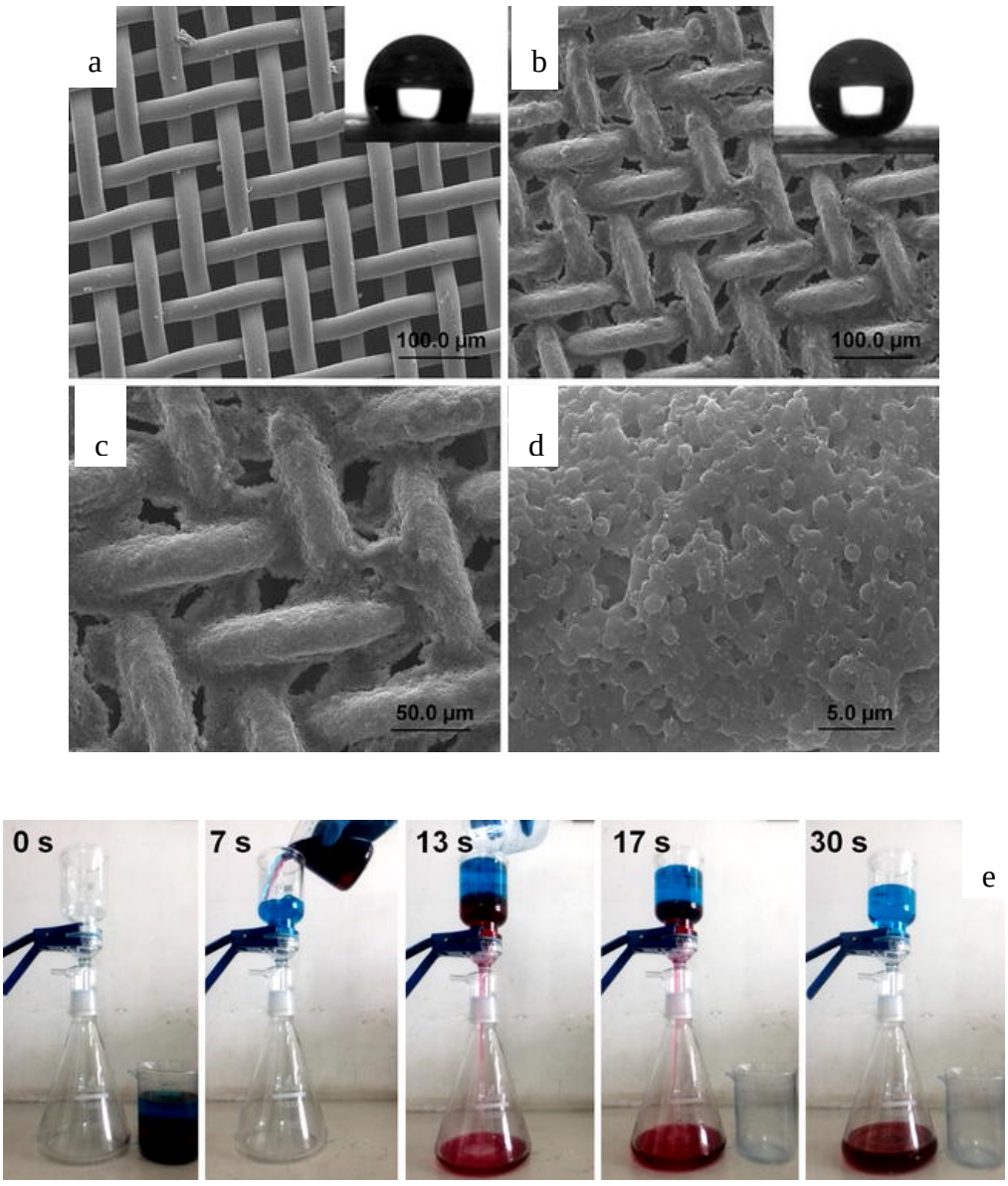

Figure 1.11: SEM images of (a) pristine steel mesh film, (b, c, d) prepared superhydrophobic steel mesh film with increase magnification level and (e) photograph of the prepared mesh-based oil-water separation process of water and chloroform. The chloroform and water were dyed with oil Red Dye 24 and methylene blue for clear observation, respectively. [72]

Despite the various wetting properties of the materials used for oil-water separation, they can be classified into two categories: filtration or absorption. Selective absorption of oil-water mixture can be achieved using particle and powdered absorbents, polymeric sponges and foams. [69,73-77] Among these absorbent materials, sponges are mostly used because of their commercial availability, low cost, good elasticity and 3D internal structure. Su's group has reported the fabrication of a magnetic, superhydrophobic and oleophobic sponge which can be used with a peristatic pump to achieve continuous oil-water separation (see Figure 1.12). [78] For the absorbent materials for oil-water separation, the absorption capacity is clearly the key parameter to evaluate their separation performance. Ma *et al.* has summarized the methods and absorption capacity of some of the current porous absorbents. [79] In practical application, after absorption equilibrium, the absorbed water or oil must be collected and removed from the absorbent materials before being reused in the next operation recycle. This type of operational cost and materials' reusability are still challenges for the wide application of absorbent materials.

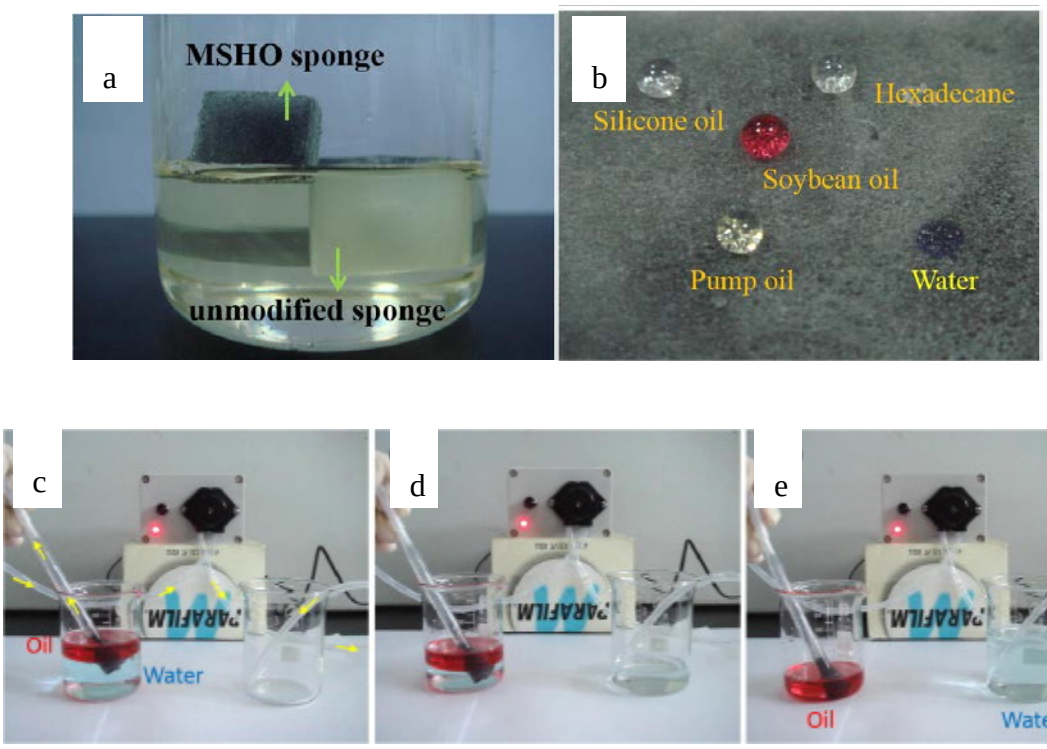

Figure 1.12: (a) photograph of the unmodified sponge and prepared superhydrophilic/oleophobic sponge after being placed on soybean oil, (b) photograph of water and various oil droplets onto the treated sponge, (c-e) pump assisted continuous oil-water separation using the prepared sponge. The soybean oil was labeled with oil red O and water is colored with ethylene blue for clear observation. [78]

Some common materials used for oil-water filtration are metallic meshes, fabrics and polymeric membranes. [80-86] Compared with polymeric membranes used in traditional filtration process, novel filtration materials such as metallic meshes and fabrics with special wetting properties do not require elevated operation pressure, and display fewer fouling concerns, better mechanical strength and improved cycling performance. Zhu *et al.* have successfully fabricated reusable superhydrophobic copper mesh, fabric and sponge that can be applied in oil-water separation (see Figure 1.13). [87] The

superhydrophobicity was achieved by dipping the substrate into a solution of polyfluorowax-hydrophobic SiO_2 to obtain specific surface morphology and chemistry.

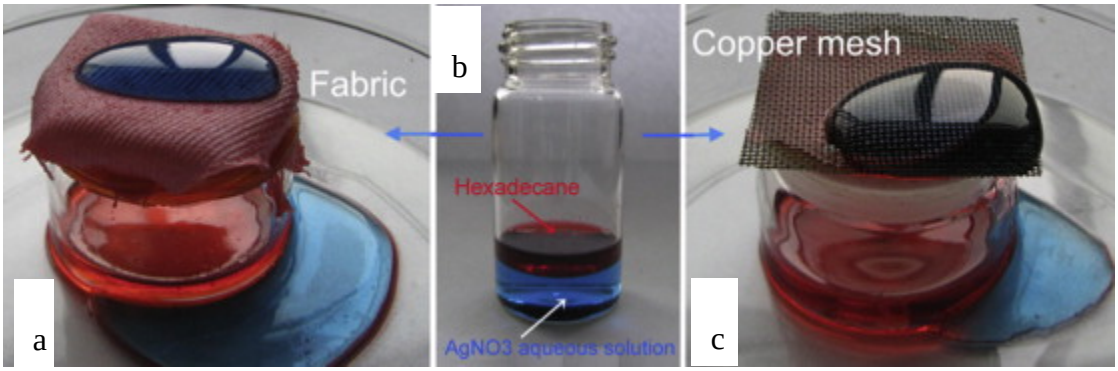

Figure 1.13: Photograph of prepared superhydrophobic/oleophilic (a) fabric and (b) copper used for oil-water separation. Hexadecane, colored with oil red, easily passes through the fabric, whereas water dyed with methylene blue stays on the surfaces. [87]

However, due to the large pores in the material, metallic meshes and fabrics have limits in separating oil-water emulsions where the size of the dispersed liquid is a few nanometers to tens of micrometers. Thus, with successful modification of surface wettability on polymeric membranes, unique oil-water separation performance can be attributed to their smaller and controllable pore size. Liu *et al.* have systematically studied the effect of pore size and pressure difference on oil-water separation on superhydrophilic/under water superoleophobic stainless steel meshes and polyvinylidene fluoride (PVDF) membranes. [88] They found that their coated stainless steel mesh with pore size larger than 5 µm cannot separate oil-water emulsions while the prepared PVDF

membrane with pore size ranging from 0.22 μm to 2 μm can achieve effective separation of various surfactant stabilized emulsions (Figure 1.14).

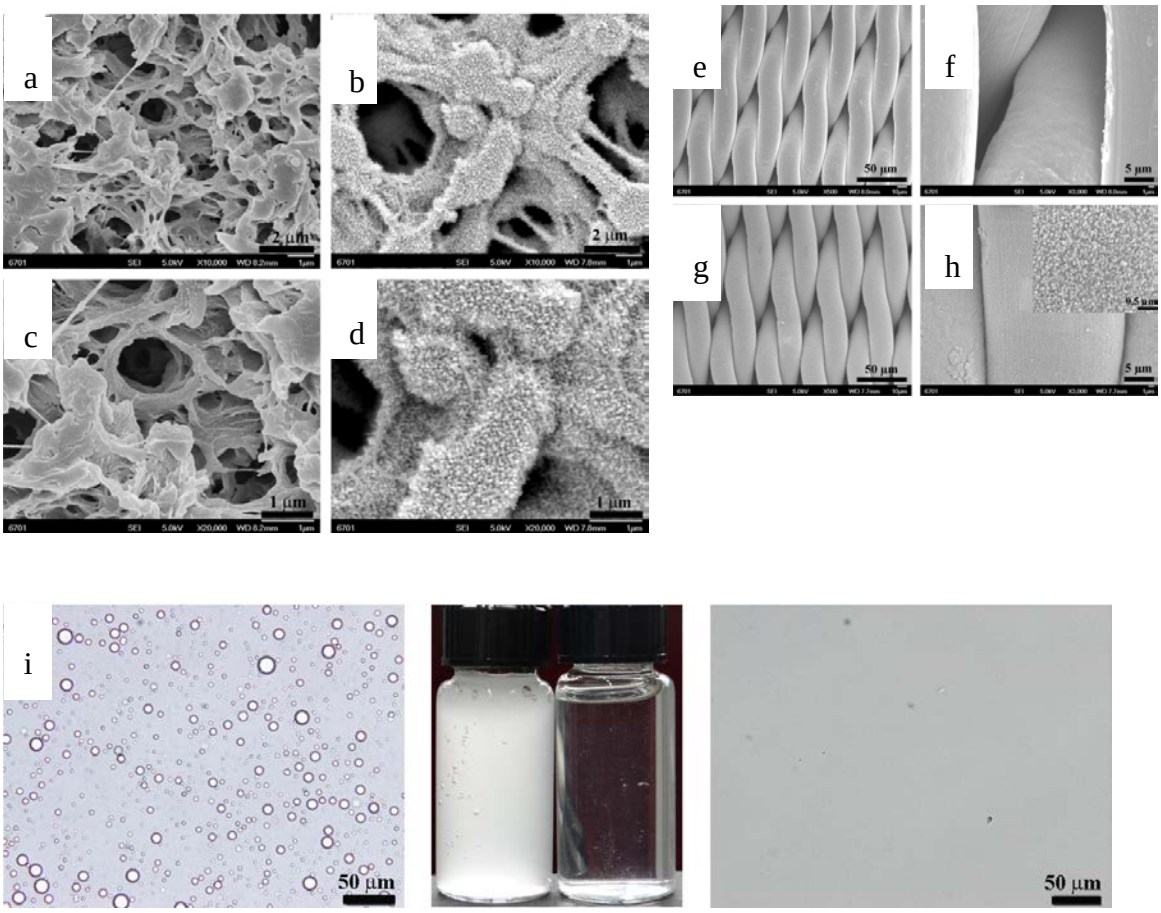

Figure 1.14: SEM images of (a,c) original PVDF membranes, (b,d) PANI-modified PDVF membranes, (e,f) original stainless steel meshs, (g,h) PANI-modified stainless steel meshs and (i) optical photographs of hexane-in-water stabilized by 1mg/ml Tween 80 (left) and collected filtrates (right) using PANI-modified PVDF membranes. [88]

1.4 Mechanical Durability Tests of Liquid Repellent Surfaces

Although extensive reports of liquid repellent surfaces exist, the large majority of them do not describe tests on mechanical robustness and long-term durability. [89-93]

This piece of information is important for their utilization in real-world applications and many researchers have realized this and started characterizing or improving the mechanical resistance of these surfaces. [94,95] Although the liquid repellency of a surface can degrade upon exposure to varied environmental exposures such as chemical corrosion, bacterial adhesion or UV exposure, mechanical wear is the type of degradation that most affects the performance of liquid repellent surfaces most in daily use.

Major aspects of mechanical durability that are important for commercial application and are often investigated separately or in combination in the literature are coating adhesion, resistance to tangential abrasion, dynamic impact, liquid bath (particular for textile industry) and bending and pressing for specific applications. For coating adhesion, tape peeling is recognized as the simplest and most useful adhesion test. Some studies have developed more stringent adhesion tests based on tape peeling called cross-hatch tape test where certain pattern is scratched on the surface before tape peeling is applied (Figure 1.15).

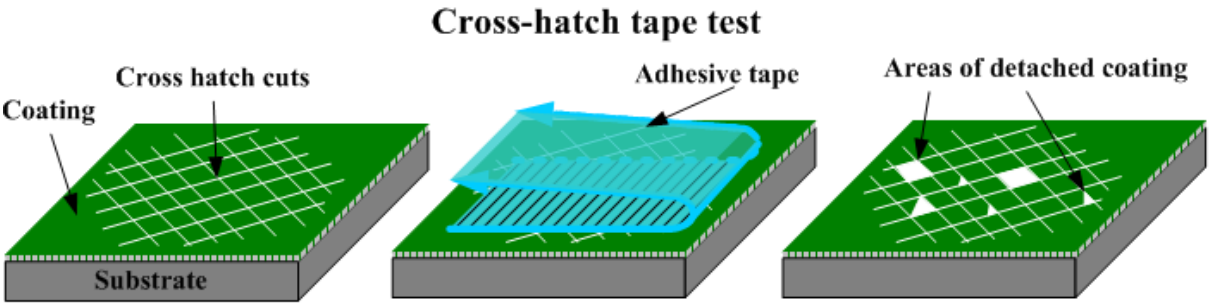

Figure 1.15: Schematic illustration of cross-hatch tape test (substech.com).

Tangential abrasion is widely encountered in the daily use of liquid repellent surfaces, and the resulting surface destruction has been evaluated by various tests. One

common test is the linear or circular movement of abradent material on the surface (see Figure 1.16).

Figure 1.16: Typical linear abrasion setup (left): a rod with a predefined weight moves linearly and rubs the tested surface tangentially. Photograph of the Taber linear abraser (right). [96]

Since scratching the surface with a bare-finger, sandpaper, pencil or knife/blade does not require an expensive experimental setup, these are more common in the literature. [42,97-101] Wang *et al.* set up a customized blade scratching system where 0.8 kg weight was loaded on the blade which was dragged along the tested surface (Figure 1.17). [99] They found that with increased number of scratches, liquid repellency gradually reduced. After 100 scratch cycles, the coated fabric lost ethanol repellency and water and hexadecane contact angle dropped to 150° and 120° respectively.

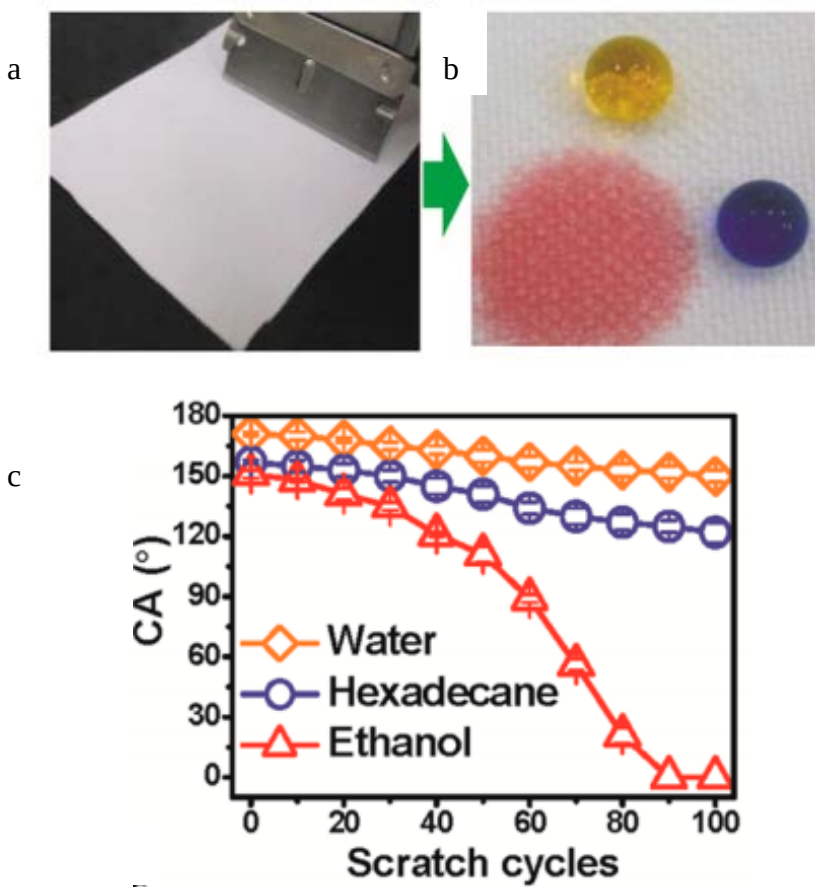

Figure 1.17: (a) photos of scratching fabric with a sharp blade, (b) colored water and hexadecane drops on the coated fabric after 100 scratches where colored ethanol was absorbed and (c) contact angle changes with 100 scratches. [99]

Dynamic impact durability deals with a material's resistance to external collison from solid, liquid or gases. This type of test could generate valuable information whether the surface will retain its liquid repellent properties in outdoor applications. Typical experimental testing setup for solid particle collosions is shown in Figure 1.18a where a certain amount of sand particles flood the surface from a certain height. Deng *et al.* applied 100 to 300 μm sized sand grains from different height on their superhydrophobic surface which was fabricated on glass slides modified with porous silica shells. [102]

They reported that the surface morphology and superhydrophobicity remained intact and with impact heights up to 30 cm. However, fractured surface structure was found when sand impinged from a height significantly higher than 30 cm. Similarly, researchers have also used water sprays to evaluate a surface's performance in an environment with liquid impact (see Figure 1.18b and c). [103-105]

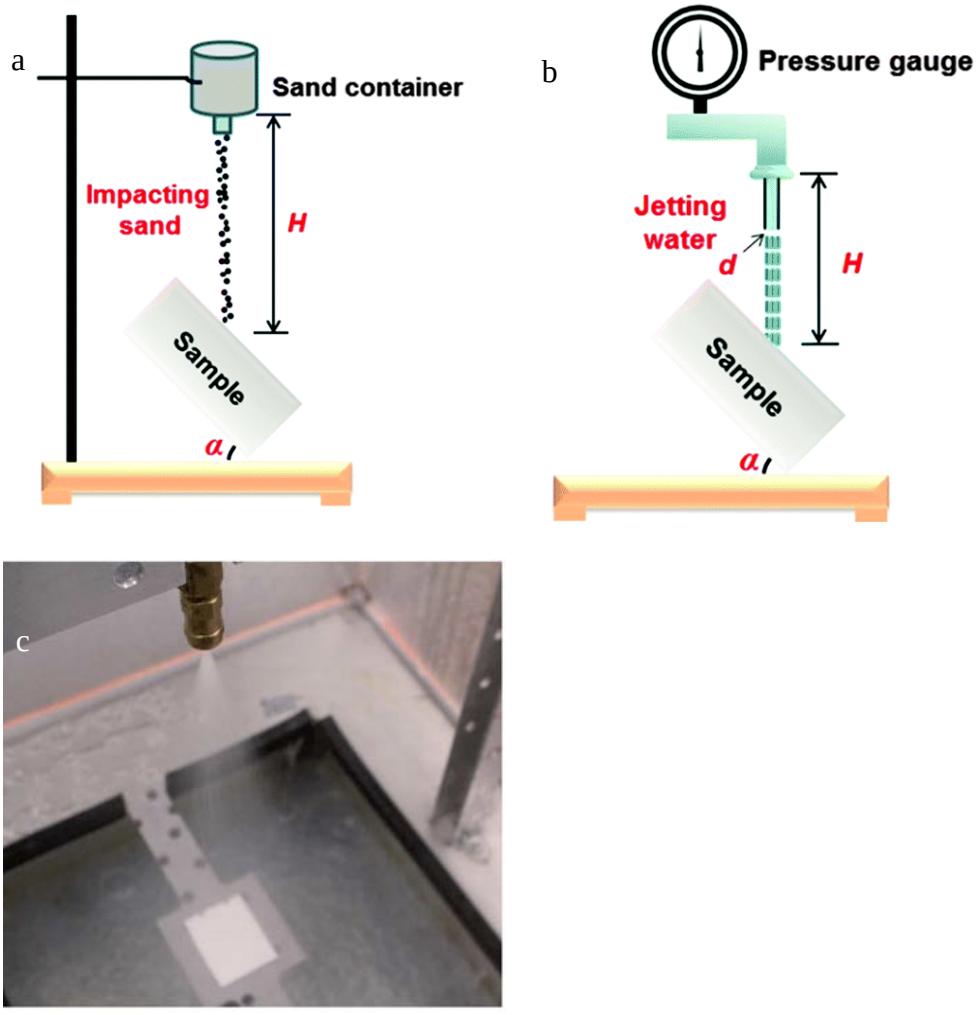

Figure 1.18: Illustration of common (a) sand impact test, (b) water jet test setup [106] and (c) photo of spray jet setup to investigate rain impact resistance of superhydrophobic surfaces. [105]

Nonwetting materials reported in the literature have shown high contact angles or good repellency under liquid impact; however, these results do not guarantee that the material will not absorb liquid gradually during immersion. For the textile industry, resistance to laundry wear must be tested to evaluate the mechanical durability of liquid repellent textiles. [107-111] Both mechnical abrasion and chemical additives can possibly accelerate the degradation of the textiles coating during liquid bath immersion. Yoo *et al.* fabricated a robust superhydrophobic fabric through initiated chemical vapor deposition of a stacked polymer film composed of a poly(1,3,5,7-tetravinyl-1,3,5,7-tetramethylclotetrasiloxane) (p(V4D4)) layer and a poly(1H,1H,2H,2H-perfluodecylacrylate) (p(PFDA)) layer. They tested the mechanical robustness of the fabric with a laundry machine (LF, WFTS107A) with a commerical detergent (LG healthcare, laundry detergent tech. 1 sheet percycle) added. Figure 1.19a shows that the contact angle remained above 150° after 75 cycles of washing and rinsing. In addition, they found that the hierarchical structure they imparted to the fiber surface was perserved after the laundry test (see Figure 1.19b and c).

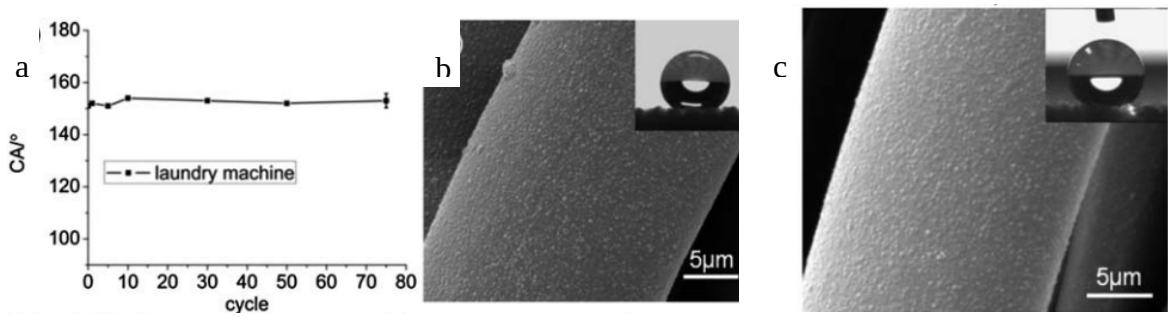

Figure 1.19: (a) water contact angles plotted with respect to the number of laundry cycles. (b) SEM images of the stacked polymer film coated polyester fabric surface and (c) SEM images of the fabric surface after the laundry test. [108]

The contact angle data and surface morphology indicate the robsutness of the fabric surface under a harsh laundry environment, although this does not guarantee no degradation is present on the surface. XPS analysis shows that fluorine content decreased while silicon content slightly increased (Table 1.1) after 50 laundry cycles. They attributed this change to the exposure of the bottom polymer film p(V4D4) cuased by the frictional wear of top coating material p(PFDA). For non-deformable materials or surfaces with limited liquid repellency, this type of liquid bath test is typically not performed.

Table 1.1: Atomic percentage of the p(V4D4-L-PFDA) coated fabric surface before and after the laundry cycle (atomic %).

Element	Carbon	Oxygen	Silicon	Fluorine
Before laundry	40.46	6.31	0.84	52.39
After laundry	45.87	8.07	1.08	44.08

For applications that involve non-wetting surfaces with curvature and coomerical packaging materials, the mechanical robustness of surfaces under pressing (bearing weight) and bending or even folding are both of great importance for their long term performance. A few researchers working on wetting modification of materials for specific applications have applied mehanical robustness test of folding (bending) or pressing on their prepared surfaces. [112-115] Kim *et al.* have fabricated a transparent, highly flexible, superhydrophobic plastic film by tansferring a porous alumina membrane (PAM) to the top surface of UV-imprinted polymeric micropillar arrays with a polymer

adhesive and chemically treating the transferred PAM. [112] They targeted their materials for applications such as glass-based products with different curvatures. Thus up to 2000 cycles of reptitive bending and pressing was applied on the prepared surfaces to test their superhydrophbic robustness. Figure 1.20 shows the water static contact angle and hysteresis change on the superhydrophobic film after different cycles of bending and pressing. No appreciable degradation of wetting properties were found on the surface after repetitive bending and pressing showing the material's superior robust performance.

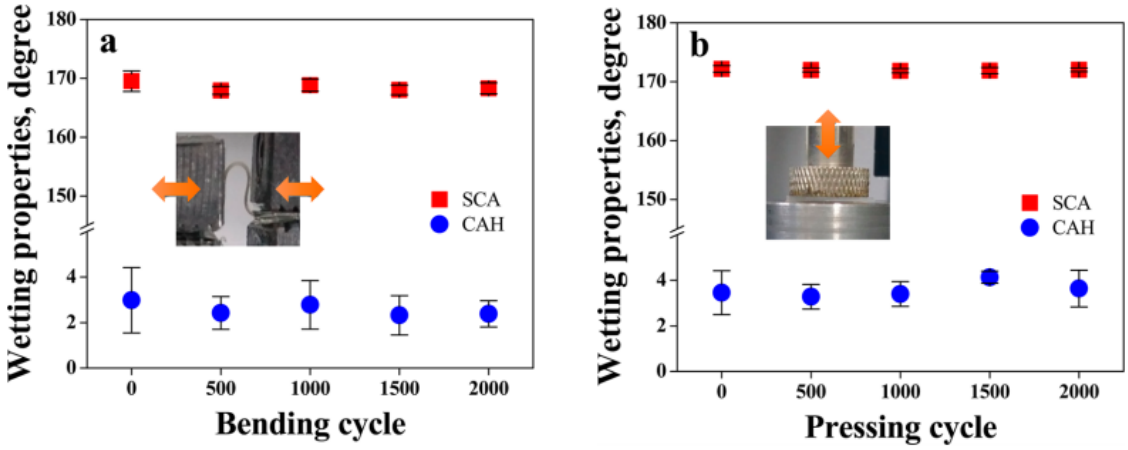

Figure 1.20: Changes in surface wetting properties due to (a) repetitive bending tests with a minimum bending radius of 2 mm and (b) repetitive pressing tests with a maximum normal forces of 5 N. [112]

1.5 Outlook

As a biodegradable, inexpensive and universally accessible material used in packaging, printing and cleaning, paper remains a vital component of our society. However, the hydrophilic and oleophilic nature of paper often limits its appearance in certain applications. Creating non-wetting paper products has great potential in future

applications in the fields such as microfluidic devices, medical testing strips, liquid packaging and disposable medical apparel. Thus, wetting modification on paper has been investigated in great detail during the past several decades. However, due to the heterogeneity of the fiber surface and vulnerability to some stringent surface modification techniques, successful fabrication of superamphiphobic paper surfaces has seldom been reported. Existing reports on non-wetting paper usually employ complex fabrication processes. In addition the surfaces either lack mechanical robustness or do not possess good repellency towards low surface tension liquids. Since the two principle requirements of all superamphiphobic surfaces are surface morphology and low surface energy, more clear understanding of the design parameter involved in achieving superamphiphobicity on fibrous surface is needed in order to tailor the surface modification techniques according to the specific application desired. The mechanical strength and robustness have yet to be improved for those reported liquid repellent products intended for commercial applications. Thus a standard evaluation system has to be developed to generate valuable information on products' long term performance under different mechanical impacts that will be encountered in specific applications. As the understanding of and fabrication techniques for superamphiphobic surfaces continue to evolve, robust and cost-effective paper with unique wetting properties will make its appearance in a wide range of practical applications.

1.6 Thesis Outline

In this thesis, we explored how wetting properties change with surface chemistry and fiber network topography on substrates such as paper and stainless steel metal mesh.

Chapter 2 focuses on tuning liquid repellency of paper surfaces by combining pulp pretreatment (refining, debonder addition) and controlled plasma etching. Debonder was used specifically to modify the anti-wetting properties of paper substrates by controlling the topology of the fiber network. These studies improved the understanding of the design of superamphiphobic surfaces on paper and other porous materials. Chapter 3 describes the creation of superamphiphobic paper with liquid "roll-off" properties towards a wide range of liquids. A two-step process that included oxygen plasma etching and vapor deposition enables fine tuning of nanoscale roughness and thereby facilitates enhanced fundamental understanding of the effect of micro- and nano-scale roughness on paper wetting properties. Chapter 4 applies hydrophilic/oleophobic stainless steel (SS) meshes fabricated by a one-step solution-based coating method using methyltrimethoxysilane (MTMS) to separate oil-water mixtures. This approach minimizes cost and material waste while achieving excellent separation performance. Chapter 5 describes investigations on how various types of coatings react to different mechanical impacts on flat and non-flat surfaces. A comprehensive understanding of the surfaces' mechanical robustness was generated by employing the most frequently reported mechanical durability tests. Chapter 6 discusses the conclusions of this thesis along with future recommendations for research.

CHAPTER 2

FABRICATION OF HIGHLY AMPHIPHOBIC PAPER USING PULP DEBONDER

Reproduced from L. Jiang *et al. Cellulose* 23.6 (2016): 3885-3899

2.1 Introduction

Successful and economically feasible fabrication of superior liquid repellent surfaces on cellulose-based materials will create a new path towards cheap and "green" materials for food packaging, microfluidic devices and self-cleaning surfaces. Our group has previously reported the successful fabrication of highly non-wetting paper surfaces, but the low strength of those substrates, which were created from non-aqueous pulps, prohibits broad use. [34] Other studies on superamphiphobic paper involve the deposition of nano-particle coatings on paper rather than exploitation of the inherent nanostructure of cellulose fibers. [37,116] In addition, these studies either require a sophisticated fabrication process such as blending of copolymers and silica particles under strict processing conditions prior to substrate coating, [117] or they lack reported evaluation of mechanical strength and coating stability. [34] Because of these issues, alternative amphiphobic papermaking techniques that are simple, cost effective and easy to scale up are of significant interest.

For fiber-based surfaces, the Cassie-Baxter model has been modified for the specific case of parallel, regularly spaced, cylindrical fibers (Eq. 1.4).

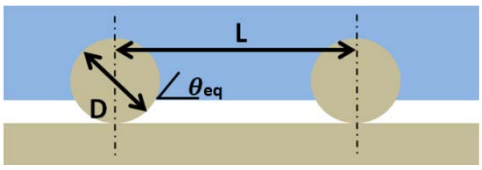

Figure 2.1: Schematic representation of the composite interface on fiber surfaces with reentrant topography.

In Equation 1.4, the apparent contact angle of the liquid θ^* is determined by the inter-fiber spacing *L*, the fiber diameter *D* and the equilibrium contact angle θ_{eq} (Figure 2.1). [35] Figure 2.2 represents the predicted apparent contact angle according to Equation 1.4 as a function of *L/D* ratio and equilibrium contact angle. It should be noted that when the *L/D* ratio is 1, θ_{eq} must be larger than 58° to generate a valid θ^* value. Similarly, the *L/D* ratio must be larger than $\frac{\pi}{2}$ when θ_{eq} is 0°. Since the θ^* values observed in this study do not fall within that range, only *L/D* ratios greater than $\frac{\pi}{2}$ are presented in the graph. The figure shows that increases in both *L/D* and equilibrium contact angle result in a higher apparent contact angle; as qualitatively expected, surfaces with lower surface energy (higher equilibrium contact angle) and fibrous structures with higher *L/D* ratios favor superamphiphobicity. That is, in order to achieve higher apparent contact angles (greater than 150°) on a substrate with lower *L/D* ratio (higher paper strength), a higher equilibrium contact angle is needed. This explains why water, with a relatively high equilibrium contact angle on hydrophobic substrates, responds more strongly to surface morphology changes on fiber-based substrates than apolar liquids. This is consistent with the commonly observed fact that on paper, superhydrophobicity is easier to achieve than oleophobicity.

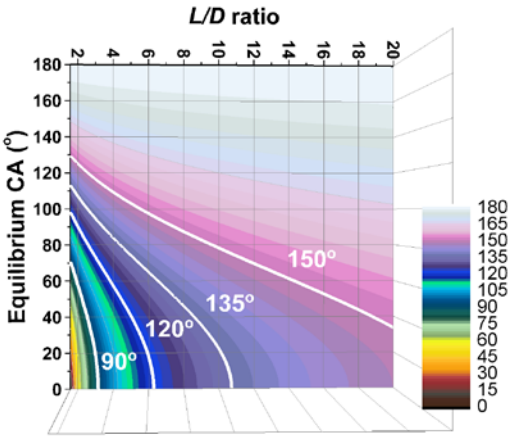

Figure 2.2: Contour map showing the relation between *L/D* ratio, equilibrium CA (θ_{eq}) and apparent CA (θ*) on fiber based substrates.

In this chapter we present a facile method to achieve high amphiphobicity on paper using three simple processing steps: debonder addition, oxygen plasma etching and liquid-based fluorosilane coating. In our previous study, which used solvent exchange (to increase *L*), oxygen plasma etching (to decrease *D*) and plasma enhanced fluoropolymer deposition (to further increase θ_{eq}) to create superamphiphobic paper, the mechanical strength of paper was greatly reduced after solvent exchange and oxygen plasma processing due to inhibition of hydrogen bonding interactions that are responsible for inter-fiber bonding. [34] In contrast, the tensile strength of the highly amphiphobic paper fabricated using the three-step process in this study remains similar to that of commercial copy paper. The modified process is more facile, inexpensive and suitable for scale-up. Refining can be used to decrease the fiber diameter *D* by fibrillating individual fibers as a result of grinding pulp between metal gears. This process generates fiber-wall fragments known as “fines”; in general, pulp particles that pass through a 75 μm diameter round

hole are considered fines. [118,119] Fines in this study are mainly generated by refining and thus called secondary fines. They are usually present in the form of fibrils that attach to the fibers via hydrogen bonding. Unfortunately, fines fill the pores between fibers and smooth the paper surface during papermaking, which renders the concept of a well-defined *L/D* ratio meaningless.

Our goal in this chapter is to obtain lower *D* values while keeping pores in the final paper structure clear of fines. In order to remove fines from the pulp, hydrogen bonding between the fines and fibers must be inhibited. In the paper industry, surfactants are used as debonding agents (also called softeners or debonders) during production of porous products like tissue paper, diapers and absorbent toweling. [120-122] The softness of a paper product is enhanced by interrupting bonding between fibers, and the resulting increase in porosity is beneficial for water absorbency of these products. Commercially available debonders are generally comprised of a quaternary ammonium surfactant, a non-ionic surfactant as well as strength additives. These entities bond to the fiber surface, thus reducing the potential for inter-fiber hydrogen bonding. Compared with typical fibers, fines have a much higher surface area per unit mass and therefore offer greater bonding area. In our investigations, we found that significant fines removal can be achieved by debonder addition to the refined pulp, and that residual fines can be removed easily by etching in an oxygen plasma. After initial fines removal, plasma etching and fluorochemical deposition were employed to create the requisite fiber roughness and low surface energy coating needed for amphiphobicity. To our knowledge, this is the first time that debonding agents have been used to alter the paper structure to establish anti-wetting properties. In order to demonstrate that the mechanical strength of the modified

paper is not substantially changed from that of traditionally processed paper, tensile strength and stiffness measurements were performed.

2.2 Experimental Methods

Pulp Refining

Southern hardwood kraft fibers (Alabama River mill, Georgia-Pacific Cellulose Co.) were used. The dry fiber sheets were soaked in deionized water overnight before further treatment. The fibers were then refined in a PFI mill for 6,000, 10,000 or 15,000 revolutions according to TAPPI standardized method T 248 sp-08.

Debonder Addition and Paper Formation

Debonding agent (FluffSoft F639) was kindly donated by Emerald Performance Materials, LLC. 90% of the functional components are either an ethylene oxide adduct of a vegetable oil or a propylene oxide adduct of a fatty acid; 8.5% is a C16-18 alkyl benzyl dimethyl ammonium chloride (proprietary). 150 μl debonder/g dry fiber was added to the refined pulp and stirred for 1 hour; paper was then formed following TAPPI standardized method T 205 sp-02 using treated pulp.

Plasma Etching

Paper samples were placed in a 2.5 inch parallel plate electrode (13.56 MHz) plasma reactor and etched for various times. During etching, oxygen was introduced into the reactor at 20 standard cubic centimeters per minute (SCCM) under an equilibrium pressure of 0.5 Torr. The etching process was conducted at 110 ℃ using a power of 120

W. A more detailed description of the reactor configuration can be found in previous publications. [48,49]

Fluorosilane Coating

Before coating the paper, 100 µl of (heptadecafluoro-1,1,2,2-tetrahydrodecyl)trimethoxysilane (FDTMS) (Gelest, Inc.) was pre-hydrolyzed to generate hydroxyl groups in 1 ml isopropanol (IPA) (Reagent Grade, Fisher Chemical) with 20 µl ammonium hydroxide (VWR Inc.) added as catalyst and stirred at 350 rpm for 1 hour. [123] The paper substrate was immersed in this solution for 1 hour. After immersion, the substrate was removed from the solution and rinsed with IPA. Excess fluid on the substrate was then removed by absorption into tissue paper (KimWipe, Kimberly-Clark Co.). Finally, the paper was cured in an oven (Fisher Scientific, Model 825F) at 100 ℃ for 30 minutes.

Contact Angle Measurements

All static contact angle measurements were performed by placing a 4 µl droplet of selected fluid (DI water, motor oil (SAE 10W-30, MotoTech), n-hexadecane (Sigma-Aldrich Co., 99%)) onto the testing substrate. Images were recorded and analyzed by a ramé-hart goniometer (model 290). Contact angle hysteresis was measured by increasing and decreasing the droplet volume, with an initial volume of 4µl and step changes of 0.3 µl. For each substrate-fluid combination, both static contact angle and contact angle hysteresis measurements were repeated five times.

SEM Imaging

Scanning electron microscopy (SEM) was performed on paper substrates that were sputter coated with Ag/Pd to mitigate charging effects during imaging. Images were taken with a Hitachi SU8230 cold field-emission SEM (Hitachi High-Technologies Co., Japan).

Profilometer Measurement

Measurements were conducted using a LEXT OLS4100 Laser Scanning Confocal Microscope (LSCM) profilometer with a laser wavelength of 405 nm (Olympus Co., Japan) and a scan area of 644 μm × 646 μm.

Mercury Porosimetry

The pore size distribution of substrates was determined using a Micromeritics AutoPore IV 9500 mercury porosimeter. Paper samples were cut into 3 mm × 3 mm squares and evacuated to a pressure of 6.7 Pa (50 μm Hg) for 5 min in order to remove physisorbed gases from the interior of the sample before starting the mercury intrusion experiments.

Tensile Strength, Stiffness and Density

Z-directional tensile strength of paper substrates was measured by Monitor ZDT (Testing Machines Inc., Model 84-22) according to Tappi Standardized method T 541 om-10. The Z-directional elastic stiffness and density tests were performed by OPUS 3-Dimensional Ultrasonic System (Sonisys Inc.). For tensile strength and elastic stiffness, at least 4 measurements were performed for each experimental setting.

X-ray Photoelectron Spectroscopy

The elemental composition and chemical bonding information of the substrates were determined with a Thermo K-Alpha XPS (Thermo Fisher Scientific, West Palm Beach, FL) at a pressure below 10^{-7} Pa. Thermo Advantage 5.934 software was used to curve fit and deconvolute the high resolution C1s spectra.

2.3 Results and Discussion

Effect of Refining, Debonder and Plasma Etching

As discussed above, the apparent contact angle of a liquid on paper can be increased through a reduction of the (average) fiber diameter *D* and an increase in the spacing *L*. To reduce *D*, refining is generally used. Figure 2.3 shows SEM images of paper substrates that were made from hardwood pulp and subjected to varying levels of refining. For convenience of the discussion below, we classify our substrates by the number of revolutions (in thousands) they experienced during refining and the pulp type. Thus, 6HW designates a substrate formed from hardwood pulp after exposure to 6,000 revolutions of refining.

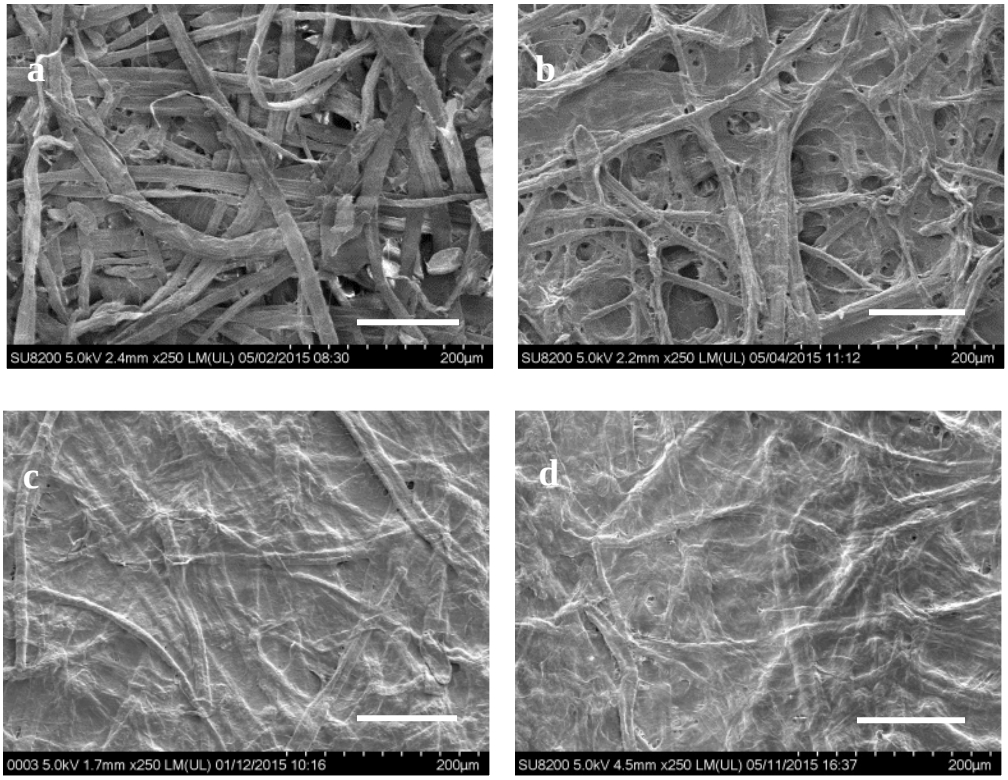

Figure 2.3: SEM images of (a) unrefined paper and paper refined for (b) 6,000, (c) 10,000 and (d) 15,000 revolutions (displayed in the sequence of increased mechanical treatment time). The scale bars represent 100 µm.

A high level of refining yields thinner fibers, homogenizes the fiber distribution and produces more fines that cover the fibers and fill inter-fiber spaces (from Figure 2.3a to 2.3c). When refining level gets even higher, their effect on fiber fibrillation and fine generation will reaches a plateau (compare Figure 2.3c and 2.3d). Both 10HW and 15HW pulp contain large amounts of fines that block inter-fiber pores and thus increase the water draining time during the paper forming process. At the same time, the higher degree of refining increases the paper strength through improved fiber bonding. Thus, 6HW has the lowest mechanical strength compared to 10HW and 15HW, especially after prolonged plasma etching (longer than 30 minutes) during the next processing step.

Balancing fiber diameter, fines content and energy input, 10HW was chosen for this study. To take advantage of the thinner fibers in the sheet and achieve favorable *L/D* ratios, fines that block the inter-fiber pores must be removed.

We used debonder to perturb the bonding between fines and fibers, as well as fiber-fiber bonding. Table 2.1 lists the density, Z-directional elastic stiffness and tensile strength before and after debonder addition. After debonder addition, the density of paper decreases, indicating an increase in paper porosity.

Table 2.1: Density and mechanical strength changes of 10HW with and without debonder treatment.

Substrate	Density (kg/m^3)	ZD elastic stiffness (GPa)	ZD tensile strength (psi)
10HW	1003 ± 42	0.30 ± 0.01	83 ± 11
10HW w/ debonder	854 ± 13	0.22 ± 0.01	58 ± 12

After the debonder treatment, the paper qualitatively feels softer. Based on the SEM images in Figure 2.4, fibers are more prominent on the surface and some pores are partially open due to reduced accumulation of fines (see Figures 2.4a and 2.4b). Since fines play a significant role in improving paper strength and the level of hydrogen bonding is a good indication of the paper strength and stiffness, the observed decrease of paper stiffness and tensile strength (see Table 2.1) can also be interpreted as signs of fines removal and suppression of hydrogen bonding. Even larger differences between paper

made with and without debonder addition are observed after plasma etching. Figures 2.4d and 2.4e show the changes in paper structure after 60 minutes of plasma etching, with and without debonder, respectively. After plasma treatment, paper with debonder appears more porous than paper without debonder, which still has pores that are clogged with fines. Our explanation for these observations is that debonder not only removes fines from the pulp, but also loosens the bonding between fiber and fines, which are then removed more easily during plasma etching. Thus, after prolonged etching treatment, the structural differences become more prominent. The high magnification images of Figures 2.4c and 2.4f highlight the nanoscale roughness of fibers generated by oxygen etching, which promotes suspension of droplets in a Cassie-Baxter state and increases the apparent contact angle.

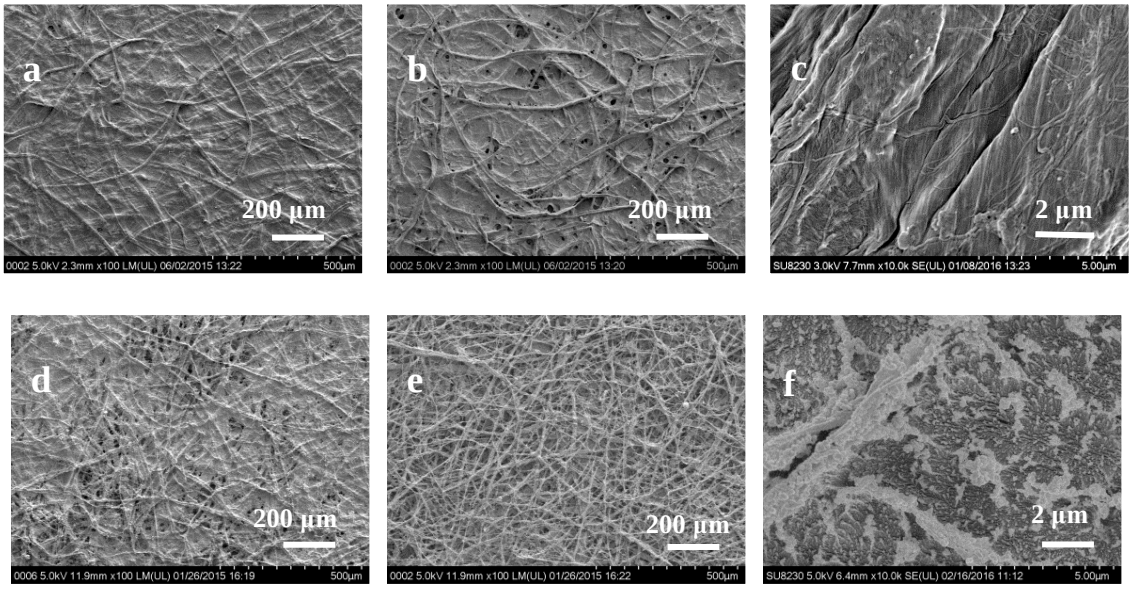

Figure 2.4: SEM images of 10HW paper before oxygen plasma etching: (a) without debonder, (b/c) with debonder (low and high magnification), and after 60 minutes etching: (d) without debonder, (e/f) with debonder (low and high magnification).

According to the SEM images displayed in Figure 2.4, the proposed mechanism of the fabrication process is illustrated in Figure 2.5. Firstly, debonder removes a significant amount of fines from the pulp thus the paper has less fines clogging the inter-fiber spacing. Then the plasma etching process will etch away even more fines on the surface and reduce the fiber diameter. Also, nanoscale roughness will be generated on each fiber through plasma. Escaping either debonder addition step or plasma process will not give a porous paper surface clear of fines. Finally, a uniform fluorochemical coating could be deposited on the surface to decrease the surface energy. Changes in the cross section of paper showing the fiber-air-liquid interfaces are also depicted in Figure 2.5. Before the treatment, fines are filling the spaces between fibers and liquid get fully contact with the surface and wet the surface completely. After the three step process, nano-roughened thin fibers with large inter-fiber spacing are generated to support the liquid in Cassie-Baxter state where air pocket are trapped underneath the liquid.

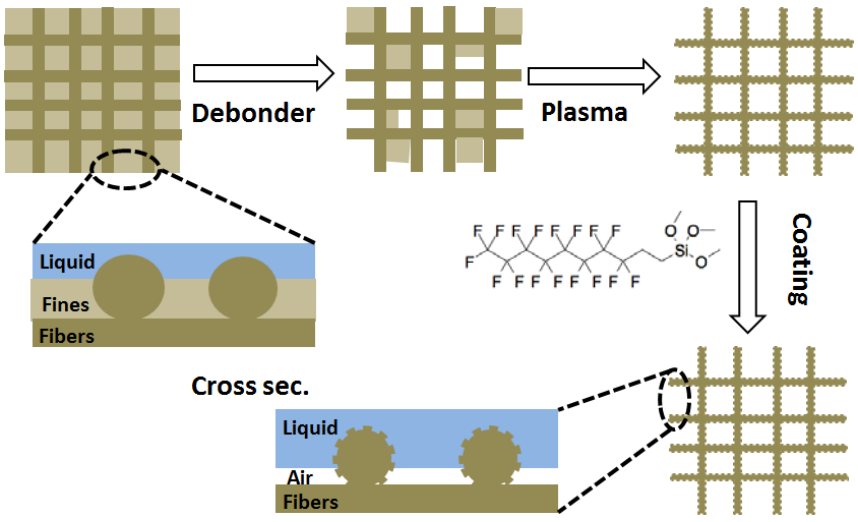

Figure 2.5: Schematic illustration of the process to fabricate highly amphiphobic paper.

In order to evaluate the effect of debonder and plasma etching more quantitatively, profilometry measurements were employed. The topography of the 3-D confocal microscopy images reveal a significantly increased nanoscale surface roughness after 60 minutes plasma etching for both samples, while debonder addition enhances microscale roughness due to fiber detachment (see Figure 2.6 and Table 2.2).

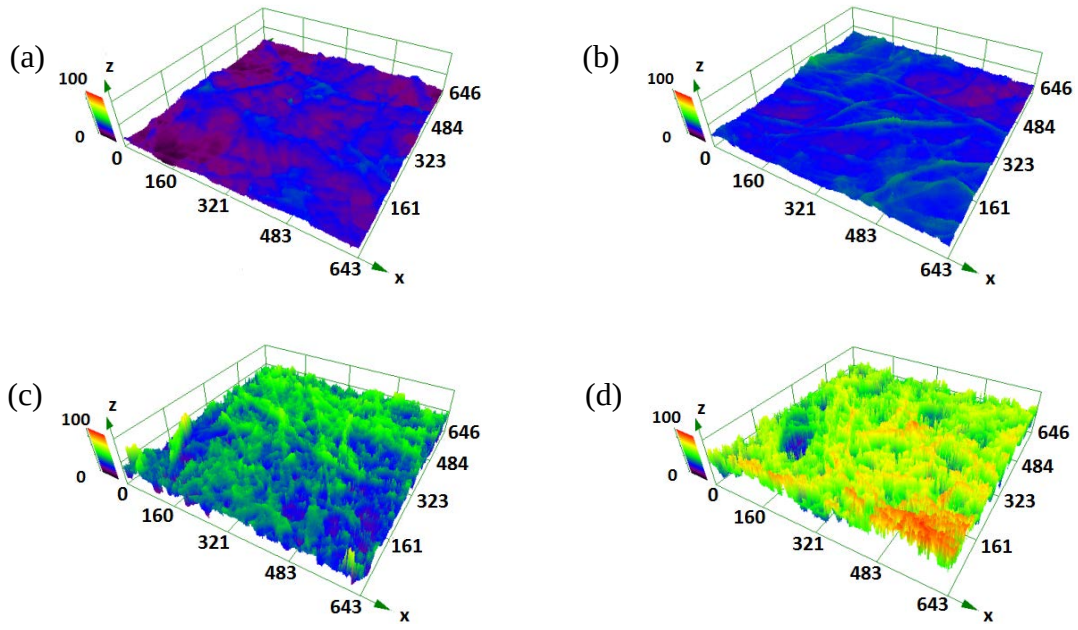

Figure 2.6: Laser scanning confocal microscope images of paper before oxygen etching: (a) without debonder, (b) with debonder; and after 60 minutes plasma etching: (c) without debonder and (d) with debonder.

Table 2.2: Average roughness (Sa), root mean square roughness (Sq) and peak-valley roughness (Sz) measured with LEXT laser scanning confocal microscopy.

Substrate	Debonder	Etch Time (min)	Sa (μm ± μm)	Sq (μm ± μm)	Sz (μm ± μm)
10HW	No	0	3.78 ± 0.16	4.74 ± 0.15	39.54 ± 1.15
10HW	Yes	0	4.18 ± 0.52	5.17 ± 0.67	38.64 ± 5.76
10HW	No	60	6.72 ± 0.51	8.23 ± 0.63	84.61± 10.80
10HW	Yes	60	12.11 ± 1.28	15.23 ± 2.30	118.37 ± 35.02

Based on SEM images and profilometer measurements, the addition of debonder does not modify the inter-fiber spacing *L* significantly, but it increases fiber protrusion from the substrate and increases porosity by opening up inter-fiber pores. In comparison, previous research within our group using sec-butanol to treat the pulp changed the inter-fiber distance greatly. [34] Although a large *L/D* ratio is preferred for improved liquid repellency (see Figure 2.2), the debonding effect of sec-butanol was too strong; the resulting increase in *L/D* ratio sacrificed the mechanical properties significantly.

Modified Cassie-Baxter Model

After 60 minutes of plasma treatment, the paper handsheets were coated with FDTMS for enhanced liquid repellency. Figure 2.7a and 2.7b present the SEM images of 60 minutes etched and FDTMS-coated paper that were prepared without and with debonder respectively. FDTMS coating does not modify the surface morphology significantly since paper made without debonder still clogged with fines and paper added with debonder remains porous. Figure 2.7c and 2.7d give a more detailed look on the

fibers of each sample. In Figure 2.7c, fibers appear more fractured than in Figure 2.7d. A potential explanation for the difference is that without debonder addition, no selective etching between fibers and fines is evident. Because fines produced in our study are mostly fiber-wall fragments, these bond strongly with fibers. For paper prepared with debonder, where the bonding between fines and fiber was inhibited, the smaller fines are more likely to be selectively etched away by an oxygen plasma, leaving the individual fibers relatively intact.

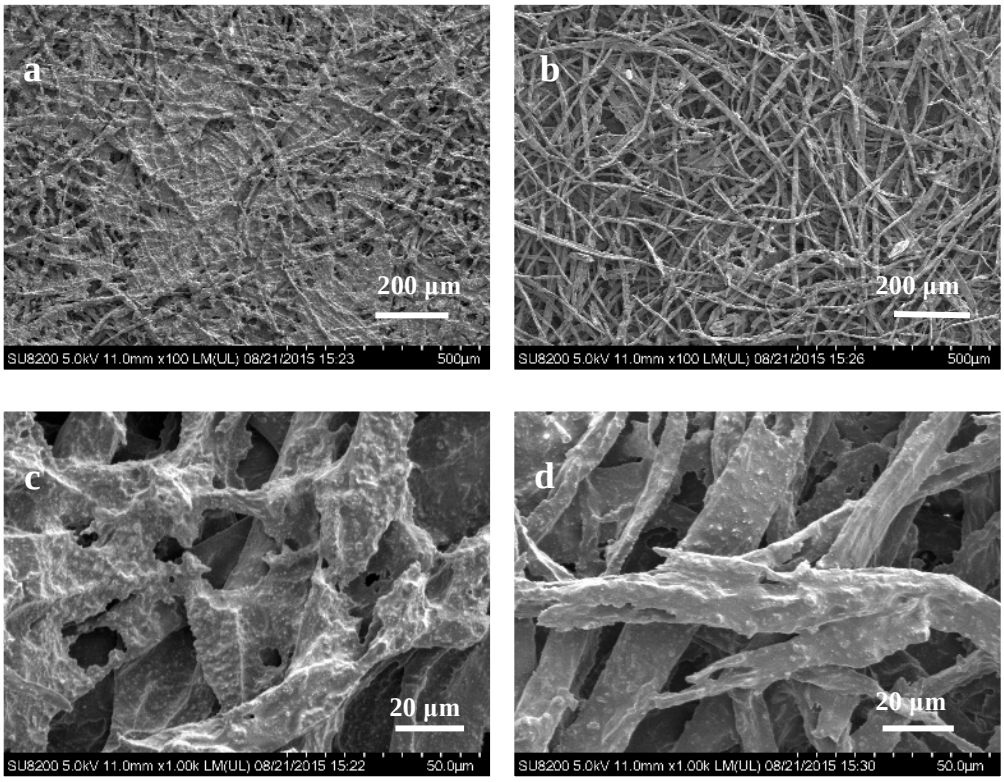

Figure 2.7: SEM images of 60 minutes plasma etched 10HW (a) without debonder and (b) with debonder, both after FDTMS coating, (c) and (d) are the high-magnification versions of (a) and (b), respectively.

The static contact angles and contact angle hysteresis of three testing fluids on different substrates, including an FDTMS coated silicon wafer as reference, are presented

in Table 2.3. It should be noted that without FDTMS treatment, handsheets are wetted completely by both water and oil. From Table 2.3, we can see that when debonder was added, the liquid repellency of coated paper was greatly improved. Comparing Figures 2.7a and 2.7b, it is clear that paper was more porous after oxygen plasma etching when debonder was added. This indicates an increase in the *L/D* ratio as described by Eq. 1.4, since 10HW without debonder remained partially clogged (regions with fines covering and connecting fibers) after oxygen plasma etching. The result offers strong support for the modified Cassie-Baxter model, which suggests that increasing the *L/D* ratio of fiber networks is essential for obtaining higher apparent contact angles. None of the testing liquids displayed roll-off behavior, even when the surfaces were tilted 90°. However, the contact angle hysteresis of water, motor oil and hexadecane were all reduced significantly by debonder addition (see Table 2.3). This observation is consistent with the decreased heterogeneity of the fiber network after debonder addition (reduced localized fines accumulation) and plasma etching (compare Figures 2.7a and 2.7b), which reduces liquid droplet adhesion.

Table 2.3: Contact angles and hysteresis of water, motor oil and hexadecane for different substrates after FDTMS coating (paper samples were etched for 60 min before coating with FDTMS).

Substrate	θ_{water} (°)		$\theta_{\text{motor oil}}$ (°)		$\theta_{\text{hexadecane}}$ (°)	
	static θ	hysteresis	static θ	hysteresis	static θ	hysteresis
Silicon wafer	110 ± 1	10 ± 1	81 ± 4	28 ± 4	74 ± 2	25 ± 2
10HW	140 ± 4	26 ± 5	120 ± 3	50 ± 5	113 ± 6	50 ± 2
10HW w/ debonder	150 ± 1	17 ± 2	155 ± 6	13 ± 2	141 ± 1	36 ± 5

If we assume that the contact angles on the flat silicon wafer represent equilibrium contact angles, we can use the measured apparent contact angles on the 10HW w/ debonder (60 minutes etched and FDTMS coated) to extract an estimated *L/D* ratio from the modified Cassie-Baxter model (Eq. 1.4). For all three test liquids, these estimated *L/D* values are shown in Table 2.4. Figure 2.2 illustrates that experimental uncertainty in equilibrium and apparent contact angle data leads to variations in estimated *L/D* ratios. For example, motor oil and hexadecane have lower equilibrium contact angles than water and thus exhibit lower sensitivity to the *L/D* ratio than water at apparent contact angles around 145° - 155°. Furthermore, a consequence of the larger standard deviation of measured contact angles for motor oil is that the estimated *L/D* ratio has the largest uncertainty. Nevertheless, considering the *L/D* values of all three liquids, it is reasonable to state that an average *L/D* ratio in the range 5 – 8 satisfies the modified Cassie-Baxter model, even though Eq. 1.4 is technically only valid for materials with a uniform structure of parallel, cylindrical fibers. In spite of the fact that paper substrates

are highly heterogeneous, the model provides good predictions of trends in wetting properties, and can thus be used as a guideline for the design of fiber-based surface structures.

Table 2.4: Estimated *L/D* ratios in 60 minutes etched 10HW w/ debonder with different testing fluids using the modified Cassie-Baxter model (Eq. 1.4).

Testing Liquid	***L/D* ratio**
Water	4.3 ~ 5.1
Motor Oil	7.9 ~ 22.9
n-Hexadecane	6.3 ~ 7.0

Further quantification of surface porosity changes after each treatment in the three-step process is essential for understanding the relationship between wetting and porosity on fiber-based substrates. Therefore, we used mercury porosimetry to investigate the distribution of pore sizes. The principle of mercury porosimetry is based on the fact that mercury does not wet most surfaces and thus will not penetrate into small pores unless sufficient external pressure is applied. If pores are assumed to be cylindrical, then the critical pressure *P* that forces mercury into pores is inversely proportional to the pore diameter *d*:

$$(\pi d^2/4)\, P = -\pi\, d\, \gamma \cos\theta_{eq,Hg} \qquad (2.1)$$

where γ is the surface tension of mercury and θ is the equilibrium contact angle of mercury on the sample surface, which leads to the Washburn equation: [124]

$$d = -4\, \gamma \cos\theta_{eq,Hg}/P \qquad (2.2)$$

For the present study, a contact angle $\theta_{eq,Hg}$ of 130° and surface tension of 0.485 N/m were used for mercury. Although the pores within a paper substrate are not cylindrical, the distribution of calculated pore diameters *d*, and changes in this distribution, still provide insight into the effect of processing parameters on surface porosity.

Figure 2.8a shows the cumulative intrusion curves of mercury, i.e. the total volume of mercury intruded into each gram of sample as a function of pore diameter. In order to understand the effect of both debonder and oxygen plasma etching on the surface porosity, 10HW samples with debonder were tested before and after plasma etching and compared with untreated 10HW. Based on the maximum intrusion volume, both debonder addition and plasma etching resulted in a significant increase of porosity, with the relative effect of 60 minutes plasma etching being larger than debonder addition.

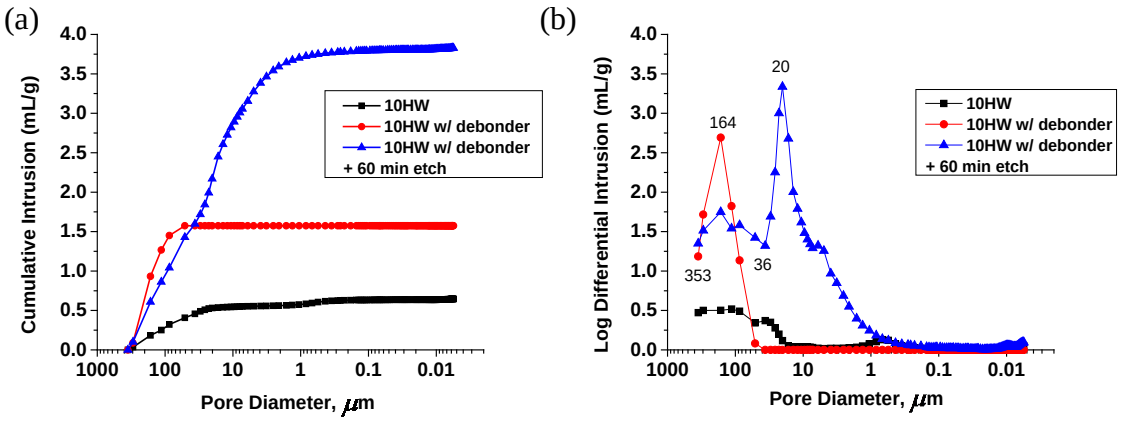

Figure 2.8: (a) Cumulative and (b) differential mercury intrusion curves for different substrates.

More detailed information of the pore size distributions is revealed by calculating the log-differential intrusion curve (Figure 2.8b). Even for untreated 10HW, which appears essentially non-porous under SEM (see Figure 2.4a), the mercury intrusion curve showed small yet broad peaks from 353 μm to 36 μm. Existence of such unrealistically large pores was also detected in other mercury porosimetry studies of paper; [125] this is likely an artefact due to the low pressure filling of interstitial void space between individual small paper samples in the sample chamber, which is interpreted by the software as internal pores. Furthermore, flexible and compressible materials such as paper can be compressed by mercury, which can also be interpreted as mercury penetration into pores.

In spite of these experimental challenges, upon debonder addition a sharp peak around 164 μm was observed. This could be explained by the opening of some fiber spaces after debonder treatment (see Figure 2.5). These inter-fiber spaces acts as pores during mercury intrusion, however, the peak values should be interpreted with caution because the intrusion process is not ideal as the model used for pore size measurement which assumes there are cylindrical pores. After 60 minutes plasma etching, a bimodal pattern was found with a slightly broadened peak around 164 μm and a new, sharper peak around 20 μm. The broader range of large pores (around 164 μm) and the creation of smaller pores (around 20 μm) are consistent with SEM images and the previously stated hypothesis that the handsheet porosity is increased during plasma etching through fines removal. More residual fines are removed and thinner fibers are created during plasma etching, which resulted in a broader distribution of large pores.

Wettability

After 60 minutes of plasma etching, fines blocking the inter-fiber pores were almost entirely removed and a high degree of amphiphobicity was established on the coated paper substrates (Table 2.3) made with debonder. We further investigated the effect of etch time on wetting, which is a direct consequence of dimensional changes of the fiber network. Since plasma etching has a negative effect on paper strength, it is important to strike a balance between paper strength and liquid repellency characteristics. The relationship between etch time and apparent contact angles for the different test fluids is displayed in Figure 2.9.

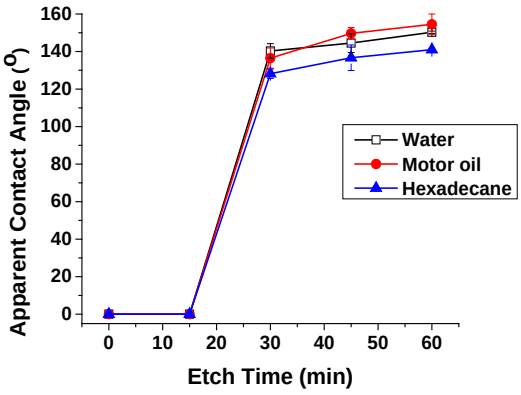

Figure 2.9: Contact angles of water, motor oil and hexadecane versus etch time for 10HW paper with added debonder after FDTMS coating.

The contact angles of all three testing fluids on unetched or 15-min etched paper were unstable (slowly absorbing liquid) and are thus denoted as 0°. After 30 minutes of oxygen plasma, all paper samples yielded a stable contact angle for all three liquids (no liquid absorption or significant contact angle changes within 20 minutes, except for

changes due to evaporation of water from the droplets); for etch times greater than 30 minutes, contact angles increased gradually with etch time. It should be noted that liquid droplet absorption rates after 15 minutes etching were slower than those for unetched samples for all three fluids. The lack of stable contact angles after 15 minutes of plasma etching is likely due to the inability of the oxygen etch process to completely remove fines from the pores at this short etch time. When liquid droplets come in contact with these unetched "islands", they can gradually be absorbed by the paper (see Figure 2.10a and 2.10b). However, 30 minutes of plasma etching is able to etch away fines from all surface pores (see Figure 2.10c). With this porous surface, stable liquid repellency was established on the 30 minute etched paper. According to our previous discussion regarding Figure 2.2, at an apparent contact angle ~150°, water is more sensitive to surface structure changes (*L/D* ratio) than is oil, so stable water contact angles should be achieved on paper at shorter etch times than those required for stable oil contact angles, which was also observed in our previous study. [34] Further increases in etch time gradually improve the anti-wetting properties, probably by further increasing the *L/D* ratio (see Figure 2.10d) and nano-scale roughness.

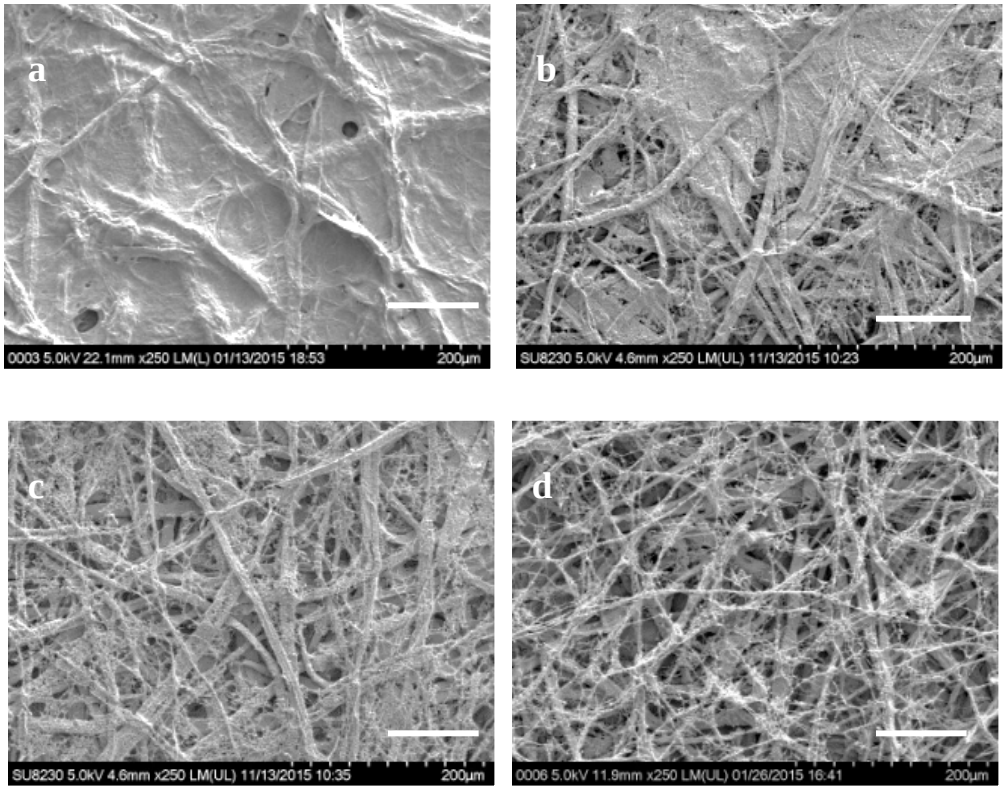

Figure 2.10: SEM images of paper made with debonder after (a) 0 minutes, (b) 15 minutes, (c) 30 minutes and (d) 60 minutes oxygen plasma etching. The scale bars represent 100 µm.

XPS Analysis

Table 2.5 shows the surface atomic concentration of untreated 10HW, 10HW made with debonder, and 10HW made with debonder after 60 minutes plasma etch and coating with FDTMS. Debonder addition does not have a significant effect on the atomic composition of paper. Considering that the debonder dosage is low (150 µl per gram of dry fiber) and only 8.5% weight of the debonder liquid is a quaternary ammonium compound, it is possible that the signal from N atoms of the active quaternary ammonium (C16-18 long chain) is below the XPS detection limit (ca. 1%). After FDTMS coating,

the fluorine surface concentration was close to 54%, while the oxygen content was greatly reduced and Si was detected.

Table 2.5: The XPS atomic concentration of untreated and FDTMS coated paper substrate (the last row shows the sample that was etched for 60 min before coating with FDTMS).

Substrate	debonder	FDTMS	Atomic concentration (%)				Stoichiometry ratio	
			C	O	F	Si	O/C	F/C
10HW	No	No	66.13	33.87			0.51	
10HW	Yes	No	66.31	33.69			0.51	
10HW	Yes	Yes	35.68	5.58	53.99	4.75	0.16	1.51

High resolution C1s spectra of these three samples are displayed in Figure 2.11. From the deconvoluted XPS spectrum of untreated 10HW (Figure 2.11a), typical signals for lignocellulosic materials are found: O-C=O at 288.5 eV, carbon bonding to one oxygen at 286.5 eV and C-C or C-H at 284.8 eV. While 10HW treated with debonder (Figure 2.11b) has nearly the same atomic surface composition as untreated 10HW (Table 2.5), their carbon bonding structures look rather different. Since the major components of the debonder are an ethylene oxide adduct of a vegetable oil and a propylene oxide adduct of a fatty acid, the most reasonable explanation for the abundant presence of O-C=O and C-O group is that the debonding agent has adsorbed to the surface, which gives rise to ester and ether functional groups.

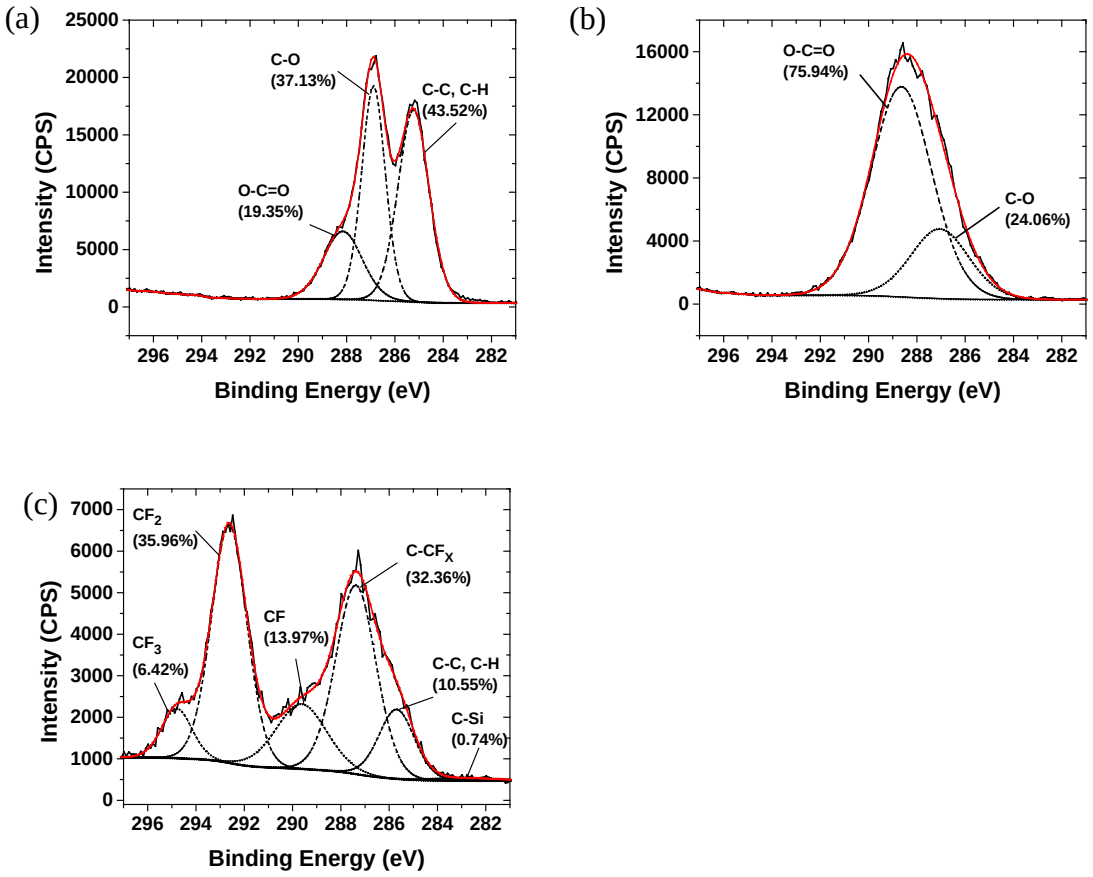

Figure 2.11: C1s XPS spectra of 10HW paper (a) untreated, (b) with debonder and (c) with debonder after 60 min etch and FDTMS coating. Values in parenthesis refer to the atomic percentage of C in the corresponding bonding state.

After 60 minutes oxygen plasma etching and FDTMS coating, $-CF_3$, $-CF_2$, -CF, C-C and C-H groups are detected in the C1s spectra, as expected (see Figure 2.11c). A small peak (282.9 eV) is also detected in the XPS C1s spectra, which can be attributed to C-Si bonds. The relative abundance of $C-CF_X$ indicates that the FDTMS film is highly cross-linked. This is also supported by the fact that the ratio of $-CF_2$ to $-CF_3$ is 5.6:1 while the FDTMS molecule has a theoretical $-CF_2$ to $-CF_3$ ratio of 7:1.

Mechanical Properties

Mechanical properties such as tensile strength are critical for potential applications of amphiphobic paper substrates. In the case of paper, elastic stiffness can be combined with tensile strength as a reliable indicator of bonding degree or bond strength. [126,127] It should be noted that the superamphiphobic paper produced in our previous research has loose surface fiber bonding and was too weak for tensile strength testing. [34] We describe below how tensile strength and stiffness of paper change with debonder addition, plasma etching and FDTMS coating (see Table 2.6). Here, the ZD tensile strength test is a destructive while ZD elastic stiffness test is non-destructive. The mechanical properties of standard copy paper (Econosource 8.5" × 11", 92GE/102 ISO) are included as a reference.

Table 2.6: Z-Directional tensile strength and elastic stiffness changes of paper after plasma etching and silane coating.

Substrate	Debonder	Etch time (min)	FDTMS	ZD tensile strength (kPa)	ZD elastic stiffness (× 1000 kPa)
Copy paper	No	0	No	317 ± 28	177 ± 11
10 HW	No	0	No	572 ± 76	302 ± 14
10 HW	Yes	0	No	400 ± 83	216 ± 9
10 HW	Yes	30	No	365 ± 62	106 ± 6
10 HW	Yes	30	Yes	359 ± 76	315 ± 46
10 HW	Yes	60	Yes	290 ± 28	232 ± 19

Handsheets prepared from highly refined pulp (e.g. 10HW) have a much higher strength and are stiffer than common copy paper. However, after the addition of debonder, both the ZD tensile strength and ZD elastic stiffness of the handsheets drop substantially. Thirty minutes oxygen plasma etching does not have a significant effect on the tensile strength of debonder added paper, but stiffness decreases. An FDTMS coating on the 30-min etched sample could not restore the tensile strength, but the stiffness of the coated substrate greatly increased. Although 60 minutes of etching and FDTMS coating yielded the best liquid repellency, this gain came at the expense of tensile strength and stiffness. The higher *L/D* ratio produced during prolonged plasma etching inevitability affects the bulk paper strength. However, these fully treated amphiphobic handsheets (debonder, plasma-etched for 60 min, FDTMS-coated) still possess tensile strength and stiffness that are comparable to copy paper. Mechanical strength requirements for specific applications will impose limits on the increase in *L/D* ratio (and structure) that are acceptable and thus affect the wetting behavior that can be achieved.

2.4 Conclusions

We have developed a facile method to fabricate highly amphiphobic paper with pulp debonder which to date has only been used industrially to enhance wetting and softness. Refining was needed to create fibers with smaller diameters, as predicted by the modified Cassie-Baxter wetting model. However, large quantities of fines accumulate in the pulp after high levels of refining. To minimize the negative effect of fines on the porosity and roughness of the paper formed after refining, pulp debonder was used to inhibit hydrogen bonding between fines and fibers. After debonder addition, the paper becomes softer and oxygen plasma etching further enhances porosity. Also, oxygen plasma etching increased

the surface roughness, which was confirmed by SEM images and profilometry. The paper strength after etching was quantified by Z-directional tensile strength measurements; in spite of the paper structure modification, the end product still exhibited comparable mechanical strength to copy paper. With a final step of fluorosilane coating, contact angles greater than 140° were achieved for water, motor oil and hexadecane. Debonder addition improved the liquid repellency of paper greatly through the removal of fines in the pulp. After detailed discussion of the factors that control the wetting of paper in this study, further research is underway to test coating durability and to further increase oil repellency of paper by optimizing surface coating materials and fiber sources. The approach described here to achieve a high degree of amphiphobicity on paper handsheets does not require sophisticated structural control, but uses a commercial debonder. The method thus enables scalable production of non-wetting paper through three simple steps: debonder addition to the pulp, followed by plasma etching and liquid-based fluorosilane coating. Development of low-cost amphiphobic paper would facilitate its potential use in medical testing strips, disposal clothes, lab-on-a-chip devices and liquid packaging, where inhibition of water and oil absorption is critical. Furthermore, the results in this study utilize debonder interactions with pulp for wettability control rather than their traditional use for improvement of water absorbency and softness.

CHAPTER 3

TWO-STEP PROCESS TO CREATE "ROLL-OFF" SUPERAMPHIPHOBIC PAPER SURFACES

Reproduced from L. Jiang *et al. ACS Applied Materials & Interfaces* 9.10 (2017): 9195-9203

3.1 Introduction

Most studies have achieved superamphiphobicity on substrates such as polymers, metals and woven fabrics through lithography, [28,128] laser ablation, [129] anodization [130-132] or nanoparticle coating methods. [133-135] The resultant surfaces often repel liquids with surface tensions above 27.5 $mN \cdot m^{-1}$ (hexadecane), while surfaces that can repel liquids with lower surface tensions are extremely rare and ones that can display roll-off behavior for those liquid are even rarer. [33,136,137] A few researchers have fabricated smooth surfaces (root-mean-square roughness < 1 nm) to enable liquids with surface tensions as low as 17 ~ 18 $mN \cdot m^{-1}$ to roll-off. [136,137] However, these methods are not applicable to surfaces that are inherently rough, such as fabrics, metal meshes and porous polymer membranes. Tuteja *et al.* have produced electrospun superamphiphobic surfaces that repel pentane (15.7 $mN \cdot m^{-1}$) through careful optimization of several design parameters. [33] For a randomly deposited electronspun fiber mat, surfaces with extremely low surface energy (14.0 and 11.1 $mN \cdot m^{-1}$) were required in order to achieve superamphiphobicity; to this end, the fibers were fluorinated which may compromise inter-fiber adhesion, although this property was not reported explicitly. Wetting

properties of surfaces based on different fabric morphology were compared, but effects of the micro- and nanoscale roughness were not explored. The same researchers also achieved superamphiphobicity on silicon wafers through precise control of surface morphology and surface chemistry. However, fabrication of these sophisticated structures is demanding with respect to both process technique and substrate material. Vollmer *et al.* have successfully fabricated a robust superamphiphobic coating on glass slides using candle soot as template, where even tetradecane (26 $mN \cdot m^{-1}$) rolls off the surface readily at tilt angles as low as 5°; [23] their method is applicable only to heat-resistant and flat surfaces.

Overall, previous reports have shown success in fabricating superamphiphobic surfaces on flat materials by incorporation of particles [26,100] or other techniques such as lithography [32,57,138] to establish roughness. However, studies that demonstrate repellency for liquids with surface tensions lower than hexadecane on non-flat substrates are extremely limited. Most reported methods have been developed for rigid polymer surfaces and metals, and are not applicable to paper manufacturing. [136,139-141]

In this chapter, we present a rapid, simple two-step method to fabricate superamphiphobic paper surfaces. Oxygen plasma etching is used to generate nanoscale roughness on fibers and alter porosity level by thinning the fibers. A thin fluoroalkyl trichlorosilane film (< 5 nm) deposited from the vapor phase reduces the surface energy of the paper substrate. The micro- and nano-scale roughnesses are varied systematically and possible synergistic effects are investigated without interference by variations in chemical modification. Our modified paper substrates are distinct from nearly all other superamphiphobic surfaces in that they retain similar mechanical impact properties to

those of untreated paper, and thus offer great potential for future applications where the strength and flexibility of cellulose and other fiber-based products are critical. The thin coating does not have a significant effect on air permeability. This approach minimizes the cost and material waste while ensuring outstanding liquid repellency with little effect on paper bulk properties.

3.2 Experimental Methods

Pulp Preparation and Paper Formation

Southern hardwood kraft fibers (Alabama River mill, Georgia-Pacific Cellulose Co.) were soaked in water overnight and then refined in a PFI mill for 6,000 revolutions according to TAPPI standardized method T 248 sp-08. Paper handsheets were subsequently formed following TAPPI standardized method T 205 sp-02 (denoted "6HW" in the following discussion).

Plasma Processing

Paper samples were placed in a 2.5 inch parallel plate (13.56 MHz) plasma reactor and etched for times between 15 and 60 min. Designations such as "15E" (etched for 15 min) will be used in the following discussion to specify the etch time used in the process. After the reactor has been evacuated to 0.01 Torr, oxygen was introduced into the reactor at 20 standard cubic centimeters per min (SCCM) and an equilibrium pressure of 0.5 Torr established. The etching process was conducted at 110 ℃ using a power of 120W. The rf power was provided at a frequency of 13.56 MHz. Additional details of the plasma reactor configuration can be found elsewhere. [142]

Vapor Phase Silanization of Fluorosilane

50 μl of (heptadecafluoro-1,1,2,2-tetrahydrodecyl)trichlorosilane (FDTCS, $C_{10}H_4Cl_3F_{17}Si$, Gelest Inc.) mixed with 150 μl toluene (Alfa Aesar, anhydrous, 99.8%) was placed in a 4 ml glass vial. The open vial along with the substrate, was placed within a 20 ml glass bottle. The bottle was uncapped and covered with an inverted beaker. During heating, the gap between the beaker and the bottle allowed fluorosilane vapor to be released as pressure was reduced. The silanization process was performed in a vacuum oven (VWR Scientific 1410 Sheldon Manufacturing, Inc.) at 100 ℃ and 88 kPa (26 inHg) for 15 min. In the following discussion, the vapor deposition of FDTCS is denoted "VD" to simplify the process description.

Coating on Silicon Wafer and Thickness Measurements

P type 100mm silicon wafers (Wafer World Inc.) were washed with acetone, methanol, isopropanol and dried with a nitrogen stream. Then the silicon was treated with an oxygen plasma for 2 min without heating before being coated with FDTCS. The vapor phase silanization of the flat Si wafer resulted in a rise in the water contact angle from 24° (untreated) to 111°, and a decane contact angle rise from 0° (not quantifiable) to 63°. The coating thickness was measured with J.A. Woollam M-2000 variable angle spectroscopic ellipsometer.

Static Contact Angle, Contact Angle Hysteresis and Roll-off Angle Measurements

All static contact angle measurements were performed by placing an 8 μl droplet of selected fluid (DI water, diiodomethane (Sigma-Aldrich Co., 99%), n-hexadecane (Sigma-Aldrich Co., 99%)), decane (Sigma-Aldrich Co., 99+%) and n-heptane (EMD Chemicals Inc, Omnisolv, 99% min) onto the paper. The images were recorded and analyzed with a Rame-Hart CA goniometer (model 290). Dynamic advancing and

receding angles were measured by increasing and decreasing the droplet volume, with an initial volume of 8 µl and step changes of 0.3 µl. The contact angle measurements were repeated five times for each fluid. For roll-off angle measurements, the solid surface was inclined from 0° to 90° using the tilting plate method to establish the tilt angle for roll-off; when the 8 µl droplet did not roll-off, a 20 µl droplet was tested as well. For each substrate-fluid combination, static contact angle and roll-off angle measurements were repeated at least 5 times. Commercial motor oil (SAE 10W-30, MotoTech) was only used in roll-off and non-sticky demonstration (see video clip in supporting information) rather than contact angle measurement because the composition and surface tension information (~ 30 $mN \cdot m^{-1}$) of this liquid are not accurately known.

SEM Imaging

Paper was sputter coated with Ag/Pd before introduction into the scanning electron microscopy (SEM) imaging system to mitigate charging effect. Images were taken with a Hitachi SU8230 cold field-emission SEM (Hitachi High-Technologies Co., Japan).

X-ray Photoelectron Spectroscopy

The elemental composition and chemical bonding information of the substrates were determined with a Thermo K-Alpha XPS (Thermo Fisher Scientific, West Palm Beach, FL) with a spot size of 400 µm at a vacuum pressure below 10^{-7} Pa. Thermo Advantage 5.934 software was used for curve fitting of the high resolution C1s spectra.

Air Resistance

The time needed for 100 ml of air to pass through the paper samples was used to evaluate air resistance according to TAPPI standardized method T 460 om-02 (Gurley

method). Five 50 mm square samples were prepared for each set of measurements using L&W densitometer (Lorentzen & Wettre USA, Inc.).

Tensile Strength, and Stiffness

Z-directional tensile strength of substrates was measured by Monitor ZDT (Testing Machines Inc., Model 84-22) according to TAPPI Standardized method T 541 om-10. The Z-directional elastic stiffness tests were performed by OPUS 3-Dimensional Ultrasonic System (Sonisys Inc.). For tensile strength and elastic stiffness, at least 4 measurements were performed for each experimental setting.

Dynamic Impact Durability

The substrate under investigation was tilted 45°, while 20.2 g oxide sand particles (colorful sand timer, Foxnovo Company) flowed out of a plastic funnel 20 cm or 40 cm above the substrate surface for 30 seconds. The diameter of the sand particles ranged from 80 to 120 μm.

3.3 Results and Discussion

Wetting Properties

In order to investigate only the physical effects of the fibers, we fabricated paper without additives. Before exposing the paper to the two-step process, all test liquids spread and absorbed into the paper immediately, giving contact angles below the detection limit of the equipment (denoted as 0°). After paper etching for 30 min using an oxygen plasma followed by a 15 min vapor phase silanization, test liquids with surface tension as low as 23.8 $mN \cdot m^{-1}$ (decane) could easily roll off the surface (see Figure 3.1).

Figure 3.1: Time-sequence images showing dyed water (blue), motor oil (yellow), dyed hexadecane (red) and decane (clear) (20 µl) rolling off the 30E + VD 6HW surface which was tilted from 0° to 90°. Motor oil was used instead of diiodomethane in the demonstration to avoid the density effect on "roll-off" behavior.

The effect of oxygen etching time on surface wettability was then investigated to determine the effect of roughness on wettability and roll-off behavior. Figure 3.2 shows contact angles data of droplets on oxygen plasma etched 6HW after fluorosilane vapor deposition. After 15 min of vapor deposition, paper surfaces are transformed from superamphiphilic (0° for all test liquids) to highly amphiphobic (even towards liquids such as hexadecane), thereby significantly improving the oil repellency of paper. Due to their low surface tension, droplet repellency for decane and n-heptane was not established until the etch time reached 30 min. After oxygen plasma etching for 30-60 min followed by vapor silanization, test liquids including decane could readily roll off the paper surfaces.

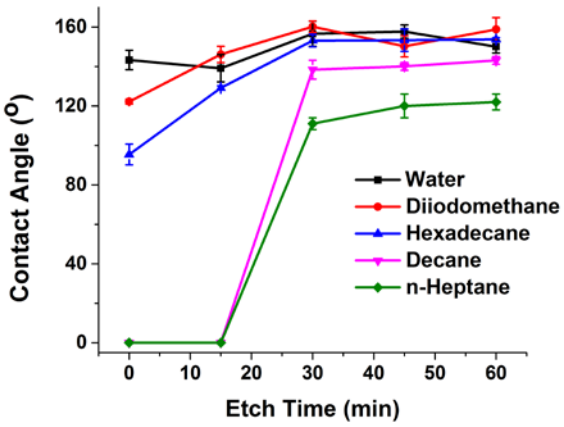

Figure 3.2: Liquid contact angle data on substrate with various etch time (the high evaporation rate of n-heptane may have caused underestimation of its contact angles).

The roll-off angles of all four test fluids on these substrates are displayed in Table 3.1. Due to extremely high volatility and thus evaporation of small drops of n-heptane, controllable roll off tests were difficult to perform; these results are therefore not included in the following discussion. Due to its high density, diiodomethane (3.32 g/ cm^3) rolls off more easily than water despite its lower surface tension, indicating the importance of gravitational effects for such high density fluids on porous adhesive substrates. Decane droplets of 8 µl do not roll off samples that were 30 min and 45 min etched and vapor deposited unless 20 µl volume were used. After 60 min oxygen plasma etching, water droplets roll off immediately and 8 µl decane droplets show movement on the surface. The contact angle hysteresis of water, diiodomethane, hexadecane and decane on 30E + VD sample are 5°± 3°, 6°± 2°, 8°± 4°, 17°± 5° respectively. The trend of hysteresis change is consistent with that of roll off angle showed in Table 3.1 (except for the case of diiodomethane due to its density effect in roll-off behavior). Since roll-off

angle measurement has been recognized as an alternative to contact angle hysteresis measurement [143] and offers a more direct description of surface self-cleaning properties (drop mobility) [144], only roll-off angles of the modified substrates are displayed in subsequent discussions. A 30 – 60 min oxygen plasma etch prior to fluorosilane coating ensures roll-off behavior for all test liquids, which indicates a wide morphology regime and thus processing/manufacturing window that retains Cassie-Baxter wetting behavior. To the authors' knowledge this is the first report of the achievement of similar wetting and adhesion properties, process latitude, and ease of fabrication of porous superamphiphobic surfaces without particle addition or generation.

Table 3.1: Roll-off angles for four test fluids on different superamphiphobic paper surfaces. Numbers are roll-off angles for 8 μl droplets unless 20 μl is indicated, which was used as secondary test when 8 μl droplets did not roll off.

Roll off angle (°)	Water	Diiodomethane	Hexadecane	Decane
30E + VD	11 ± 1	4 ± 1	8 ± 3	48 ± 3 (20 μl)
45E + VD	10 ± 1	2 ± 1	13 ± 1	48 ± 5 (20 μl)
60E + VD	2 ± 1	3 ± 1	10 ± 5	62 ± 3 27 ± 3 (20 μl)

Control of Morphology and Chemistry

The two-step process described above is illustrated in Figure 3.3. As is well-known, dual scale roughness and low surface energy are key aspects in fabricating superamphiphobic surfaces. In our process, we control the microscale roughness (micro-

porosity) and nanoscale roughness through plasma etching and modify the surface chemistry with a thin coating through vapor deposition. The modification of morphology and surface chemistry are essentially separate steps, which allows a wide range of process combinations, all of which result in amphiphobicity and in most cases, superamphiphobicity. In the following three subsections, fundamental changes in micro- and nano-scale roughness due to the plasma etch process, possible synergistic effects of dual scale roughness on anti-wetting and the role of the vapor deposition are discussed.

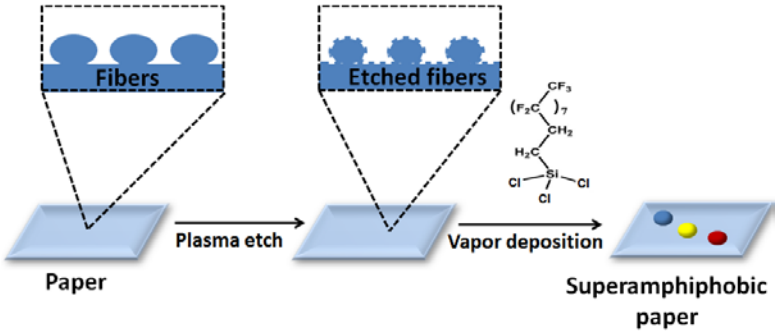

Figure 3.3: Schematic illustration of the process to fabricate superamphiphobic paper

Micro-scale Porosity

Previous wetting studies have shown that oxygen exposure time plays a major role in tuning the roll-off properties of paper. [34,142] Figure 3.4 displays changes in the morphology of paper surfaces due to plasma etch time. The surface porosity increased with increasing etch time because of selective etching of crystalline versus amorphous fiber segments, thinning of fiber diameter, and removal of fines (pulp particle that pass

through a 75 μm diameter round hole, mainly generated during refining in this study) that block pores between fibers. According to our previous study, [145] fines that remain in the paper sheet increase the liquid solid contact area and result in reduced liquid repellency. Oxygen etching for 15 min does not completely remove the fines that reside between the fibers, and thereby creates a sticky amphiphobic surface. When the etching time was 30 min, 45 min or 60 min, the surface porosity increased with fewer fines retained on the surface. This result is consistent with the wetting property changes presented in the previous section. Physical appearance of paper samples after various etching-coating processes are displayed in Figure 3.4f. Paper surfaces change gradually towards being transparent and thinner since more material was removed at longer etch times. However, 60 min etched and vapor deposited samples in this study still withstand repeated contact angle and roll-off tests (at least 10 tests) and maintain roll-off behavior after four months of storage in a closed sample case.

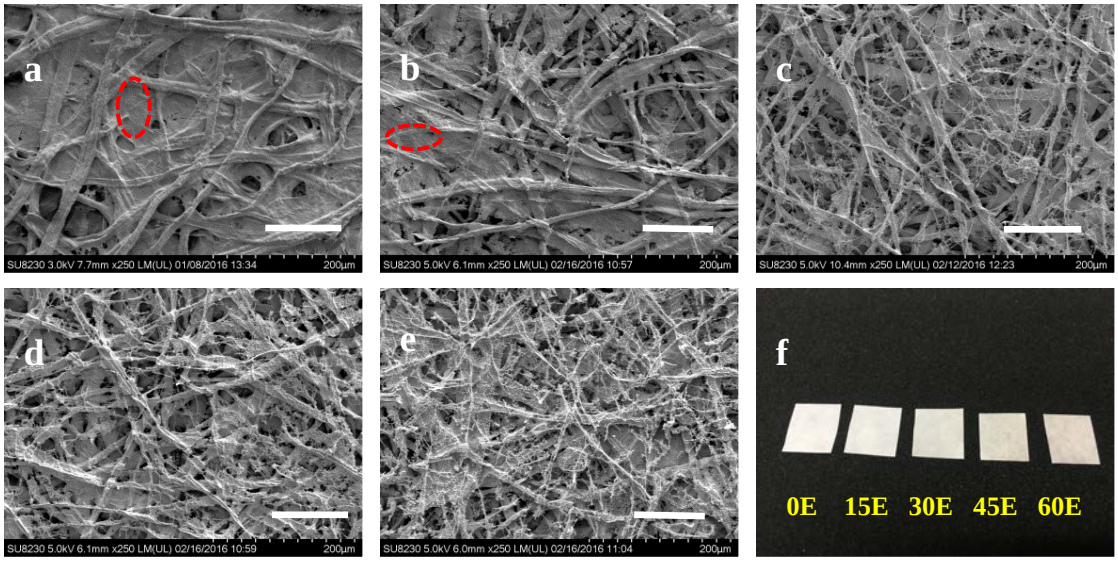

Figure 3.4: SEM images of (a) unetched, (b) 15 min etched, (c) 30 min etched, (d) 45 min etched, (e) 60 min etched 6HW after VD and (f) low-magnification visual examination of 6HW for a range of etch times, followed by VD. The scale bars represent 100 μm. Circled areas are examples where fines are covering the fiber network.

Nano-scale Roughness

Fiber roughness increased significantly through the selective etching of amorphous cellulose regions during oxygen plasma etching (Figure 3.5). Oxygen plasma etching for 15 min generated a rough pattern on fibers, while 30 min and 45 min of oxygen plasma accentuated the etched structure even more. Longer etch times of 60 min, on the other hand, began to smooth the etched structure. Quantification of nanoscale roughness changes on etched fibers was attempted with AFM. Limited information could be obtained due to the fact that paper is physically and chemically heterogeneous.

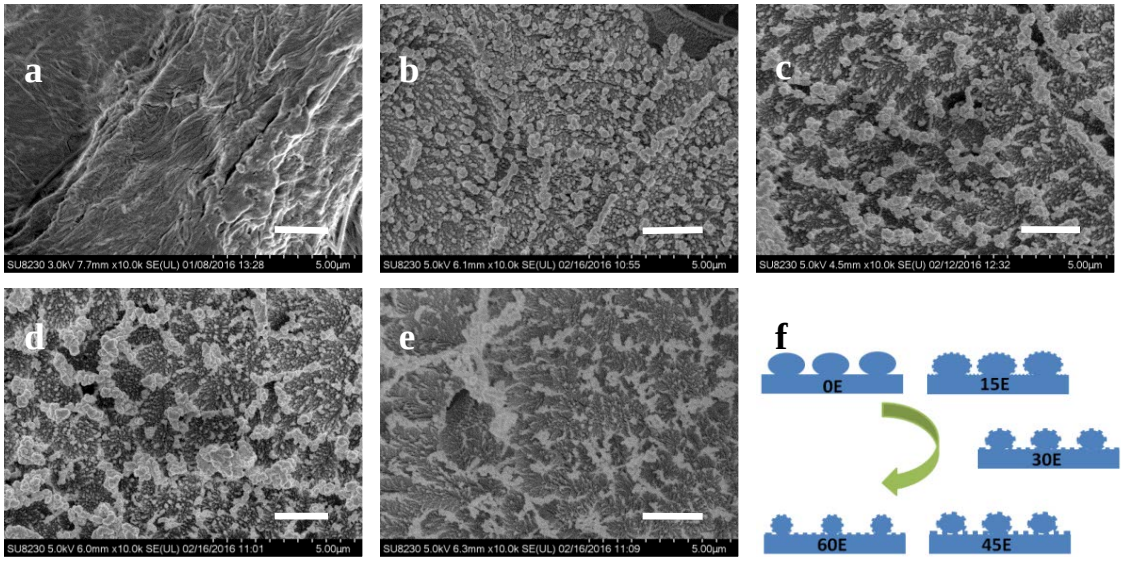

Figure 3.5: SEM images on a fiber of (a) unetched + VD, (b) 15E + VD, (c) 30E +VD, (d) 45E +VD, (e) 60E + VD 6HW and (f) schematic illustration of paper surface changes with various etch times. The scale bars represent 2 μm.

Based on SEM images of paper surfaces at both micro- and fiber-scale after various etch times (Figure 3.4a-e, 3.5a-e), Figure 3.5f illustrates schematically paper morphology changes with plasma etch time. Longer etch time reduces the fiber diameter gradually by preferentially removing amorphous segments, thus increasing fiber spacing. Thinner fibers combined with wider inter-fiber spacings have been shown to be beneficial to improve liquid repellency. [34-36] Such observations are consistent with increased contact angles and easier "roll-off" behavior that are observed with longer etch time.

However, the 60 min etched paper still displays better "roll-off" properties than other samples even with smaller nanoscale roughness. We thus infer that the nanoscale roughness alone does not determine the surface wetting properties. Similarly, neither will microscale roughness alone establish the wetting properties. After 45 min etch, paper

fibers have certainly become thinner (more material removed) and thus higher micro-porosity than 30 min etched paper, although there is no significant difference in their wetting properties. We therefore conclude that synergy exists between micro- and nano-scale roughness when designing superamphiphobic surfaces. Many researchers have found that hierarchical structures on surface are necessary for achieving superamphiphobicity, [133,146] and it has been reported that significant dominance of either micro- or nano- scale roughness will result in reduced superamphiphobicity. [147] Some studies claim that microscale structure is more beneficial for the achievement of superamphiphobicity than is nanoscale structure. [148] Clearly, the exact synergic effect between the micro- and nano-scale structures is not currently well understood, but an optimum combination, which depends upon the structure shape and surface chemistry likely exists.

Morphology and Chemistry Change after Vapor Deposited Coating

Direct measurement of the thickness of a coating on a heterogeneous fibrous substrate such as paper is difficult. Fluorosilane vapor deposition for 15 min results in 1 ~ 2 nm thick FDTCS coating on a flat silicon wafer which has had hydroxyl groups generated by a short plasma treatment. Figure 3.6 shows SEM images of 30 min oxygen plasma etched 6HW before and after vapor deposition. As expected, no visible surface morphology changes are apparent from the thin vapor deposited coating (compare Figure 3.6a with 3.6b, 3.6c with 3.6d).

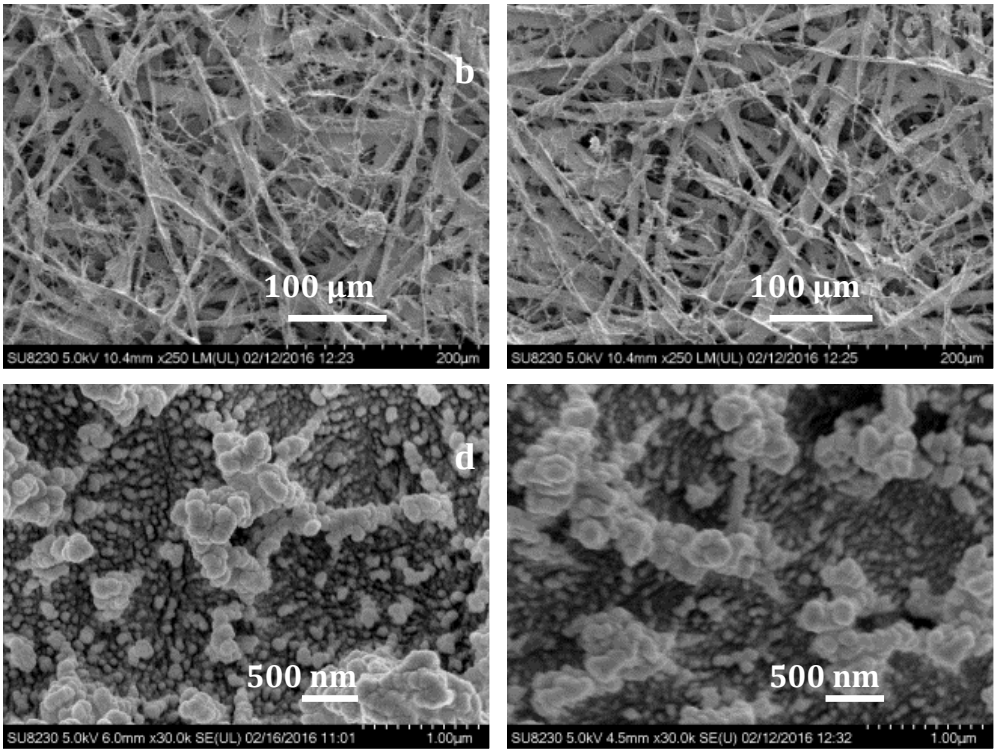

Figure 3.6: Low- and high-resolution SEM images of (a, c) 30E and (b, d) 30E + VD 6HW paper.

Chemical bonding structure changes before and after the two-step surface modification process was investigated using X-ray Photoelectron Spectroscopy (XPS). Thirty minute etched and vapor deposited samples were chosen for all further characterization studies because this sequence represents the shortest process time that yields high liquid repellency. Table 3.2 shows the atomic composition of paper before and after the treatments. A small amount of Cl and Si introduced by FDTCS are detected on the surface. According to the wetting properties of 30 min etched and FDTCS coated sample, the surface should be fully covered with FDTCS to be highly repellent to water and oil. In fact, oil will not roll off a surface that has coating defects. However, the high percentage of oxygen and low F/C ratio is not consistent with the atomic composition of

the coating material. This observation can be explained by the fact that the XPS sampling depth (~ 5 nm) is larger than the coating thickness (1 ~ 2 nm on silicon wafer as reference). Thus XPS sampled a range of composition on the treated sample that yielded a weighted average of the FDTCS layer and the fiber material beneath. The XPS result is consistent with the previous assertion that the coating is very thin (< 5 nm), and so will not affect the surface morphology significantly.

Table 3.2: XPS atomic concentration of 6HW before and after two-step process treatments.

Substrate	Atomic concentration (%)					Stoichiometry ratio	
	C	O	F	Si	Cl	O/C	F/C
6HW	65.4	34.6				0.5	
30E + VD	36.8	15.4	43.9	2.6	1.3	0.4	1.2

Figure 3.7 displays the high resolution C1s XPS spectra of the sample before and after the two-step treatment. Typical signals for lignocellulosic materials for untreated 6HW samples are: O-C=O at 288.5 eV, C-O at 286.5 eV and C-C or C-H at 284.8 eV (see Figure 3.7a). For plasma etched and FDTCS coated samples, detection of an intense C-O signal is additional evidence that the coating thickness is less than 5 nm (see Figure 3.7b). C-O bonds are not present in the coating material and thus should not be present on the surface which is highly repellent to both polar and non-polar liquids. XPS must therefore have detected the cellulose material beneath the coating. XPS signals for -CF_3, -

CF_2, -CF and C-CF_x were detected as expected. The presence of the relatively high concentration of C-CF_x is consistent with the fact that the CF_2 to CF_3 ratio in the film is 5.7:1 while the ratio is 7:1 for the precursor FDTCS molecule.

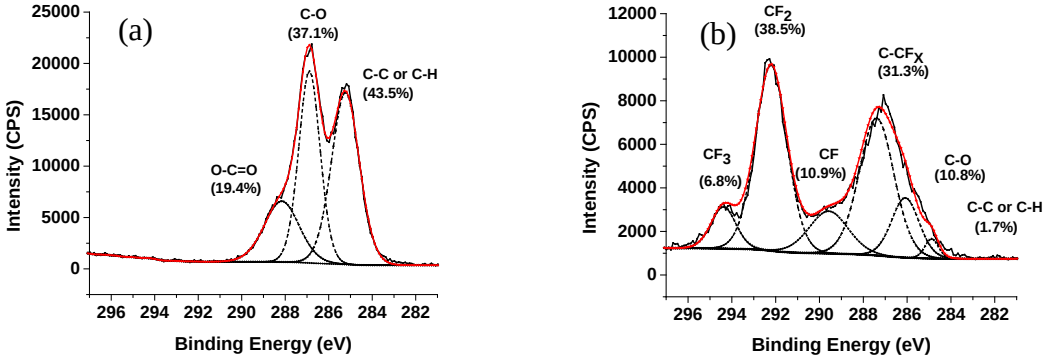

Figure 3.7: C1s XPS spectra of 6HW (a) before and (b) after the two-step process treatments.

Porosity and Mechanical Properties

Air permeability and mechanical properties of materials are critical parameters when considering applications such as packaging for low surface tension fluids (oils) and disposable medical apparel. Porosity (as indicated by air resistance) of copy paper (Staples multipurpose paper 8.5" × 11", 500/ream (513099-WH)), and 6HW before and after two-step process treatments (30 min etch, vapor deposition of FDTCS) were measured. The resulting air resistance values are displayed in Table 3.3. Copy paper was chosen as a commercial product reference since it has similar basis weight (70 ~ 80 g/m^2) and caliper (0.0031" ~ 0.0035") as the paper sheets fabricated in this study. Table 3.3 shows that copy paper has the lowest air resistance, while 6HW has a much higher value

(i.e. lower porosity) mainly due to decreased porosity after refining. Therefore, employing refined pulp to prepare superamphiphobic paper may allow the use of paper as a non-greasy packaging and liquid container in applications where higher strength and stiffness are required. As seen in Figures 3.4a and 3.4c, 30 min of oxygen plasma etching greatly increased the surface porosity of paper. This caused a substantial reduction in the air resistance of 6HW after the two-step process treatment. Since the coating is thin, the vapor deposition process does not cause a significant change in air resistance. As a result, the roll-off paper remains more air resistant than copy paper. The air resistance data of copy paper has the smallest standard deviation because much less time is needed for air to pass this material than the other samples. Heterogeneity was inevitably introduced in the paper making process for the laboratory-processed paper, which displays a higher standard deviation on less permeable samples.

Table 3.3: Comparison of air resistance for copy paper and 6HW paper before and after two-step process treatments.

Substrates	Time for 100 ml air to pass (sec)
Copy paper	10 ± 1
6HW	531 ± 70
30E +VD	127 ± 40

Table 3.4 shows that untreated 6HW shows a higher ZD tensile strength and elastic stiffness than copy paper mainly due to an increased level of fines bonding after

refining. According to Figures 3.4a and 3.4c, 30 min plasma etch and vapor deposition have only modified the first few layers of fibers, while most fibers beneath remain unchanged as is evident in those figures. Visual examination of paper transparency before and after two-step process treatments also supports the hypothesis that the oxygen plasma does not affect substrate bulk properties (Figure 3.4f). This observation is consistent with the fact that no significant change in paper ZD tensile strength was noted after 30 min plasma etching and vapor deposition. The decrease of ZD elastic stiffness is likely associated with reduced fine accumulation and increased surface porosity in the paper after oxygen plasma etching.

Table 3.4: Comparison of Z-Directional (ZD) tensile strength and elastic stiffness changes between copy paper and 6HW before and after two-step process treatments.

Substrates	ZD tensile strength (kPa)	ZD elastic stiffness (×1000 kPa)
Copy paper	322 ± 12	205 ± 28
6HW	393 ± 24	321 ± 16
30E +VD	375 ± 26	260 ± 20

Dynamic Impact Durability

Surface durability is an extremely important characteristic that determines the ability to use non-wetting surfaces in commercial applications. Despite its significance in nearly all potential applications, few studies have investigated the mechanical stability of

porous substrates after conversion to a superamphiphobic state. [97,149] A liquid repellent surface will encounter solid particle impact in applications where exposure to atmospheric conditions occurs. In this section, we describe interaction of our non-wetting paper surface with sand particles in dynamic impact tests that were selected to evaluate the mechanical robustness of the surface modification. [150] The sand particle impact test was performed at 20 cm and 40 cm height on 6HW samples that were etched for 30 minutes and vapor deposited, 30E + VD (see Figure 3.8b).

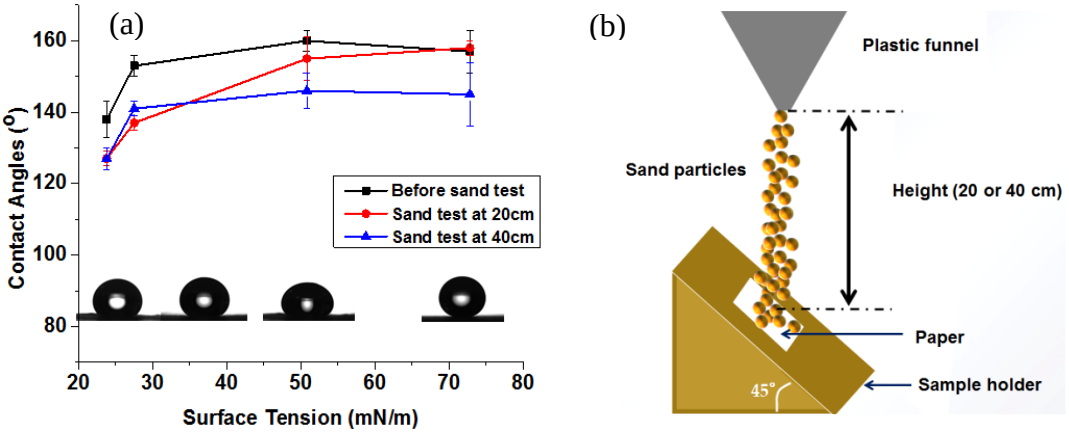

Figure 3.8: (a) Contact angles of 30E + VD 6HW before and after sand test at 20 cm and 40 cm height. Inset: 8 µl droplets (from left to right: decane, hexadecane, diiodomethane and water) on paper before sand test. (b) Schematic illustration of sand test.

Prior to the sand test, 30 min plasma etching and fluorosilane vapor deposition yields a paper surface with high liquid repellency (Figure 3.8a). A sand test at 20 cm height does not have a significant effect on contact angles of water and diiodomethane. However, the contact angles of low surface tension liquids such as hexadecane and

decane were reduced. When higher impact energy (sand at 40 cm) was employed, contact angles of hexadecane and decane maintain essentially the same as those for the paper tested at 20 cm. A slight decrease of diiodomethane contact angles compared with the original paper was observed even when standard deviation was considered. Roll-off measurements were also performed to confirm the change in paper wetting behavior after the sand test performed at different heights (Table 3.5).

Table 3.5: Roll off angles of test liquids on paper before and after sand impact testing. Numbers are roll off angles of 8 μl droplet unless 20 μl was indicated (20 μl was used when 8 μl droplet did not roll off).

Roll off angle (°)	Water	Diiodomethane	Hexadecane	Decane
Before sand test	11 ± 1	4 ± 1	8 ± 3	48 ± 3 (20 μl)
Sand test from 20 cm	2 ± 2 (20 μl)	6 ± 1	51 ± 2 (20 μl)	57 ± 1 (20 μl)
Sand test from 40 cm	20 ± 8 (20 μl)	10 ± 1	57 ± 2 (20 μl)	58 ± 4 (20 μl)

After the sand test from 20 cm, diiodomethane droplets roll off at 6°± 1° while water, hexadecane and decane droplets roll off at 2° ± 2°, 51° ± 2° and 57° ± 1° respectively, when droplet volume was increased to 20 μl. When a sand test was performed at 40 cm height, increased roll-off angles were observed for water, diidomethane and hexadecane. The samples maintained their roll-off properties although the contact angles decreased after sand tests. The contact angle and roll off angle measurements indicate that the sand test at 20 cm already caused changes on the paper

surface; a further increase in height apparently induced a few additional damages on the paper surfaces.

XPS analysis was used to investigate the cause of the decreased liquid repellency after sand tests (see Table 3.6 and Figure 3.9). Changes in surface chemistry are minimal and the observed differences are within the standard deviation of XPS measurements; several measurements were taken at different spots on the paper prior to the sand test. Apparently, no significant chemical damage was imparted to the paper surface since any coating damage should result in an increase of carbon and oxygen content (compared with 6HW in Table 3.2). The combination of XPS analysis and wetting properties indicate that the coating remains intact on the paper surface after the sand test from 20 cm.

Table 3.6: XPS atomic concentrations of FDTCS coated roll-off paper before and after sand tests at 20 cm height.

Substrates	Treatments	Atomic concentration (%)				
		C	O	F	Si	Cl
30E + VD	Before	36.8	15.4	43.9	2.6	1.3
	After impact test	36.5	13.3	46.8	2.1	1.3

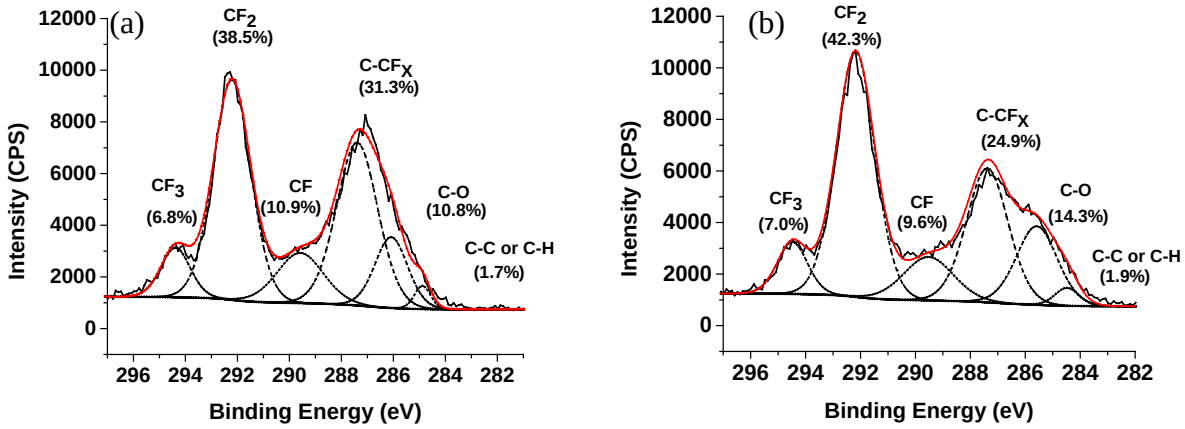

Figure 3.9: C1s XPS spectra of FDTCS coated "roll-off" paper (30E + VD) (a) before and (b) after sand test at 20 cm height.

SEM images were also taken on roll-off paper before and after the sand tests (20 cm and 40 cm) to determine if morphology changes had occurred that could affect the paper liquid repellency. Figures 3.10b and 3.10c reveal fiber fracture after sand tests from 20 cm and 40 cm. When liquid droplets come into contact with these fractured fibers, fiber structure and thus hysteresis will likely be degraded, which explains why 20 µl droplet volume instead of 8 µl was needed for water, hexadecane and decane droplets to roll off the surface after sand tests. While Figure 3.10e shows that there is no significant change of structure on fibers after sand tests from 20 cm, cracks were found on fibers when sand impact testing was performed from 40 cm high (see Figure 3.10f). Fractures in the fiber network at the micro-scale appears to be the main reason for the drop in liquid repellency after sand tests, and sub-micron destruction of fibers at greater sand impact testing height induce a further decrease in repellency.

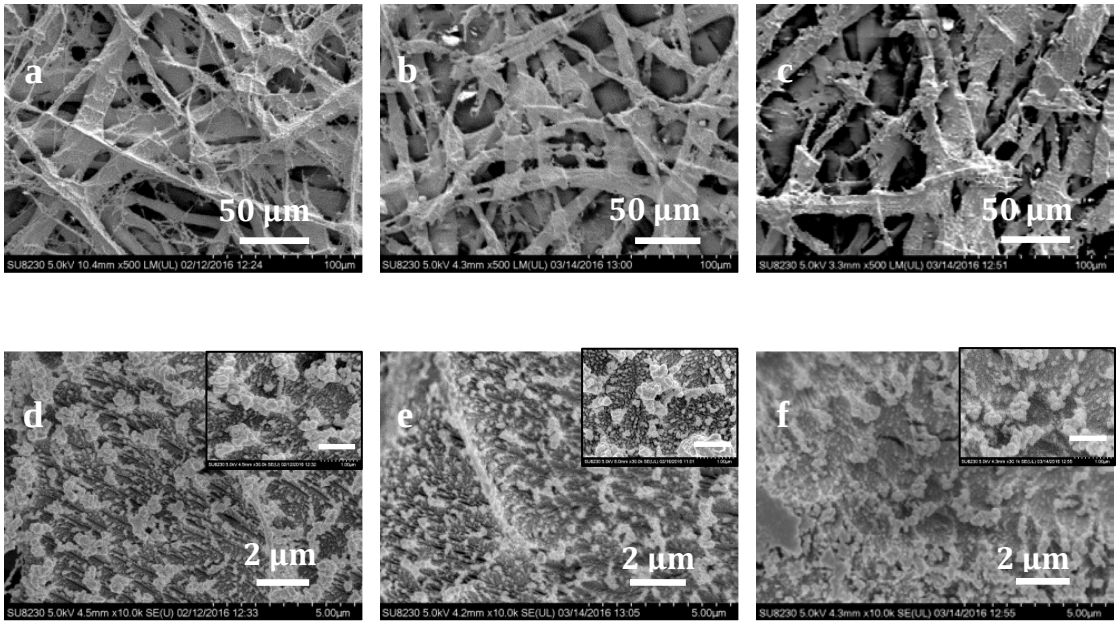

Figure 3.10: Low- and high-resolution SEM images of FDTCS coated roll off paper (30E + VD) (a, d) before sand impact test, (b, e) after sand impact test at 20 cm and (c,f) after sand test at 40 cm height. Inset: nano-scale roughness on fibers where scale bars represent 1 µm.

3.4 Conclusions

Fabrication of superamphiphobic surfaces has proven to be extremely challenging especially when the materials are porous and heterogeneous. The simple cost-effective two-step process described in this work achieves extremely high repellency even to low surface tension liquids such as hexadecane and decane (23.8 $mN \cdot m^{-1}$) and good repellency towards n-heptane (20.1 $mN \cdot m^{-1}$). This type of repellency is rare on inorganic and homogeneous materials, but even more unusual on porous and heterogeneous surfaces like paper. An oxygen plasma was used to generate nanoscale roughness and increased surface porosity through fiber thinning and paper fines removal. Combination of these properties with the naturally occurring re-entrant fiber structure and microscale

fiber size yielded a hierarchical structure on paper. To obtain the necessary surface chemistry, a thin fluorosilane layer was formed on the surface through vapor deposition. When the oxygen plasma treatment time was 30 min to 60 min, droplets of test liquids such as water, diiodomethane, hexadecane and decane roll off the surface easily. The extremely thin coating allowed the investigation of changes in wetting properties triggered by subtle changes in surface morphology. Neither durability of the coating surface nor adhesion with the underlying paper were degraded substantially after a sand impingement test, thereby indicating that these materials may offer extended liquid repellency in an array of applications. In addition, air permeability and mechanical strength of these roll-off samples were similar to those of copy paper. To our knowledge, the combination of the above-discussed properties (process simplicity, breathability, biodegradability, mechanical robustness, recyclability and coating durability) has not been reported for superamphiphobic surfaces, and especially for a commodity, porous product such as paper. Our findings offer insight into the critical design parameters involved in the formation of superamphiphobic surfaces. Ultimately, these results may lead to applications such as effective archiving of paper files, disposable wearable garments, and non-greasy food and liquid packaging with mechanically stable surfaces by using a simple, efficient production cycle.

CHAPTER 4

FABRICATION OF NON-FLUORINATED HYDROPHILIC-OLEOPHOBIC STAINLESS STEEL MESH FOR OIL-WATER SEPARATION

Reproduced from L. Jiang *et al. Separation and Purification Technology* 184 (2017): 394-403

4.1 Introduction

Recent oil spills in Alaska, the Gulf of Mexico, France and many other locations have highlighted the risks of environmental pollution that accompanies the development of industry and society. [151,152] The difficulties that were encountered during oil spill cleanup and the general challenges associated with post-treatment of increased volumes of oil-contaminated industrial wastewater underscore the critical need for energy-efficient systems to separate oil-water mixtures. Extensive investigations on the fabrication of porous substrates with special wetting properties have inspired the idea of separating oil-water mixture without applying high amounts of external energy. [53,145,153-156]

Numerous studies have been performed on the surface modification of porous materials to achieve special wettability properties that can be used for oil-water separation. Various hydrophobic-oleophilic material structures, including metal meshes, have been reported as potential oil-water separation solutions. [157-159] In these materials, the oil contaminant is absorbed, while water is rejected. The primary challenge for the application of these types of materials is fouling. [160,161] Throughout the

separation process, oil penetrates into the material and blocks the pores, which often results in a significant decrease in flux and overall performance after several operating cycles. More importantly, these materials are not suitable for *in situ* oil removal where the oil phase does not have sufficient contact with the hydrophobic-oleophilic separation system underneath because the higher density water forms a barrier layer between the oil phase and the oleophilic substrate. The prevailing substrates that have been explored are fabrics, sponges, metal meshes, foams, paper, carbon-based aerogels and powdered materials. [51,162-165] Although it is bio-degradable, paper lacks the mechanical strength necessary for large scale oil-water separation. For common bulk materials like sponges and foams, the urgent concern is their limited volume for absorption of oil or water [79]. When considering absorption capacity, carbon-based aerogels ranked the highest among these common materials. [79,166] However, the preparation processes for these materials are often complicated and cost intensive, and absorbent-based processes are usually batch-wise, which inherently limits fluid handling capacity.

The problems discussed above have drawn attention to the design of an alternative system that uses hydrophilic-oleophobic materials where the denser water passes through the substrate as filtrate in a continuous separation process, while oil is left in the retentate stream for collection and further processing. [167-169] Although the concept has many merits, finding suitable materials is challenging. Since oils commonly have lower surface tension than water, a hydrophilic surface usually also shows affinity to oil; similarly, oleophobic surfaces generally also repel water. Nevertheless, researchers have found several ways to design substrates with these unique hydrophilic-oleophobic wetting characteristics. [170-172] Among the materials listed above, metal meshes have the

advantages of reliable mechanical strength as well as easy recycle after use through remolding. Thus the fabrication of hydrophilic-oleophobic metal meshes with durable surface coatings and high water flux represents a very promising approach for oil-water separation.

Extensive research has demonstrated that surface wettability is determined by the synergistic effect of surface chemistry and morphology. [173-176] In addition, the existence of "re-entrant" surface structures has been found to be essential for establishing high repellency towards low surface tension liquids (e.g. oils). [12,35,37] Materials with cylindrical geometries such as metal meshes are therefore of particular interest; they have naturally occurring re-entrant structures due to the curvature of the bottom half of the filaments (fibers) that comprise the mesh. Good mechanical strength and well-defined, homogenous weave patterns are additional factors that make metal meshes a superb substrate for liquid-liquid separations.

When considering the design of porous substrates for liquid penetration or repellency, surface porosity and breakthrough pressure are important physical characteristics. [33,177] For meshes, the fiber diameter and inter-fiber spacing determine the surface porosity. While higher surface porosity yields higher permeation rates, the spacing cannot be infinitely large in order to repel low surface tension liquids. Choi *et al.* have introduced a dimensionless measure of surface robustness with design parameter A^* on a textured surface with cylindrical features. [177] The robustness factor A^* refers to the ratio of breakthrough pressure P_{BT} that is required for the transition from the composite interface to a fully wetted interface and a characteristic reference pressure P_{ref}

which is defined as $P_{ref} = 2\gamma_{lv}/l_{cap}$ where l_{cap} is the capillary length of the liquid (defined below). This model has been used extensively to evaluate the substrate resistance to liquid permeation. [33,35] The robustness factor is defined by:

$$A^* = \frac{P_{BT}}{P_{ref}} = \frac{2Dl_{cap}}{G^2}\frac{1-cos(\theta_{eq})}{1+2(D/G)sin(\theta_{eq})} \quad (4.1)$$

where $l_{cap} = \sqrt{\gamma_{lv}/\rho\, g}$, γ_{lv} and ρ are the surface tension and density of the testing liquid, respectively. θ_{eq} refers to the equilibrium contact angle of the liquid on an ideal flat surface of the same chemical composition and is given by Young's equation, [178] while *D* and *G* are the fiber diameter and inter-fiber gap respectively. In order for water to penetrate the surface but keep oil retained on top, $A^* >> 1$ for oil and $A^* < 1$ for water.

To achieve the desired surface morphology needed for wettability modification, most studies have employed superhydrophilic-superoleophobic materials that were fabricated via careful construction of rough structures on the surface using methods such as spraying nanoparticles [179,180] and growing nanowires. [181] One problem with this approach is that the artificial hierarchical structure can easily be damaged or destroyed; this causes the substrates to lose their oil-water separation ability after abrasion or application of mechanical stresses.

Most surface wettability modifications, especially for hydrophilic-oleophobic surfaces, employ fluorinated chemicals. However, there are growing concerns about the risks that fluorocarbons may pose to the environment. [45,84,182,183] Unfortunately, it is difficult to achieve oleophobicity without the use of fluorinated materials and/or complicated surface texturing and coating processes. Cao has coated various substrates

with non-fluorinated films (polydopamine and polyethylenepolyamine) to achieve hydrophilicity and oleophobicity for separating a mixture of water and hexane, but the coating process takes nearly two days to complete which limits large scale, low cost use. [184] Rohrbach demonstrated a successful separation of a hexane-water mixture using hydrophilic-oleophobic filter paper. [185] This process requires a long drying time and the water flux is low (89.6 $L \cdot m^{-2} \cdot h^{-1}$). A simple two-step dip coating process in paraffin wax and poly(dimethylsiloxane)-b-poly(ethylene oxide) (PDMS-b-PEO) diblock copolymer to fabricate functional filter paper was reported by Paul, but the water flux is too low (77 $L \cdot m^{-2} \cdot d^{-1}$) for most practical applications. [186] Moreover, paper is not a good candidate for large scale oil-water separation due to its low strength and susceptibility to fouling.

The goal of this chapter is to fabricate a mechanically stable stainless steel mesh for efficient oil-water separation using a non-fluorinated short chain silane via a simple immersion coating method. Previous studies on cellulose-based substrates have demonstrated that the presence of silanol groups on the coated cellulose surface can be controlled by adjusting sonication time of the liquid mixture before coating. [51] The premise of the manuscript is that this concept can be transferred to metal substrates: silanol groups from the hydrolyzed silane impart hydrophilicity to the surface, while the methyl groups lower the surface energy of the metal mesh and render the surface oleophobic. Thus, coated meshes can simultaneously display hydrophilicity and oleophobicity; these meshes can then be used to separate layered oil-water mixtures with high efficiency, and to pretreat oil-water emulsions to remove large oil drops. The relation between separation performance and the dimensions of the mesh is explored in

detail to enhance fundamental understanding. Without complicated construction of hierarchical structures on mesh surfaces, the coated substrate can withstand abrasion tests without performance loss. This straightforward, quick and cost effective fabrication process on stainless steel mesh offers the potential for application in large scale oil/water separation for cleanup of oil spills and wastewater treatment.

4.2 Experimental Methods

Coating Procedure

Corrosion-resistant type 304 stainless steel (SS) meshes with mesh numbers 100, 200 and 400 were obtained from McMaster-Carr; the mesh number refers roughly to the number of openings per inch (see Figure 1 for images and Table 1 for key dimensions). Meshes were rinsed with acetone, methanol and isopropanol and dried under a flow of dry nitrogen. Methyltrimethoxysilane (MTMS, Sigma Aldrich, deposition grade, ≥ 98%) was mixed with 0.1 M hydrochloric acid (Fisher Chemicals, 37.3%) in a 4:1 ratio and sonicated in an ice-water bath (Fisher Scientific ultrasonic cleaner model FS20, 70 W, 42 kHz) for 5 min to induce hydrolysis. The cleaned meshes were immersed in the hydrolyzed MTMS solutions for 2 min. After removal from the solution, excess liquid was removed from the mesh by touching the liquid with a piece of tissue paper (KimWipe, Kimberly-Clark Co). The coated meshes were finally air-dried under ambient conditions for 1 hour.

Contact Angle Measurements

All static contact angle measurements were performed by placing a 4 μl droplet of DI water, diiodomethane (Sigma Aldrich, reagent plus grade, 99%, surface tension 50.8 mN/m, density 3.32 g/mL, viscosity 2.8 mPa·s at 20°C) or motor oil (SAE 10W-30, MotoTech, surface tension 30.8 mN/m, density 0.87 g/mL, viscosity 138.4 mPa·s at 20°C) onto the surface; measurements were repeated five times. Images were recorded and analyzed by the standard software (Drop images, version 2.6.1) of a ramé-hart goniometer (model 290).

SEM Images and Optical Microscopy

Scanning electron microscopy (SEM) was performed on mesh surfaces with a Hitachi SU8230 cold field-emission SEM (Hitachi High-Technologies Co., Japan). The distribution of droplet size in emulsions was observed with an optical microscope (Olympus BX51) equipped with a digital camera (Olympus U-CMAD3). The image processing and analysis were performed with PictureFrame software.

X-ray Photoelectron Spectroscopy

The surface elemental composition and chemical bonding structures were obtained with a Thermo K-Alpha XPS (Thermo Fisher Scientific, West Palm Beach, FL) using a monochromatic Al Kα X-ray source at a pressure below 10-7 Pa. The spot size is 400 μm and the detection depth is ~ 5 nm. Thermo Advantage 5.934 software was used to curve fit (Gaussian-Lorentzian) and deconvolute the high resolution Si 2p spectra.

FTIR Analysis

FTIR analysis was conducted using a Nicolet iS-50 FT-IR spectrometer (Thermo Scientific, Inc) at ATR mode. The data collection was carried out by obtaining 64 scans at 4cm-1 resolution in the range of 4000 ~ 700 cm-1 using Omnic software.

Water Recovery Measurements

A clean empty glass vial was placed on a balance (Mettler Toledo, AB104-s/FACT) which was connected to a computer with customized LabVIEW data acquisition software for real-time data transfer every 0.5 second. The oil-water separation unit was placed upon the glass vial (see Figure 4.7b). The water-oil mixture was poured into the separation unit and collected in the glass vial beneath. The total weight change of bottle and the collected liquid was monitored for 30 minutes.

UV-Vis Spectroscopy

The content of motor oil in the filtrate was estimated using an Agilent 8510 UV-vis spectrometer with a cuvette path length of 10 mm according to a standard procedure. [185-188] A calibration curve for the adsorption peak intensity of motor oil (at 280 nm) at a series of concentrations was established using hexane as solvent. The absorption spectrum of the filtrate (shaken vigorously immediately before measurement) was recorded and the motor oil content was calculated based on the calibration curve. The efficiency of oil-water mixture separation was determined using equations described in the following section.

Oil-water Emulsion

Two sets of 10 ml oil in water emulsion (10:90 v/v for emulsion A, 30:70 v/v for emulsion B) were prepared by mixing water and motor oil using a Vortex Mixer (Fisher Scientific, 150 W, 50/60Hz) at 2240 rpm. Emulsion A was mixed for 1min, while emulsion B was mixed for 30 seconds. All emulsions were freshly prepared and used immediately.

Mechanical Durability Tests

For sand impact tests, coated mesh samples were mounted on a plastic board with 45° tilt angle using double-sided tape, while 20.2 g of sand particles (diameters ranging from 80 to 120 μm) were dropped from a funnel 40 cm above the substrate over a period of roughly 30 seconds. For the tape peeling test, 3M scotch tape was applied on the mesh surface and pressed firmly to ensure no notable air entrapment in between. Then the tape is peeled from one end of mesh and the peeling process was repeated 10 times. In abrasion test, the edges of the mesh were taped on the side wall of a clean glass jar (9 cm in diameter, 10 cm tall) with 60 g glass beads (abrasive blasting media, mesh size 60-120, McMaster-Carr) inside rotating at 1 rpm. The mesh was removed after 1 hr of rotation.

4.3 Results and Discussion

Dimensions of Meshes

Based on prior experimental and theoretical research on fibrous materials with cylindrical texture, in addition to surface chemistry the fiber diameter and inter-fiber spacing are expected to play a significant role in substrate wetting [34-36]. Thus SS meshes with different dimensions were studied to evaluate their wetting behavior and

resistance towards oil and water permeation. Contact angles on uncoated and coated flat 304 stainless steel plates were used to determine equilibrium contact angles that are needed to calculate robustness factors of different meshes towards water and motor oil. It should be noted that water spreads on coated stainless steel (flat) plates and the contact angle value is below the detection limit (~ 10°) of the goniometer. Thus the $\theta_{eq,water}$ on a coated surface was assumed to be 10° for the calculation of robustness factors to reflect the trend of A^* water as a function of mesh dimensions *D* and *G*. As can be seen from Table 4.1, all uncoated meshes have greater robustness towards water than to motor oil. After coating with MTMS, all meshes displayed an increased robustness against motor oil as well as extremely low resistance to water permeation. According to equation 4.1, small spacings *G* and large fiber diameters *D* are both desired in order to achieve a high robustness factor. Specifically, decreasing *G* has a larger impact on A^* values than does increasing *D*. From mesh 100 to 400, the calculated robustness factor towards water and oil increased with mesh number. Larger differences between the robustness factor towards water and oil promote improved separation of the mixture; thus, coated SS mesh 400 is the most promising substrate investigated in our hydrophilic-oleophobic material study.

Table 4.1: Dimensions and robustness factor for different meshes ($\theta_{water,eq}$ and $\theta_{motor,eq}$ are contact angles on a flat stainless steel plate; see also Figure 4.1 for definition of dimensions).

Mesh #	*D* (μm)	*G* (μm)	uncoated				Coated			
			$\theta_{water,eq}$	$\theta_{motor,eq}$	A^*_{water}	A^*_{motor}	$\theta_{water,eq}$	$\theta_{motor,eq}$	A^*_{water}	A^*_{motor}
100	114	140	96°	27°	13	1	< 10°	57°	0	4
200	54	74			24	2			1	8
400	26	38			46	5			1	14

Figure 4.1 shows SEM images of meshes before and after MTMS coating. It should be noted here that twill weaving was used on mesh 400 to provide a finer mesh while both mesh 100 and mesh 200 were constructed as plain weave. Differences in weaving pattern may have a slight effect on the wetting properties, but this was not investigated in this study.

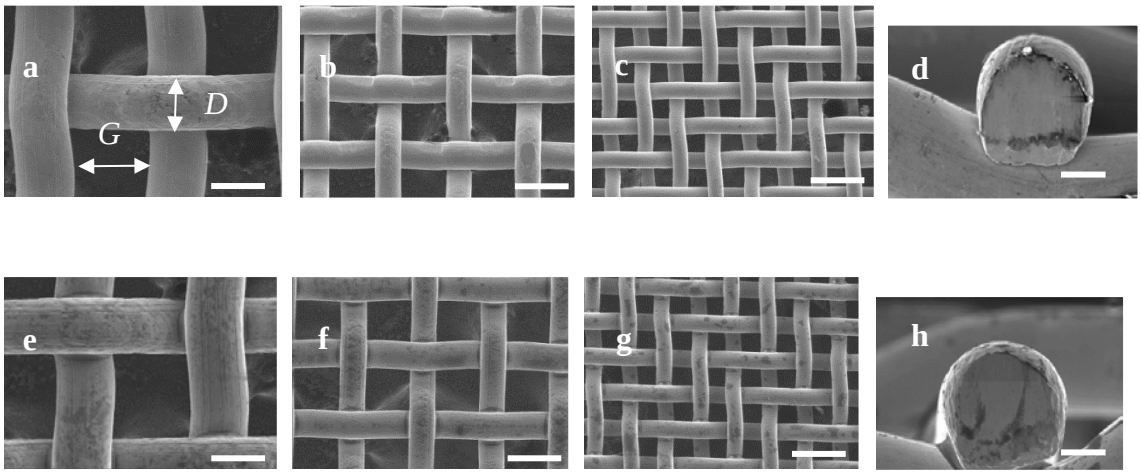

Figure 4.1: SEM images of (a) mesh 100 (b) mesh 200 (c) mesh 400 before coating and (e), (f), (g) after coating, respectively. Scale bars correspond to 100 μm. (d) and (h): cross section of fiber before and after coating on mesh 400 where scale bars represent 10 μm.

No notable change of surface morphology, fiber diameter or fiber spacing could be detected after coating which indicates a thin MTMS film. In addition, Figure 4.2 shows that there is no significant difference in the fiber diameter distribution before and after coating. It should be noted that the data displayed in Figure 4.2a differs 2 ~ 4 μm in size from the data provided by the manufacturer (see Table 4.1).

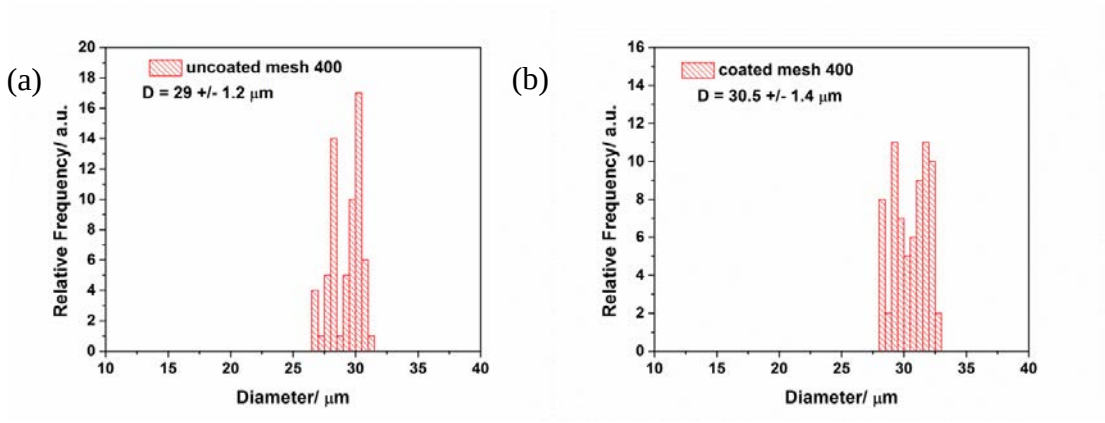

Figure 4.2: Fiber diameter size distribution of (a) uncoated mesh 400 and (b) coated mesh 400. The distribution information is obtained by analyzing SEM images of corresponding mesh samples with an imaging-processing program (ImageJ) where 100 spots were sampled.

The wetting properties on these meshes before and after coating were evaluated using contact angle measurements both in air and underwater. The contact angles in air are displayed in Figure 4.3 for water, diiodomethane and motor oil. Before coating, there is a slight increase of liquid contact angles from mesh 100 to mesh 400. Although mesh 100 and mesh 200 show no significant difference in water and motor oil contact angles, the high density of diiodomethane (3.32 g/cm^3) magnifies the subtle difference in liquid repellency because the stronger gravitational forces pull the droplet into the porous mesh. After coating, all meshes showed a substantial decrease in water contact angles and increase of oil contact angles, while no significant changes in contact angles of diiodomethane were observed on mesh 200.

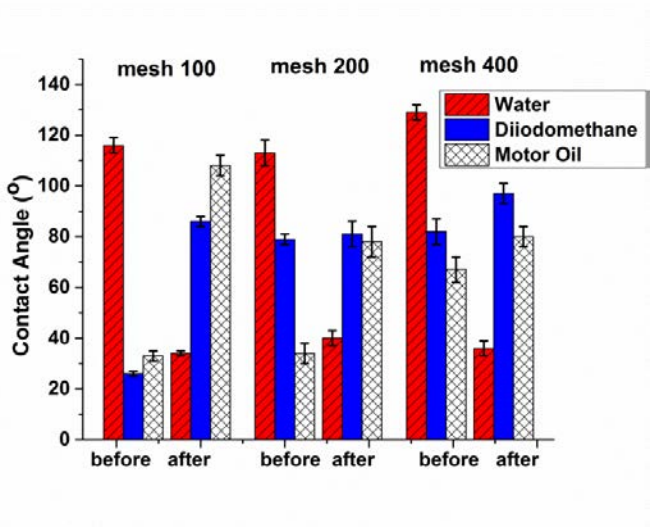

Figure 4.3: Apparent contact angles of liquids on different meshes before and after MTMS coating (in air).

Figure 4.4 shows water and motor oil droplets of different volumes on coated mesh 400. Water penetrates the mesh, with the droplet partially sitting on top of the mesh and partially suspended below. The water contact angle on top of the mesh was reduced when a larger droplet was used (Figure 4.4a-b), and water falls through the mesh when the droplet size exceeds 20 µl. Motor oil, on the other hand, remained on top of the coated meshes without penetration (Figure 4.4c-d) even when the droplet size was increased to 100 µl. Figure 4.4e presents a low-magnification view of large droplets sitting on uncoated and coated mesh 400. On the uncoated mesh, water forms a clear bead on the surface, while oil wets the surface following the rectangular pattern of the mesh with the underlying segment hanging down the mesh. After MTMS coating, the mesh is hydrophilic and can no longer support the 50 µl water droplet, leading to full water penetration. However, motor oil droplets of the same volume retain a spherical

shape on the coated mesh. Further evaluation of the performance of coated meshes in separation processes with high liquid flux will be presented in the next section.

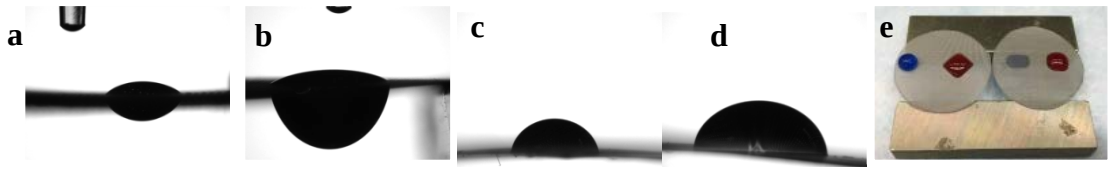

Figure 4.4: (a) 4 µl water droplet, (b) 20 µl water droplet, (c) 4 µl motor oil droplet, (d) 20 µl motor oil droplet sit on coated mesh 400 and (e) 50 µl dyed water (blue) and dyed motor oil (red) sitting on uncoated mesh 400 (left) and coated mesh 400 (right) in air.

In order to be used for oil-water separation, the underwater oil contact angle must also be evaluated to predict the separation performance of the mesh. Figure 4.5a shows the configuration used for underwater oil contact angle measurements where motor oil is injected onto an inverted mesh surface that is fixed to a horizontal copper support plate with stainless steel paper clips and immersed in the water reservoir. Before coating, all three meshes have underwater motor oil contact angles ranging from 115° to 130°. After MTMS coating, the underwater oleophobicity is increased for all meshes and reaches 163° for mesh 400 (see Figure 4.5b-d). Moreover, motor oil droplets do not stick to the coated mesh 400; a slight tilt of the surface (tilt angle 2° ± 1°) causes the oil droplet to roll along the surface. Mesh 400 thus clearly displays hydrophilic and underwater superoleophobic properties; its oil-water separation performance will be investigated in detail in the following sections.

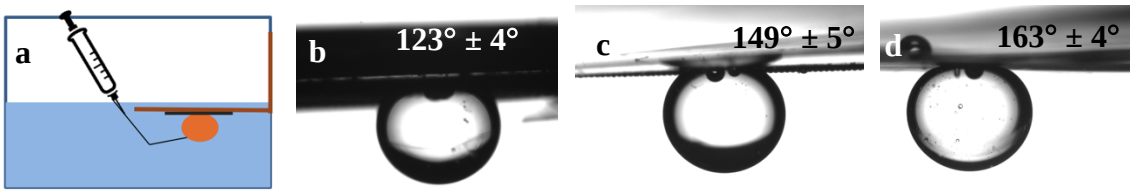

Figure 4.5: Set-up for underwater oil contact angle measurements and optical images of underwater motor oil droplets on inverted, MTMS-coated (a) mesh 100, (b) mesh 200, and (c) mesh 400.

Separation of Oil-water Mixtures

The oil-water separation apparatus is shown in Figure 4.6. The mesh to be tested was cut into 25 mm diameter circular samples, and secured between two glass fixtures using a clamp and O-ring seals. The inner diameter of the upper glassware is 16 mm while the diameter of the downstream flow channel is 7 mm. Mixtures of 7 ml water and 3 ml motor oil were prepared and poured down the column under the force of gravity. Without MTMS coating, water does not permeate through the meshes, as predicted from their high robustness factor towards water before coating (see Table 4.1). The oil phase cannot come into contact with the mesh due to the density difference with water, which leaves water as a barrier between the oil layer and mesh.

For coated mesh 100, water flows through the mesh within seconds, with oil following quickly thereafter. Although it displayed the highest motor oil contact angle, coated mesh 100 did not resist the oil flux, probably due to the low robustness towards oil. With coated mesh 200, water penetrated rapidly while motor oil remained on the mesh for a few seconds and then dripped down slowly (~ 5 minutes were needed for all oil to pass) compared to the flowrate of oil through coated mesh 100. For the coated mesh

400, in contrast, water permeated the mesh within seconds, leaving the oil on top of the mesh (see Figure 4.6). A gradual increase of resistance towards oil flux occurs from mesh 100 to mesh 400 which is consistent with their increased robustness factor towards motor oil while water permeated all coated meshes without noticeable flow resistance.

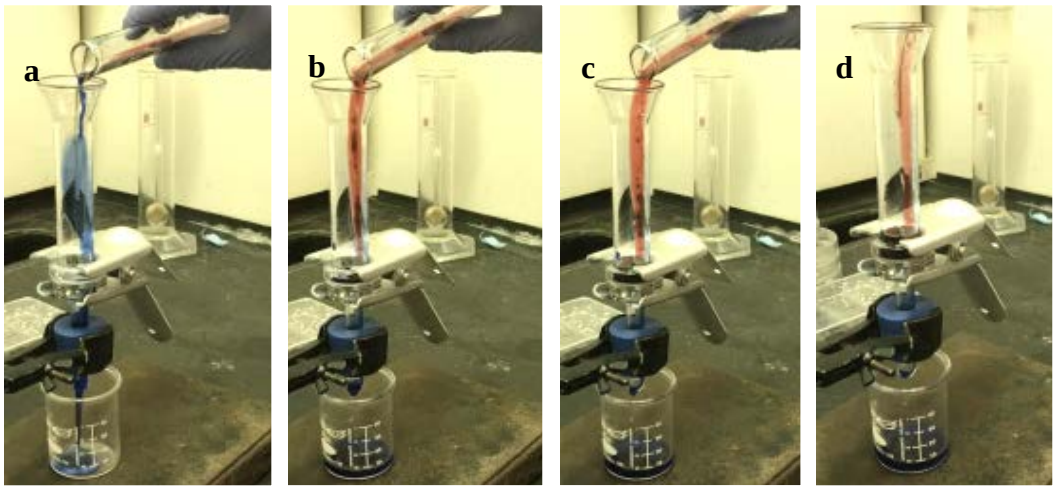

Figure 4.6: (a-d) Time-sequence images of separating layered motor oil (dyed red) - water (dyed blue) mixture using coated mesh 400

Since mesh 100 and mesh 200 do not have the ability to separate oil-water mixtures, only the performance of coated mesh 400 was further quantified. Figure 4.7 shows the result of water recovery measurement and the apparatus used. An immediate increase in weight was observed when the oil-water mixture was poured into the separation apparatus. Only ~ 1 s was needed to complete the separation process of a 10 ml mixture (see Figure 4.7a), and no further liquid dripping was observed during 24 hr of observation. The water recovery was 91.1% where water was mainly lost due to wetting

of the walls of the glassware and mesh; the water recovery increased to 95.4% when a larger mixture volume was used (10.5 ml water with 4.5 ml motor oil). Water fluxes as high as 7.16×10^4 $L \cdot m^{-2} \cdot h^{-1}$ were measured, which is remarkable for such low driving forces. The water flux reported previously for oil-water separation usually ranges between 10^2 and 10^4 $L \cdot m^{-2} \cdot h^{-1}$, where most of studies use varying levels of feed pressure that can greatly exceed gravitational forces. [189-191] Even for gravity-driven experimental systems, the hydrostatic driving force is usually higher than in our experiments. We poured a 10 ml mixture into the system, with liquid height never exceeding 3 cm due to the rapid water flow through the mesh. In some previously reported studies, the liquid height was either set at 10 cm, or fixed volumes as large as 200 ml were used, although in some cases, the volume was not specified. [192-194] Clearly, the coated meshes combined with gravity-driven flow provide an energy-efficient solution to oil-water separation while maintaining high water flux.

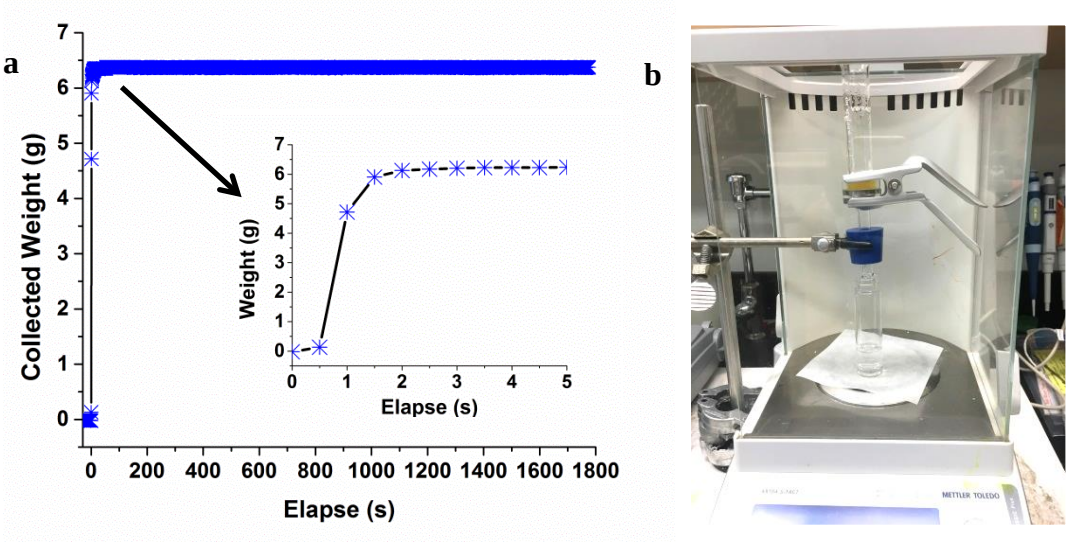

Figure 4.7: (a) Weight of collected liquid as a function of time elapse (t =0 represents the time at which the mixture was poured into the system) and (b) separation apparatus for water recovery measurement.

The separation efficiency was characterized via UV-vis spectroscopy measurements of the filtrate; no oil was detected visually. Figure 4.8 shows absorption curves of motor oil-hexane mixtures of known concentration, in which a distinct peak at 280 nm is evident (typical of mineral oil). [186,195] The relationship between the absorption intensity at 280 nm and oil concentration was defined by a linear fit (absorbance = 0.6067 × oil conc. [mL/L] with R^2 = 0.9899). The absorption curve for the filtered water overlaps with the clean DI water control sample and shows no significant peak at 280 nm.

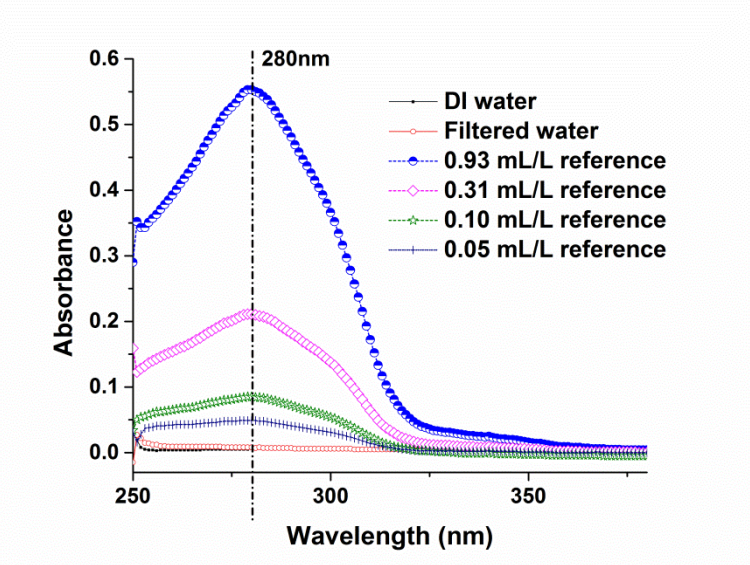

Figure 4.8: UV-vis absorption spectra of motor oil in hexane with different concentrations, filtered water and reference water.

The oil concentration in the filtered water was calculated using the calibration curve; the separation efficiency was defined by equation 4.2. [185-187]

$$\text{Separation efficiency} = \left(1 - \frac{C_f}{C_i}\right) \times 100\% \qquad (4.2)$$

where C_f is the motor oil concentration in the filtered water and C_i is the initial concentration in the feed. The separation efficiency of coated mesh 400 was calculated to be higher than 99.99%. After being immersed in water for a week, the coated mesh 400 could be reused for effective oil-water separation; no notable drop in separation efficiency (remains 99.99%) and water flux (less than 0.5% change) was observed.

Separation of Motor Oil/Water Emulsions

Stainless steel mesh 400 coated with MTMS showed excellent separation efficiency for rapidly demixing layered oil-water systems. However, industrial wastewater and oil spills often contain both poorly mixed, layered oil-water mixtures and emulsified oil droplets. Generally, substrates with relatively large pores do not have the ability to achieve complete separation of oil-water emulsions in which oil droplet diameters typically range from approximately 10 nm to 100 μm. Tuteja *et al.* investigated a fluorinated stainless steel mesh which they reported to separate both oil-water mixtures and emulsions. [177] However, smaller droplets in the emulsion passed through the pores of their mesh, so that a complete separation of oil-water emulsion could not be achieved. The inability of mesh substrates to prevent small droplets in the emulsion from transporting through the pores limits their oil-water separation applications. However, these systems can be incorporated into oil-water separation units as an efficient primary separation step, thereby reducing the workload on subsequent fine separation subunits by eliminating layered oil phases and larger oil droplets. Stainless steel meshes are cheap and mechanically strong, and the coating method described in this study is rapid, low cost and uses non-fluorinated coatings. We tested the ability of mesh 400 to separate droplets in the emulsion that are larger than the pore size; these results are shown below.

It must be noted that before coating, the emulsion cannot penetrate the hydrophobic mesh. The hydrophilicity of the coated mesh is crucial for separating the bulk water phase from the large oil droplets. To confirm the oil droplet screening effect of the coated mesh, two sets of emulsions were prepared. Mixtures with different ratios of motor oil and water were subjected to shear for varying amounts of time to generate

emulsions A and B with different droplet size distributions (see experimental methods for details). All emulsions were freshly prepared and poured into the separation column immediately without the use of surfactants for stabilization. Coated mesh 400 (38 μm square pores) was used to separate these emulsions.

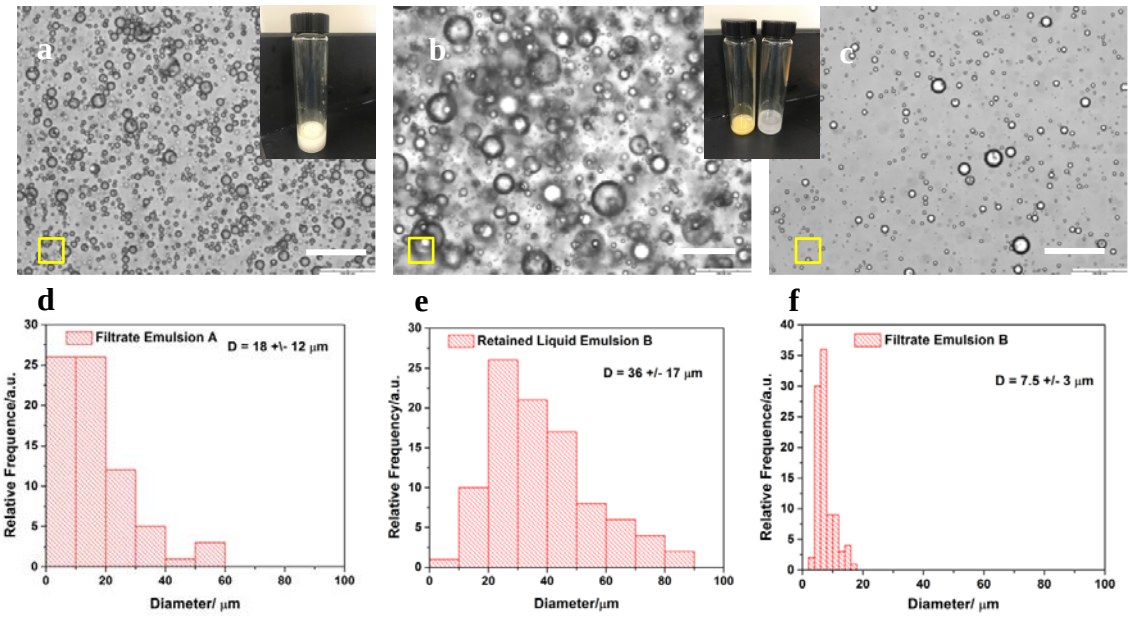

Figure 4.9: Optical microscope images and respective oil droplets size distribution of (a,d) filtrate from emulsion A, (b,e) retained liquid and (c,f) filtrate from emulsion B using coated mesh 400. Inset: visual image of filtrate from emulsion A (left), retained liquid and filtrate from emulsion B (right). Scale bars represent 100 μm, while the squares are to-scale representations of the pores of mesh 400. The distribution information is obtained by analyzing optical images of corresponding samples with an imaging-processing program (ImageJ) where 100 droplets were sampled and characterized.

Emulsion A passed through the mesh unhindered and no liquid was retained by the mesh; a picture of the filtrate is displayed as the inset in Figure 4.9a. Mesh 400 has no ability to separate emulsion A, which is not surprising, since the optical micrograph and oil droplets size distribution of the filtrate from emulsion A shows that the droplets are

small enough to pass through the 38 μm mesh pores. In Figure 4.9d, few oil droplets with diameter slightly larger than 38 μm (mesh pore size provided by the manufacturer) were found in the filtrate of emulsion A. This is likely to be caused by the coalescence of smaller oil droplets during the delay before optical imaging. However, the result should only be used as a reference to demonstrate the size-exclusion effect of the coated mesh in emulsion separation and not be over-interpreted since the number of sampled droplets will never be enough to represent the whole picture of the sample fluids. Coated mesh 400 was able to separate emulsion B into an oily retentate and a semi-transparent filtrate; the retained liquid consists of mostly large droplets and some attached smaller droplets (see Figure 4.9b), while the filtrate only contains droplets that are smaller than the pore size, i.e. 38 μm in diameter (see Figure 4.9c and f). The result is consistent with our previous assumption about the separation capability of coated mesh 400 with respect to emulsions. Its separation efficiency at high fluxes for layered oil-water mixtures and oil droplets with diameters larger than 38 μm from emulsions qualifies the mesh as a primary subunit in an oil-water separation process.

Surface Analysis

To investigate the changes in surface chemistry of the metal mesh before and after MTMS coating, XPS was performed on a stainless steel plate since the diameter of mesh fibers is smaller than the XPS beam size. According to previous research, methoxy groups are substituted with hydroxyl groups in a stepwise way during fast MTMS hydrolysis under acidic conditions and sonication. [196-198] The hydrolyzed MTMS then undergoes a condensation process to form dimers and oligomers which form hydrogen bonds with the surface. Since condensation is a relatively slow process

compared to hydrolysis, the extent of MTMS condensation can be controlled by adjusting the sonication time. Our previous studies indicate that the concentration of polar silanol groups on the MTMS-coated surface can be varied through sonication time, and that this provides control over the hydrophilicity of the coated surface. [51] Specifically, at short sonication times (5 min), dimers and linear oligomers with methyl side groups form in solution; after coating, unreacted silanol groups become the dominant surface species, which results in a unique hydrophilic-oleophobic surface.

The treatment fully covered the metal surface with MTMS, since no Fe signal was detected on the coated surface. High resolution Si2p XPS spectra were taken to obtain more detailed information on surface chemistry (see Figure 4.10a). No verifiable peaks were detected on the original stainless steel plate, consistent with the absence of silicon in stainless steel. However, after the MTMS coating process, a large XPS peak between 103.2 eV (SiO_2) and 102.8 eV (fully crosslinked $Si(CH_3)O_{1.5}$) was present. [199,200] This indicates that the MTMS species are not yet fully crosslinked and that MTMS dimers and oligomers are present on the surface. [51] As a result, the surface is rich in silanol groups that render the coating hydrophilic.

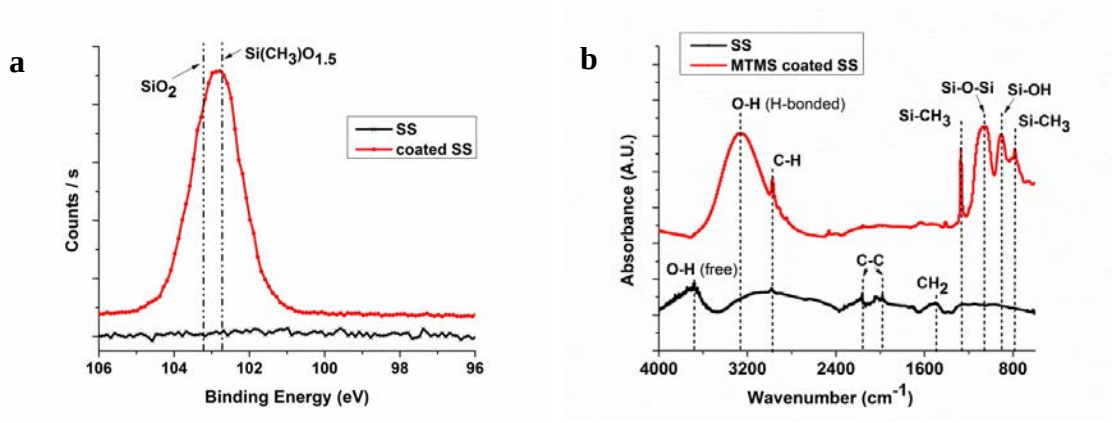

Figure 4.10: (a) Si2p XPS spectra on stainless steel plate before and after coating with MTMS and (b) ATR-FTIR of stainless steel plate before and after coating with MTMS

ATR-FTIR was also used to obtain further details about the surface chemistry changes resulting from MTMS coating (see Figure 4.10b). The original stainless steel shows small peaks corresponding to C-C and C-H bonds, which can be ascribed to carbon contamination during atmospheric exposure and sample storage. [201] Free hydroxyl groups, which can react with hydrolyzed silanes, are also present on the surface. After MTMS coating, four signature peaks of silicon bonding appear on the surface. Peaks at 1270 cm^{-1} and 782 cm^{-1} both result from Si-CH_3 bonds, and the peak for Si-O-Si at 1050 cm^{-1} indicates that there is a condensation reaction between MTMS molecules, while the existence of O-H (3280 cm^{-1}) and Si-OH (904 cm^{-1}) bonds establishes that the MTMS in the coating has not been fully crosslinked. [202]

Mechanical Durability

Depending on the complexity of the original source, wastewater often contains particles and other impurities. When oil spill cleanup is desired, sand particles are always

present, which enhances the separation difficulty. Although pretreatments can be performed to remove most of these solid compounds, residual particles could still affect the separation performance. We therefore performed a sand impact test on the coated mesh 400 and measured the resulting wetting properties and oil-water separation ability to assess the effect of exposure to sand.

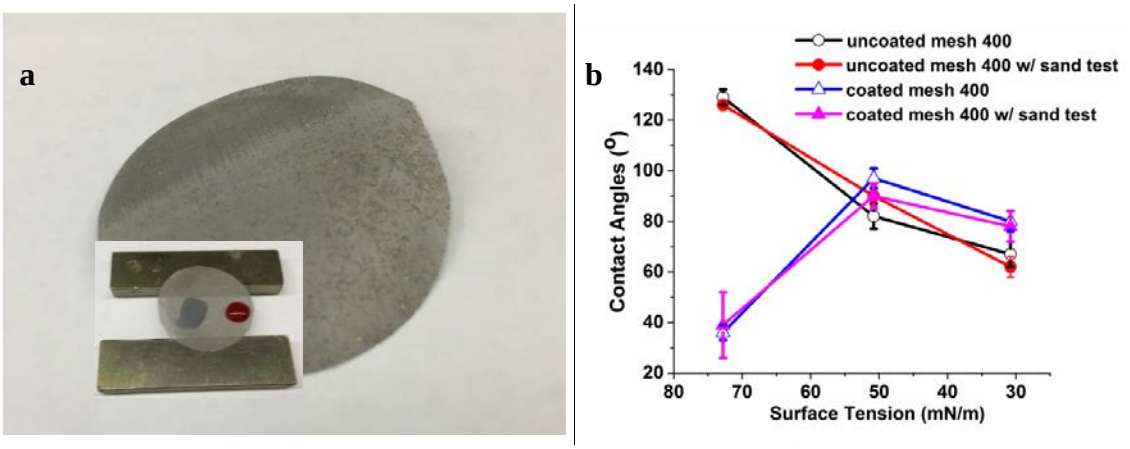

Figure 4.11: (a) coated mesh 400 after sand test (inset: 50 µl dyed water (blue) and dyed motor oil (red) sitting on coated mesh 400 after sand test) and (b) contact angles of liquids on uncoated mesh 400 and coated mesh 400 before and after sand test.

As displayed in Figure 4.11a, sand particles remained stuck to the coated mesh surface after sand impact testing. The strong adhesion forces between sand particles and the surface could be caused by the polar groups contained in the coating, since no sand was attached to an uncoated mesh after sand tests. However, water droplets still penetrated the mesh. Also, oil droplets were still repelled by the coated mesh after the sand test. Detailed information on contact angle measurements is presented in Figure 4.11b. The sand test does not have a measureable effect on contact angles of uncoated

and coated meshes, although a larger standard deviation of water contact angles was observed after the sand test on coated meshes.

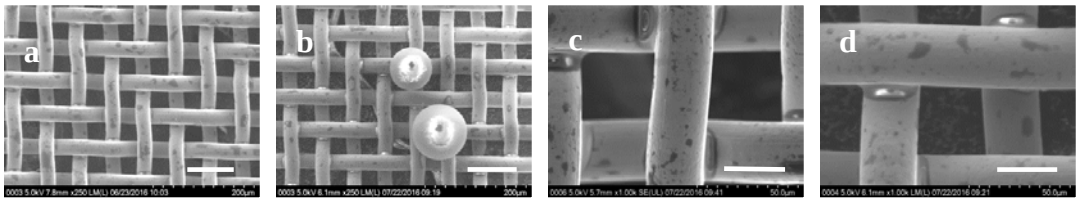

Figure 4.12: SEM images of the coated mesh 400 before (a,c) and after (b,d) sand test (low and high magnification). Scale bars represent 100 μm in (a), (b) and 30 μm in (c), (d).

SEM images were taken on coated meshes before and after sand test to determine if significant structural changes were caused by the sand test (Figure 4.12). No visual damage was found on the mesh fibers after sand exposure. Similarly, uncoated mesh remained essentially the same after sand test as assessed by SEM images (not shown). Figure 4.12b shows that sand particles blocked some pores on the mesh, which may affect the water flux in the oil-water separation. Thus the sand tested mesh was used to separate a layered oil-water mixture without further cleaning. Excellent separation performance was retained with separation efficiency higher than 99.99% (confirmed with UV-vis), while the water recovery rate and flux dropped slightly to 87.9% and 5.38×10^4 $L \cdot m^{-2} \cdot h^{-1}$ respectively. The oil layer remained on the mesh without leakage during 24 hr of observation. Other aspects of mechanical durability of the surface were also tested with tape peeling and rotary abrasion tests (see “Mechanical durability tests” in section 4.2 for details of setup). After these tests, mesh 400 with MTMS coating retains its wetting properties (contact angles of water and motor oil display less than 5° difference

from untested mesh) and oil-water separation effectiveness (separation efficiency remains 99.99%, water flux changes by less than 0.5%), thus demonstrating good coating adhesion and resistance to external abrasion.

4.4 Conclusions

A quick and simple way to fabricate hydrophilic-oleophobic stainless steel meshes for oil-water separation using non-fluorinated coating materials has been developed. The coating materials were prepared by mixing methyltrimethoxy silane (MTMS) with 0.1 M hydrochloric acid at a ratio of 4:1, followed by sonication in an ice bath for 5 min. Meshes were then immersed in the mixture for 2 min and dried in air for 1 hr. The mesh performance depends strongly on dimensions: mesh 400 with an inter-fiber gap of 38 μm and fiber diameter of 26 μm showed underwater superoleophobicity and the best performance in separating oil-water mixtures. The coated mesh allows water fluxes as high as 7.16×10^4 $L \cdot m^{-2} \cdot h^{-1}$, with water recovery up to 91.1 % and separation efficiency higher than 99.9 % solely driven by gravity. The unique combination of hydrophilicity and underwater oleophobicity was achieved on the mesh surfaces by introducing both silanol and methyl groups through controlled hydrolysis and condensation of MTMS. As a result, the system does not have the fouling problems usually encountered by hydrophobic-oleophilic materials. This mesh filter can be easily fabricated onsite, maintains excellent mechanical strength, and exhibits high water throughput. Compared with existing oil-water separation units, this filter system is more environmentally friendly and suitable for drinking water treatment, since the coating does not contain fluorine. The result of dynamic sand impact tests shows that the coated surface is resilient towards mechanical impact; even with the presence of residual attached sand particles,

the mesh still functioned efficiently. Thus, MTMS-coated mesh filters hold great potential for applications such as oil spill cleanup, where the presence of abrasive particulates is inevitable. In addition, the ability to separate oil droplets larger than the mesh pore size from oil-water emulsions suggests that it can also be incorporated into current large scale oil-water separation units as a cheap but effective pretreatment step.

CHAPTER 5

MECHANICAL DURABILITY OF LIQUID REPELLENT COATINGS

This chapter has been reproduced for submission in *Surface and Coatings Technology* by L. Jiang *et al.*

5.1 Introduction

Surface modification to achieve specific wetting properties on various substrates has been studied intensively since the discovery of the "lotus effect". [203] In most commercially relevant applications, these functionalized surfaces will be exposed to an array of environmental impacts, including mechanical wear. Therefore, mechanical wear resistance (mechanical durability) is critically important for the prevention of surface property degradation during long-term use. Mechanical durability testing of liquid repellent surfaces is often very limited; most surface modification studies invoke one type of test for a specific coating material and substrate. A well-defined suite of mechanical tests for a more comprehensive evaluation of surface mechanical robustness on different substrates and for different coating materials has not been reported. [96,100,204-207] A few review articles have summarized the state of the art for design of durable liquid repellent surfaces [208,209] and/or commented on the mechanical durability among different kinds of liquid repellent surfaces tested under specific conditions. [21,95,96]. Zhi *et al.* tried to compare the mechanical durability of superhydrophobic surfaces fabricated with various surface modification techniques, but only a sandpaper abrasion

test was used to evaluate the durability of the surfaces. [210] Malavasi's group has attempted to develop a protocol including water immersion, exposure to various chemical environments (acid, alkali, alcohol and iconic solutions), mechanical erosion, heating and UV exposure for evaluating surface durability while only one specific superhydrophobic surface developed in-house was tested. [211]

Direct comparison of standard mechanical durability tests on different coating types are essential to better understand advantages and limitations of each durability test and surface modification method; ultimately this allows design and evaluation of functional surfaces for specific applications. It has been recognized that the loss of durability is generally caused by material removal, which results in changes in chemistry and/or morphology; the durability is usually evaluated by contact angle changes. [94,212,213]

In this chapter, both paper and glass slides have been used to represent flexible and structured, as well as rigid and smooth substrates, respectively. Liquid repellent surfaces were generated on both substrates via several approaches that result in notably different coating properties, in particular thickness; in addition to methods developed in our own research group, a commercial coating material was tested as well. These coated surfaces are compared under tape peeling, dynamic impact, pressing, rotary abrasion and bending tests. For each of these wear tests, the performance of the coatings is evaluated with contact angle measurements and analyzed with SEM, FTIR and XPS. The results provide improved understanding of the unique mechanical properties of liquid repellent surfaces generated by several different methods, point out future directions for improving

their mechanical durability, and offer a reference base for selection of coating material and testing method for specific applications.

5.2 Experimental Methods

Paper Formation

Southern hardwood kraft fibers (Alabama River mill, Georgia-Pacific Cellulose Co.) were used to prepare paper substrates. The dry fiber sheets were soaked in deionized water overnight and then refined in a PFI mill for 6,000 revolutions according to TAPPI standardized method T 248 sp-08. Paper sheets were formed following TAPPI standardized method T 205 sp-02 using treated pulp.

Glass Slides Preparation

Before coating processes, VWR micro slides (frosted, selected and precleaned, 25× 75 mm, 1.0 mm thick, Cat. No. 48382-173) were cleaned with acetone, methanol and isopropanol and dried with a nitrogen stream.

Plasma Etching and Plasma Enhanced Chemical Vapor Deposition (PFE)

Paper samples were cut into 35 mm × 15 mm strips and placed in a 6 inch electrode parallel plate (13.56 MHz) plasma reactor and etched for various times. During etching, oxygen was introduced into the reactor at 75 standard cubic centimeters per minute (SCCM) under an equilibrium pressure of 0.5 Torr. The etching process was conducted at 110 ℃ using a power of 120 W for 30 min. For plasma enhanced chemical deposition, the fluoropolymer coating was deposited on the paper surface using a plasma composed of 75 SCCM Ar and 20 SCCM pentafluoroethane (PFE, Praxair) at an

operating pressure of 1.0 Torr for 30 seconds. Further details for of the reactor configuration can be found in previous publications. [48,49]

Dip Coating of Fluorosilane (FDTCS)

The paper coating solution was prepared by mixing 10µl of (heptadecafluoro-1,1,2,2-tetrahydrodecyl)trichlorosilane (FDTCS) (Gelest, Inc.) with 10 ml toluene (Alfa Aesar, anhydrous, 99.8%). The paper substrate was then dipped into this solution for 2 min. After immersion, the substrate was removed from the solution and dried at ambient conditions overnight.

Vapor Deposition of Fluorosilane (FDTCS-VD)

50 µl of FDTCS (heptadecafluoro-1,1,2,2-tetrahydrodecyl)trichlorosilane, Gelest Inc.) mixed with 150 µl toluene was placed in a 4 ml glass vial. The open vial along with the substrate, was placed within a 20 ml glass bottle. The bottle was uncapped and covered with an inverted beaker. During heating (100 ℃), the gap between the beaker and the bottle allowed fluorosilane vapor to be released as the oven was evacuated (88 kPa). The silanization process was performed in a vacuum oven for 15 min. Detailed information about the setup can be found in our previous publication. [214]

Dip Coating of Non-fluorinated Chemical (MTMS)

Methyltrimethoxysilane (MTMS, Sigma-Aldrich, deposition grade, ≥ 98%) was mixed with 0.1 M hydrochloric acid (HCl, Fisher Chemicals, 37.3%) in a 4:1 v/v ratio. This mixture was then sonicated in an ice bath for 3 hr to induce hydrolysis. Sonication was performed with an ultrasonic cleaner (Fisher Scientific, model FS20) at 70 W and 42

kHz. After 3 hr of sonication, paper samples were immersed in the mixture for 2 min and excess fluid on the substrate was removed by pressing the substrate with tissue paper. Finally, the paper was dried at ambient conditions overnight. Experimental details are discussed in a previous publication. [51]

Commercial Product Coating (Neverwet®)

Rust-Oleum® Neverwet® water repellant spray coating was purchased and applied to paper handsheets following the product application directions. The spray can was positioned 8-12” from the surface and excess liquid was removed with tissue paper. The substrate was dried at ambient conditions for 24 hr before testing.

Mechanical Durability Tests

After each mechanical durability test, samples were equilibrated under ambient conditions for 24 hr before contact angle measurements.

Tape Peeling (TP)

3M Scotch tape was applied on the paper or glass surface and pressed firmly to ensure no visual air entrapment between the tape and the substrate surface. The tape was then peeled from one end of paper; the peeling process was repeated 10 times.

Dynamic Impact (DI)

The substrate under investigation was tilted 45° and exposed to 20 g of glass beads (abrasive blasting media, mesh size 60-120, McMaster-Carr) that flowed out of a plastic funnel held 40 cm above the substrate for approximately 30 seconds.

Weight Pressing (WP)

The substrate was placed under a 470 g weight, which corresponds to a pressure of 8.8 kPa, for 1 hr.

Rotary Abrasion (RA)

The substrate was attached with tape to the wall of a clean glass jar (9 cm in diameter, 10 cm tall) containing 60 g of glass beads (abrasive blasting media, mesh size 60-120, McMaster-Carr) and the jar rotated at 1 rpm. The substrate was removed after 1 hr of rotation.

Bending (B)

The paper substrates were bent around three glass tubes with diameter of 5 mm, 7 mm and 14.5 mm (B5, B7, B14.5) respectively; the long edge of the paper samples was kept parallel to the tube axis. After 24 hr in those positions, the substrates were removed and allowed to equilibrate for 24 hr prior to contact angle measurements. During contact angle measurements, the curved samples were flattened on the measuring platform using tape; the side facing away from the tube when wrapped was measured.

Contact Angle and Roll Off Angle Measurements

All static contact angle (CA) measurements were performed by placing an 8 μl droplet of selected fluid (DI water, ethylene glycol (Sigma-Aldrich, anhydrous, 99.8%), diiodomethane (Sigma-Aldrich Co., 99%), motor oil (SAE 10W-30, MotoTech), n-hexadecane (Sigma-Aldrich Co., 99%)) onto the paper or glass slides. Images were recorded and analyzed by a rame-hart goniometer (model 290). For roll-off angle

measurements, the solid surface was gradually inclined from 0° to 90° using the tilting plate method to establish the tilt angle for roll-off.

SEM Imaging

Scanning electron microscopy (SEM) was performed on paper and glass substrates that were sputter coated with Ag/Pd to mitigate charging effects during imaging. Images were taken with a Hitachi SU8230 cold field-emission SEM (Hitachi High-Technologies Co., Japan).

FTIR Analysis

FTIR analysis was conducted using a Nicolet iS-50 FT-IR spectrometer (Thermo Scientific, Inc.) in ATR mode. The data collection was carried out by obtaining 64 scans at 4 cm^{-1} resolution across the range of 4000 ~ 700 cm^{-1} using Omnic software.

X-ray Photoelectron Spectroscopy

The elemental composition and chemical bonding information of the substrates were determined with a Thermo K-Alpha XPS (Thermo Fisher Scientific, West Palm Beach, FL) at a pressure below 10^{-7} Pa. Thermo Advantage 5.934 software was used to curve fit and deconvolute the high resolution C1s spectra.

Coating Thickness Measurements on Si Wafers

P type 100mm silicon wafers (Wafer World Inc.) were washed with acetone, methanol and isopropanol, and subsequently dried with a nitrogen gas stream. Then the silicon was coated with PFE following the procedure provided in section 2.3. The coating

thickness was measured with J.A. Woollam M-2000 variable angle spectroscopic ellipsometer.

5.3 Results and Discussion

Mechanical Robustness of Coatings on Flat, Inflexible Substrate

Before exploring the coating robustness on complex, structured substrates such as paper, all coatings were applied to glass slides and subjected to various durability tests in order to evaluate their behavior on a flat surface. Detailed information about the coating thickness is presented in Section 3.2 (see Table 1). Figure 1 shows the contact angle data for various liquids on coated glass surfaces before and after different mechanical durability tests.

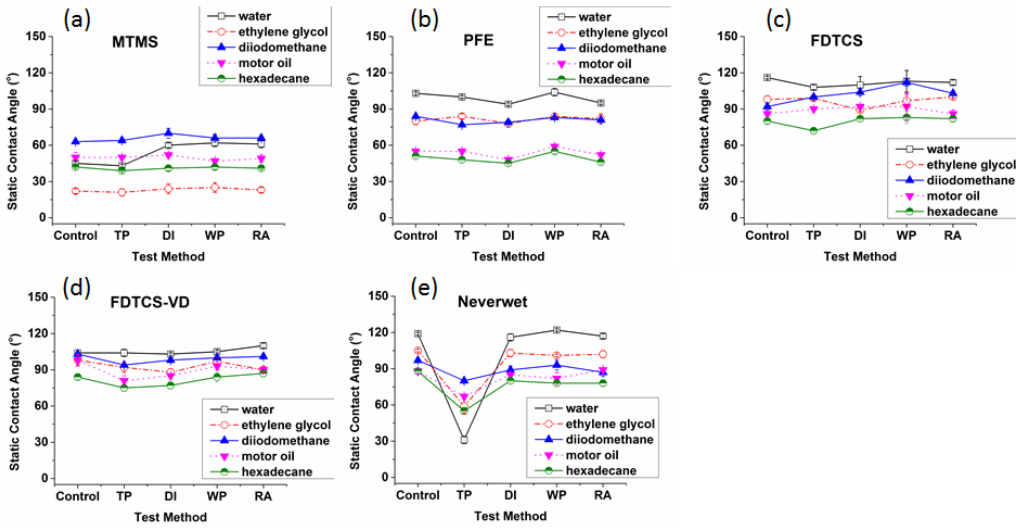

Figure 5.1: Liquid static contact angle data on glass slides coated with (a) MTMS, (b) PFE, (c) FDTCS (d) FDTCS-VD and (e) Neverwet® after various mechanical tests (TP-tape peeling, DI-dynamic impact, WP-weight pressing and RA-rotary abrasion).

From Figure 5.1 we can see that all of our laboratory coatings (Figure 5.1a-d) show excellent resistance towards all mechanical tests when applied to glass slides; no significant changes in wetting properties could be detected. FDTCS grafted onto a flat glass surface through either dip coating or vapor deposition shows similar wetting properties and resistance towards various mechanical durability tests, which indicates similar surface chemistry and coating adhesion on a flat surface. For the glass slide coated with the commercial coating Neverwet®, a large drop in contact angles was observed after the tape peeling test which indicates poor coating adhesion to the surface. FTIR spectra confirm that the coating is removed during this process, since the characteristic peaks of the Neverwet® coating were no longer detected after tape peeling: the FTIR spectrum was essentially the same as that for uncoated glass slides (see Figure 5.2).

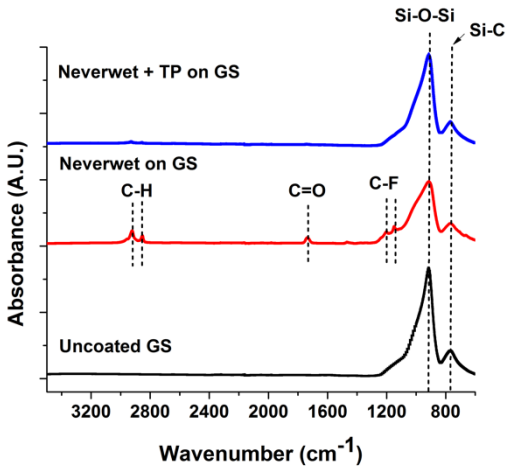

Figure 5.2: ATR-FTIR of uncoated glass slides, and for glass slides coated with Neverwet® before and after tape peeling (TP).

Compared with tape peeling, other mechanical tests such as dynamic impact, weight press and rotary abrasion primarily affect the surface structure and are less severe

tests of coating adhesion. This explains why the Neverwet® coating retains robustness on flat and non-flexible surfaces such as glass slides when subjected to these other tests.

Mechanical Robustness of Coatings on Flexible, Fibrous Substrate

To study the mechanical durability of structured materials, specifically those containing fibers, paper was used as the model substrate. The same coating materials were used as in the experiments with glass. Accurate measurement of coating thickness on heterogeneous surfaces such as paper is challenging. However, since mechanical durability is expected to be affected by coating thickness, a thickness estimate for each coating method is highly relevant; our best estimates are provided in Table 5.1.

Table 5.1: Estimate of coating thicknesses and measured loading on paper substrates

Coating type	Coating impact	Thickness estimate	Loading on paper (wt. %)
MTMS	bulk	500 nm ~ 1 µm	19.3
PFE	surface	~100 nm	< 1.0
FDTCS	bulk	100 ~ 200 nm	< 1.0
FDTCS-VD	surface	< 5 nm	< 1.0
Neverwet®	surface	200 ~ 300 nm	1.9

For the FDTCS-VD, XPS analysis, which has a detection depth of roughly 5 nm, suggests that the vapor-deposited coating is less than 5 nm thick on a paper surface, since the underlying cellulose is still detected; more accurate ellipsometry measurements of FDTCS-VP on a silicon wafer yield a 1 - 2 nm coating thickness. [214] Estimates of the

thicker coating layers are based on the surface morphology changes that were observed via SEM imaging at high magnification (see Figure 5.3), as well as more accurate knowledge about the coating processes on model substrates. For example, PFE coating of a silicon wafer under the same conditions results in a ~100 nm thick coating layer according to ellipsometry measurement, which agrees with the structural changes on coated paper as observed via SEM. Figure 5.3b shows that MTMS gives a very thick coating on paper which blankets the etched structure on the surface, thus significantly reducing the nanoscale roughness of paper (compare 5.3a and b). However, the coating is not thick enough to cause dramatic changes of fiber dimensions (compare the insets in Figure 5.3).

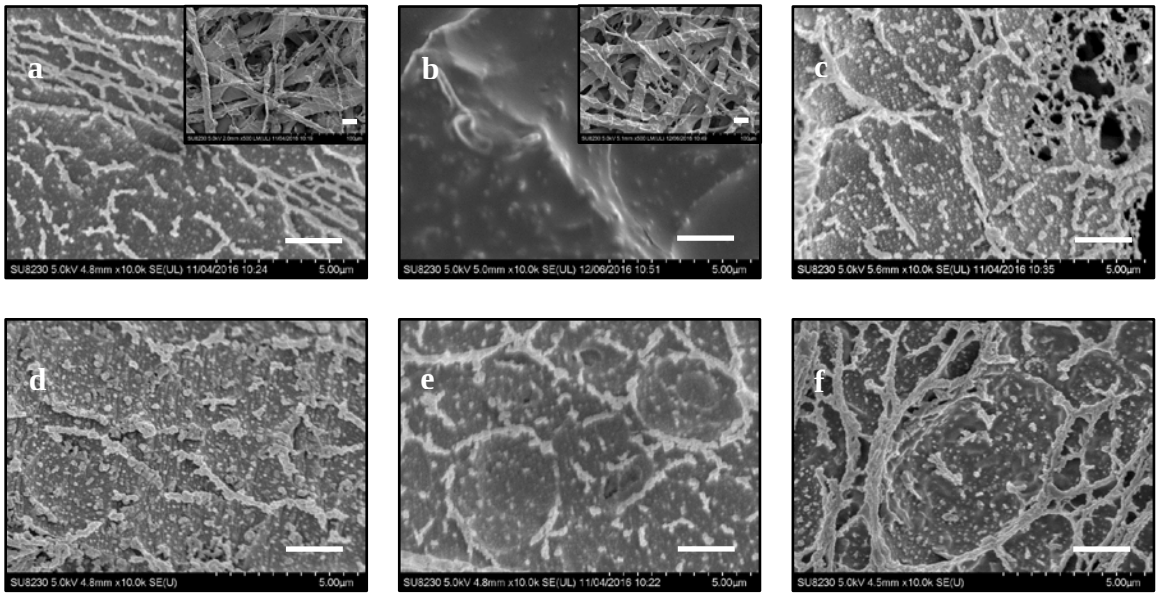

Figure 5.3: SEM images of (a) uncoated paper and paper coated with (b) MTMS, (c) PFE, (d) FDTCS, (e) FDTCS-VD and (f) Neverwet. The scale bars represent 2 µm. Insets: High magnification SEM images of (a) uncoated paper and (b) paper coated with MTMS. The scale bars represent 20 µm.

Finally, the loading of coatings on paper was also determined by measuring the weight change of paper before and after the coating process after conditioning the substrates for two days according to TAPPI standardized method T 402; these data correspond well with the magnitude of estimated thicknesses. It has to be noted here that due to the differences of the coating conditions, coatings are loaded on the sample differently (see "coating impact" in Table 5.1). For example, dip coating (including MTMS and FDTCS) will load the bulk part of the sample with the coating material, while vapor deposition and spray coating limit the modification to the top surface of the sample.

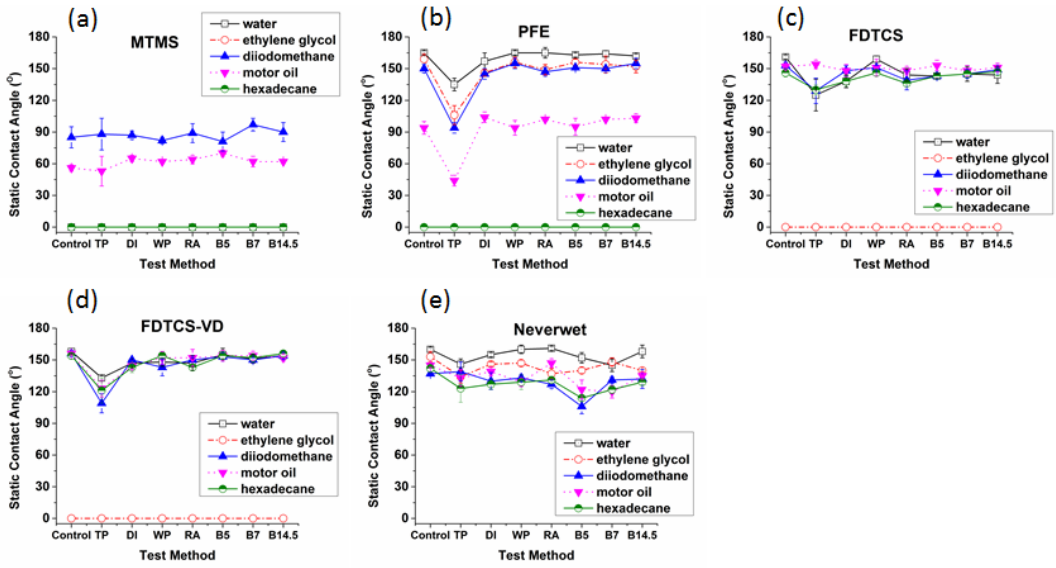

Figure 5.4: Liquid static contact angle data on paper coated with (a) MTMS, (b) PFE, (c) FDTCS, (d) FDTCS-VD and (e) Neverwet® after various mechanical tests (TP-tape peeling, DI-dynamic impact, WP-weight pressing, RA-rotary abrasion, B5, B7 and B14.5-bending around glass tubes with diameter of 5 mm, 7 mm or 14.5 mm).

Figure 5.4 shows contact angles for different test liquids on coated paper after various mechanical durability tests. Samples with testing liquid displaying zero contact angle means the liquid either completely absorbed into the sample or has a contact angle less than 10° which is the detection limit of the measurement equipment. Paper was etched with an oxygen plasma prior to the coating process to impart the appropriate roughness and thereby improve liquid repellency. Such procedures also allow the robustness of hierarchical structures typically involved in anti-wetting studies to be investigated.

Coating Adhesion

It is relatively straightforward to evaluate coating adhesion on a flat, nonflexible surface such as a glass slide; determining coating adhesion on fibrous materials using changes in wetting properties is difficult at best. Adhesion strength between adhesive and coating, between coating and fibers, and fiber-fiber bonding strength can all determine the final wetting properties of substrates after tape peeling (see Figure 5.5). Strong adhesion between tape adhesive and coating and between coating and fibers can result in fiber breakage and/or detachment upon tape peeling, which can lead to reduced liquid repellency or even total loss thereof. Strong adhesive bonding to the coating combined with weak coating adhesion to the fibers, leads to peeling of the coating material from the fibers and likely also to loss of liquid repellency. If both the fiber-fiber bonding and coating adhesion to the fiber are stronger than the adhesion between the adhesive layer and coating, no significant drop in contact angle should be observed after tape peeling.

Figure 5.5: Schematic representation of the composite interface of the tape adhesive layer on coated fiber surfaces, highlighting the fiber-fiber, fiber-coating and coating-adhesion interfaces, all of which can be disrupted in tape peeling experiments.

Coatings with low surface energies will have weaker interaction with the adhesive layer since the adhesive does not spread easily on such surfaces. This is demonstrated by the tape peeling results on paper surfaces with different coating materials -and thus surface energies- (see insets in Figures 5.6b and 5.6g). Paper without any coating has a high surface energy, which leads to strong adhesion with the adhesive layer, so that the peeling test breaks the weakest fiber-fiber bonds and causes delamination of the paper fiber structure after only 5 tape peelings (see inset in Figure 5.6b). In contrast, paper coated with low surface energy materials like Neverwet® remain intact even after 10 peeling cycles (see inset in Figure 5.6g). With relatively high surface energy (relative surface energy: MTMS> PFE> FDTCS ≅ Neverwet®), MTMS and PFE coatings have stronger adhesion with the adhesive layer compared to that of the other two coatings. Figures 5.6c and 5.6d show SEM images of MTMS and PFE coated paper after tape peeling tests where the top fiber layers have been peeled off, which indicates good coating adhesion to fibers, even though a large standard deviation (Figure 5.4a) and/or significant drop (Figure 5.4b) in liquid contact angles were observed after tape peeling.

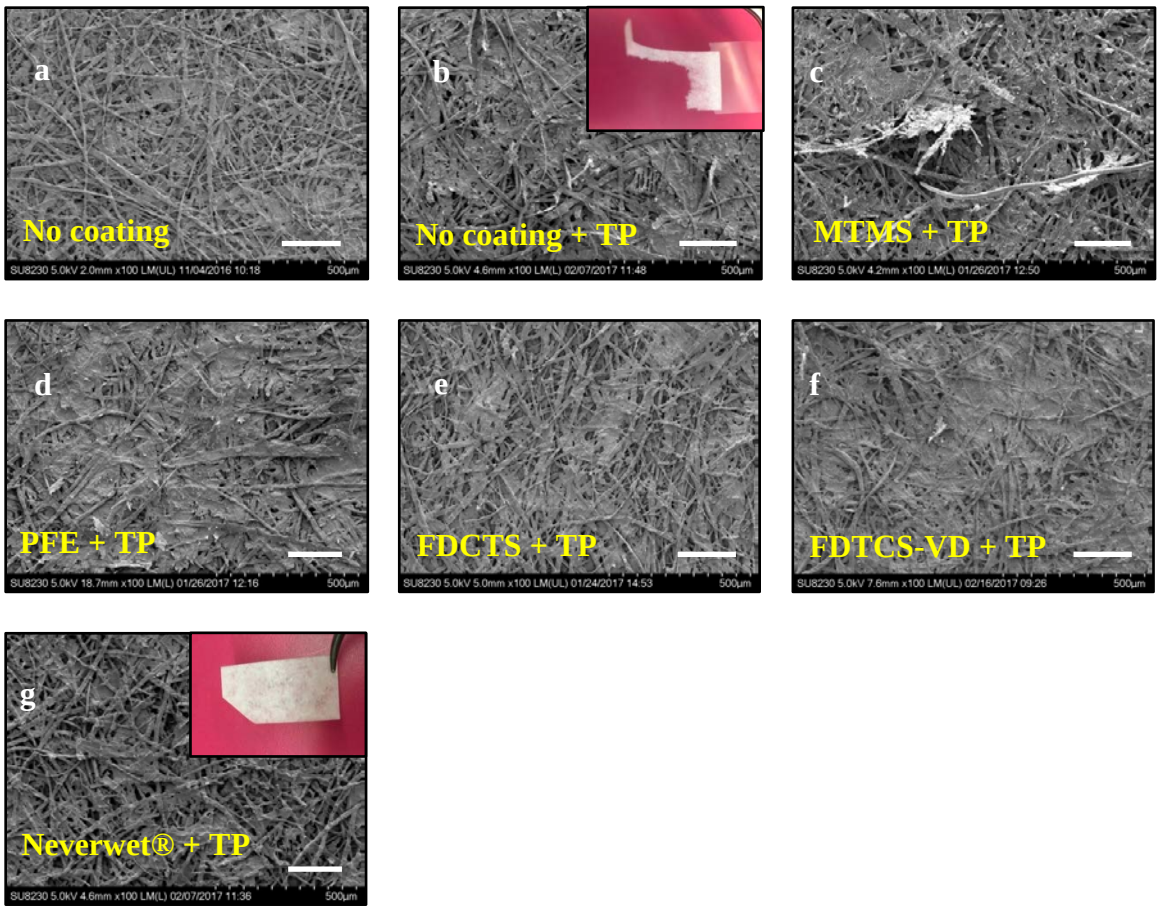

Figure 5.6: SEM images of 30 min etched paper (a) before and (b) after tape peeling test, and 30 min etch paper coated with (c) MTMS, (d) PFE, (e) FDTCS, (f) FDTCS-VD and (g) Neverwet® after tape peeling test. The scale bars represent 200 μm. Inset b: 30 min etched paper after 5 tape peeling cycles; inset g: 30 min etched and Neverwet®-coated paper after 10 tape peeling cycles.

For FDTCS and Neverwet® coated samples, a relatively intact paper surface (Figure 5.6e and 5.6g) and minor drop in liquid contact angles (Figure 5.4c and 5.4e) indicate that both the coating adhesion to the fibers and the fiber-fiber bonding strength exceed the adhesion between the tape adhesive layer and coating. Furthermore, XPS analysis did not reveal significant changes in surface chemistry for FDTCS and

Neverwet® coated surfaces after tape peeling, which provides further evidence that the coating remains intact on the surface (see Figure 5.7).

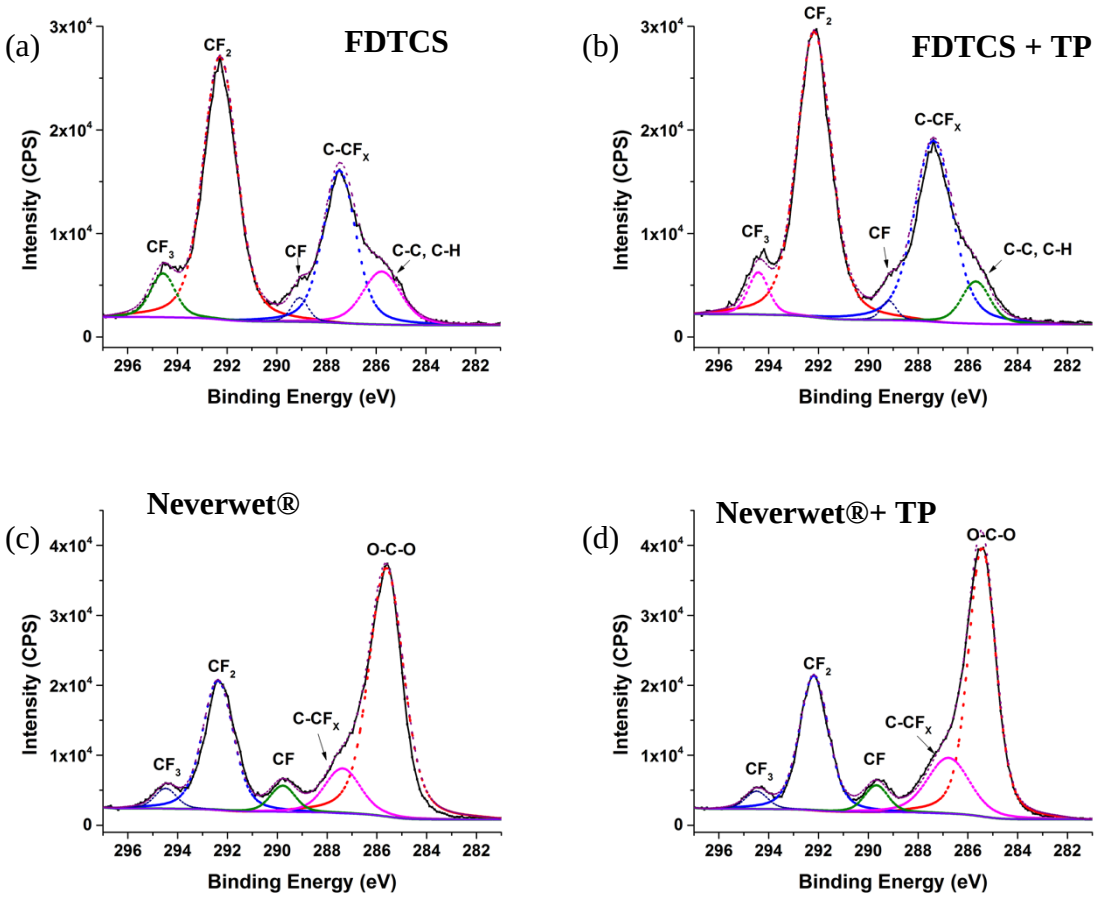

Figure 5.7: Deconvolution of C1s XPS spectra of FDTCS coated paper (a) before and (b) after tape peeling and Neverwet® coated paper surface (c) before and (d) after tape peeling.

However, considering the heterogeneity of paper surfaces, individual fibers that are weakly bonded to others can be peeled off readily. The resultant disturbance of surface structure could explain the slight contact angle drop on these two samples.

Compared with the Neverwet® coating on glass slides, the coating adhered more strongly to paper, probably due to more abundant bonding groups on the fiber surface. In addition, surfaces with texture (e.g., paper) may have lower bonding strength with the tape adhesive layer since the porous structure inhibits full contact between the adhesive layer and the substrate.

FDTCS and FDTCS-VD have very different processing conditions and resultant coating thicknesses, but the grafting chemistry between coating and surface groups is expected to be the same, which is supported by the highly consistent liquid contact angle data between both methods on both glass and paper substrates (compare Figures 5.1c and 5.1d and Figures 5.4c and 5.4d). In contrast to vapor deposition, most of the tiny fibrils weakly bonded to the fiber have been lost during the dip and lifting process of FDCTS dip coating (compare Figure 5.8a and 5.8b). However, the weakly bonded fibrils left on the FDTCS-VD sample are more likely to serve as a breaking point of the fiber network during tape peeling. SEM imaging results show that peeling off of the fiber material is more widely found on the FDTCS-VD sample than the FDTCS sample (compare Figure 5.6f, 5.8c with 5.6e, 5.8d). A greater reduction of water and oil contact angles after tape peeling on FDTCS-VD than that of FDTCS sample is likely caused by these local defects in the fiber network (Figure 5.4c and 5.4d).

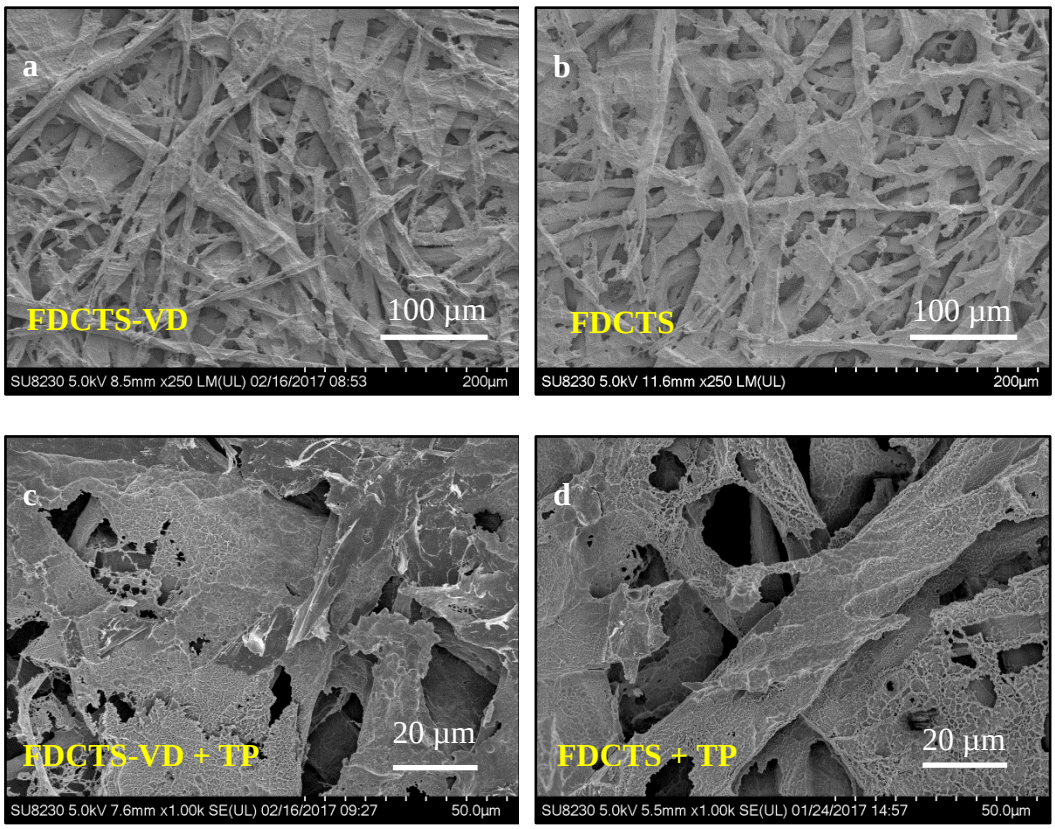

Figure 5.8: SEM images of paper coated with (a) FDTCS-VD and (b) FDTCS and the high-resolution images of their paper surface after tape peeling test respectively (c,d).

Although the anti-wetting properties of the coatings investigated in this study are affected quite differently by tape peeling, all of them adhere well to the fibers according to the analysis described in the previous discussion. However, our studies indicate that tape peeling is not an appropriate adhesion test for comparing coatings on different substrates because adhesion force between the coating surface and the tape adhesive layer could vary significantly and cannot be controlled. Also, for porous substrates, no direct correlation exists between performance failure and coating adhesion force, since the contact area with the tape adhesive layer is extraordinarily complex and thus the test

method is qualitative at best. However, as a relatively simple and inexpensive test, tape peeling can provide an indication of coating adhesion strength on a flat surface.

Morphology Changes upon Solid Particle Impact

The resistance to dynamic impact and rotary abrasion appear to be quite similar among all coated samples (Figure 5.4), irrespective of their coating thickness and original wetting properties. This phenomenon can be explained by the fact that the wetting properties of paper, with good coating adhesion, will primarily be affected by the fiber structure change caused by these mechanical tests; the performance of the coated surface should also depend heavily on the mechanical robustness of the substrate itself. Figure 5.9 shows the changes of paper morphology and the fiber structure on Neverwet® and PFE coated paper after rotary abrasion.

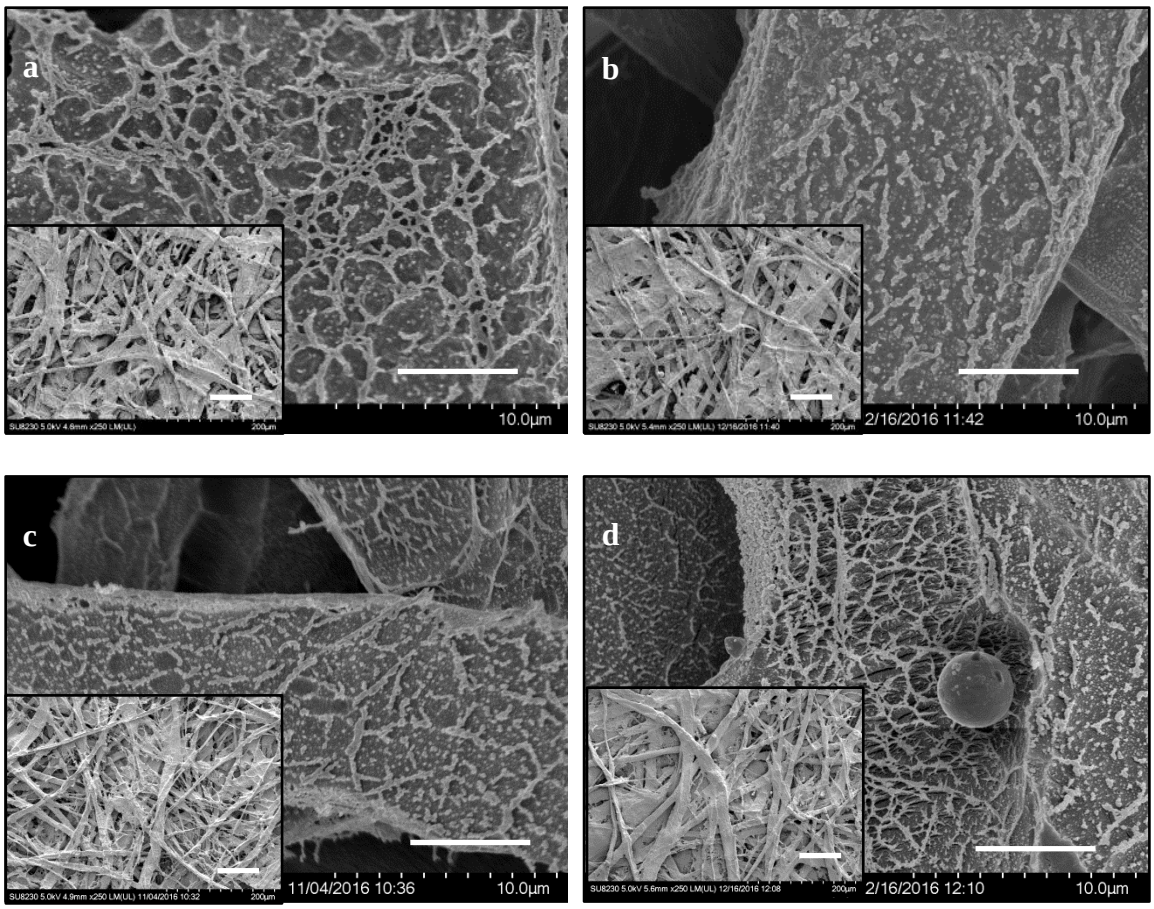

Figure 5.9: SEM images of paper coated with Neverwet® (a) before and (b) after rotary abrasion test and PFE (c) before and (d) after rotary abrasion test. The scale bars represent 5 μm. Inset: Low-resolution SEM images of respective paper surface where scale bars represent 80 μm.

According to Figures 5.9a and 5.9b, there is no significant destruction of the underlying fiber network by particle impingement during rotary abrasion. Some nanoscale roughness has been lost on the Neverwet® sample, however, due to particle abrasion on the surface, which causes a slight fluctuation in contact angle data. Similar morphology changes were also found on other coated paper surfaces after dynamic impact and rotary abrasion tests. The hierarchical structure of the paper was generated via plasma etching, which leads to robust surface structures; nevertheless, the inherent

mechanical softness of cellulose leads to structure modification after the harsh solid impact during abrasion. In order to assess the durability of liquid repellent coatings that rely on the incorporation of nanoparticles in polymer materials or electronspun nanofibers, solid impact tests are strongly recommended.

Without the dip and lifting of the sample in the coating solution, PFE samples also retained tiny fibrils on the paper surface (see the inset of Figure 5.9c) as did the FDTCS-VD samples discussed earlier. A significant fraction of the weakly bonded fibrils was lost after rotary abrasion, which indicates the strong abrasion force of the testing process (see inset of Figure 5.9d). Additionally, small sand particles were found on the fiber surface after both dynamic impact and rotary abrasion move (Figure 5.9d). Sand particle adhesion and the resultant structural changes are widely encountered in outdoor applications. Coatings such as MTMS, with higher surface energy, exhibit more particle pickup than coatings with lower surface (FDTCS and Neverwet®). However, none of the surfaces display significant changes in wetting properties after these two tests, in spite of the presence of residual sand particles (see Figure 5.4).

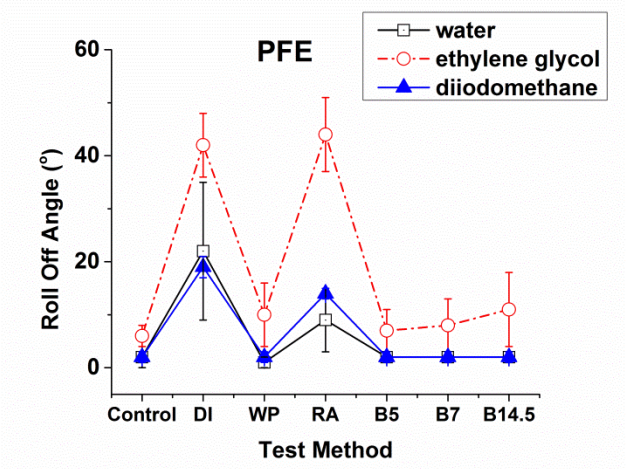

Figure 5.10: Roll off angle of various testing liquids on paper coated with PFE after different durability tests (DI-dynamic impact, WP-weight pressing, RA-rotary abrasion, B5, B7 and B14.5-bending around glass tubes with diameter of 5 mm, 7 mm or 14.5 mm).

In order to investigate more intricate changes that may be induced by these residual particles, roll-off angles, which are very sensitive to heterogeneities created by changes in both surface chemistry and morphology, were measured for various testing liquids on PFE coated paper before and after durability tests; the data are shown in Figure 5.10. It should be noted that among the five testing liquids, only water, ethylene glycol and diidomethane roll off the PFE coated paper. Furthermore, all testing liquids become sticky –*i.e.*, droplets do not not roll off the surface even at 90° tilt- after the tape peeling test, the results of which are therefore not included here. We can see that, in addition to tape peeling, dynamic impact and rotary abrasion induced the largest changes in roll off behavior. [143,144] Similar trends were also observed on Neverwet® and FDTCS-VD coated paper. These observations can be explained by the heterogenity of the surface that resulted from the residual sand particles. Depending upon the application, this change

could affect the performance of the liquid repellent surface if low liquid adhesion is critical. Compared with other popular methods for testing surface resistance towards abrasion and dynamic impact, our methods also enable the evaluation of dirt/paticle pickup, which is inevitable in commercial applications. In contrast, applying uniform pressing on the substrates does not cause local defects that could ultimately change wetting performance (see Figure 5.4 and 5.10).

Durability towards Bending Tests

Coating robustness towards bending is an important characteristic for substrates that are folded or bent during applications, such as many packaging materials. In general, it is expected that thin, inherently pliable coating materials with strong adhesion to the underlying substrates will perform best, while thick or brittle coatings are more susceptible to failure during bending.

According to the coating thickness and loading data provided in Table 5.1, MTMS and Neverwet® coatings both result in high loading of coating material, and these substrates indeed display slightly higher fluctuation of contact angle changes upon bending (see Figures 5.4a and 5.4e). Even untested paper with a relatively thick MTMS coating displays cracks that are created during fabrication (see Figure 5.3b). The number and length of these cracks increase after bending tests. Since the nanoscale roughness is nearly covered by the thick coating, and the coating adhesion is good, defects on the fiber are probably the main reason for the observed contact angle variation after bending tests.

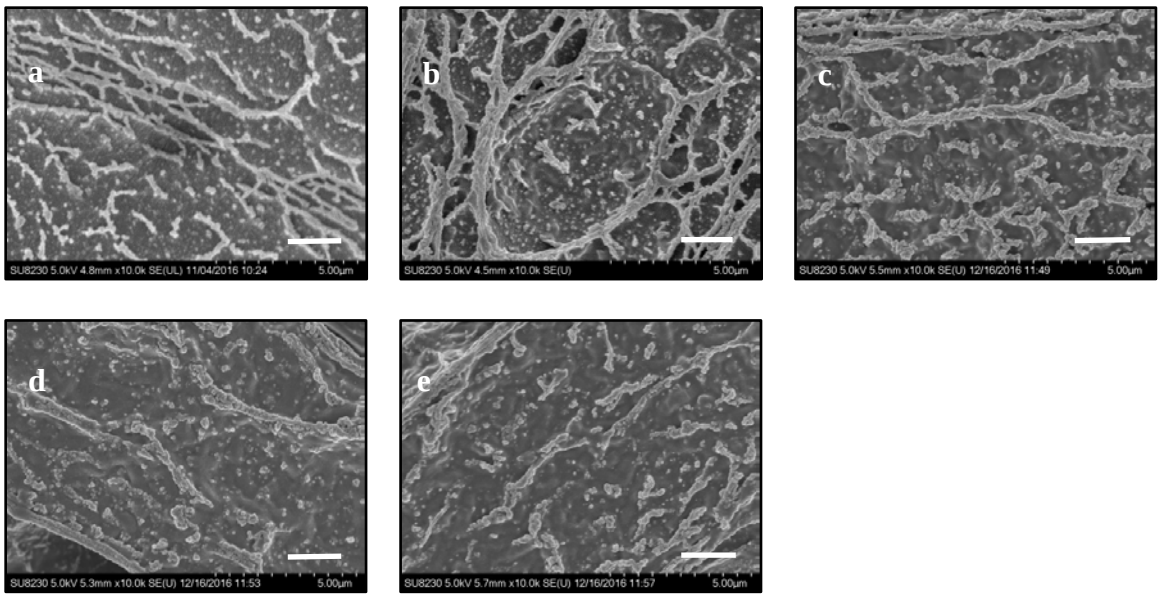

Figure 5.11: SEM images of (a) uncoated paper and Neverwet® coated paper (b) before and after bending tests on tubes with diameters (c) 5mm, (d) 7mm and (e) 14.5mm. Scale bars represent 2 μm.

The differences between Figures 5.11a and 5.11b relate to the more connected morphology on the fiber surface introduced by a Neverwet® coating. The coating process gives a sufficiently thick surface coating that it both modifies the surface chemistry and also changes surface morphology. However, the structure added shows little resistance to mechanical stresses. Figures 5.11c-e shows the changes on Neverwet® coated paper after bending the paper around glass tubes with different diameters. Compared with the coated paper before testing (Figure 5.11b), the sub-micrometer structure was clearly altered after bending. The weak linkages between the surface asperities have been significantly destroyed by surface stretching during the bending process as shown in Figures 5.11c-e. The fluctuations in contact angle upon bending are consistent with this structure change on the fiber surface.

For PFE, FDTCS and FDTCS-VD coatings, the coating is estimated to be thinner than 200 nm, with material loadings that are below our detection limit (1%). Figures 5.4b-d indicate that their anti-wetting properties before and after bending tests are essentially unchanged; furthermore, the thinnest coating FDTCS-VD (< 5 nm) displayed the most consistent wetting properties. Good coating adhesion and flexibility are probably the reasons why no notable surface changes are detected before and after bending tests. Thus, coating material loading is not only critical for economic reasons, but also affects the robustness of the functionalized surface upon bending.

5.4 Conclusions and General Recommendations

Direct comparison of mechanical durability of chemically and physically different liquid repellent surfaces using a set of comprehensive evaluation techniques has been reported for the first time. The durability tests employed are relatively simple, inexpensive to implement, and generally well-known. However, in essentially all previous studies, only one or a few of these methods has been invoked to determine certain aspects of surface robustness for the specific liquid repellent surfaces that were fabricated by those researchers. This study is the first attempt to directly compare the durability of a wide variety of modified liquid repellent coatings with the same set of comprehensive evaluation criteria and thus offer insight into the critical design parameters involved in the fabrication of durable liquid repellent surfaces. Coating adhesion, resistance to dynamic impact and tangential abrasion, robustness upon pressing and bending are critical aspects that indicate long-term stability of most surfaces during use in commercial applications. In this study, tape peeling, solid particle dynamic impact, rotary abrasion, weight pressing, and bending tests were used to examine these

properties. As a widely used method for testing coating adhesion, tape peeling is often not a suitable technique for quantitative comparison of coating adhesion, especially on porous surfaces, and thus the results must be interpreted cautiously. Dynamic impact and abrasion tests target both the coating adhesion and the durability of artificial hierarchical structures that are commonly present on highly liquid repellency surfaces; these tests should thus be included as standard tests. For flexible materials and applications where bending or folding are needed, thinner coating materials prove to be more durable upon bending. Ultimately, we hope that our findings lead to better communication among researchers working on durable anti-wetting surfaces and assist industrial professionals in optimizing coating processes and thereby improving long-term performance of the products.

CHAPTER 6

CONCLUSIONS AND FUTURE WORK

Surfaces with high repellency towards a wide range of oils and water have only been reported recently, despite the fact that extensive applications exist for such surfaces. However, technology transfer from the laboratory to industrial applications remains hindered by factors such as low process scalability, poor material mechanical robustness, and limited resistance to environmental hazards such as rain and particle impingement. This thesis focuses on investigating methods of wetting control on fiber-based materials, and specifically on finding novel ways to balance the anti-wetting performance and economic benefits of such materials.

As a biodegradable, inexpensive and universally accessible material, paper is used widely in many applications, including packaging, office supplies and household products. However, the hydrophilic and oleophilic nature of paper often limits its use in applications that involve direct contact with liquids. In Chapter 2 paper with contact angles greater than 150° for water and motor oil, and greater than 140° for *n*-hexadecane was developed through a three-step process. First, a commercially available debonding agent was used to manipulate the dimensions of the fiber network through efficient fines removal and modification of inter-fiber hydrogen bonding. Then an oxygen plasma was used to create nano-scale roughness on the micrometer-sized fibers and to remove residual fines that were blocking the inter-fiber pores. Finally, the paper was immersed in a fluorosilane solution to obtain a thin, low surface energy coating. This study marks the first report that uses debonder agents specifically to modify the anti-wetting properties of

paper substrates by controlling the topology of the fiber network. The processes used in this procedure are simple, cost effective and amenable to scale-up.

Chapter 3 demonstrates the feasibility of fabricating paper which not only repels oils and water, but also displays roll-off properties towards a wide range of oils and water. Unlike widely used approaches that rely on the deposition of nanoparticles or electrospun nanofibers to create superamphiphobic surfaces, our method generates a hierarchical structure as an inherent property of the substrate and displays good adhesion between the film and substrate. The two-step combination of plasma etch and vapor deposition enables fine tuning of nanoscale roughness and thereby facilitates enhanced fundamental understanding of the effect of micro- and nano-scale roughness on paper wetting properties. The surfaces maintain “roll-off” properties after dynamic impact tests, demonstrating their mechanical robustness. Furthermore, the superamphiphobic paper has high gas permeability due to pore volume enhancement by plasma etching, but maintains the mechanical flexibility and strength of untreated paper, despite the presence of nanostructures.

Oil-water separation is a worldwide concern due to the increasing emissions of oil-contaminated industrial water, frequent oil spills and the general shortage of clean drinking water. In Chapter 4 of this thesis, the understanding generated by our investigations of wetting control on paper was used to modify stainless steel (SS) meshes. Hydrophilic/underwater superoleophobic SS meshes were fabricated via a one-step solution-based coating method using methyltrimethoxysilane (MTMS). The dimensions of the meshes were varied to study the effect on wettability and separation efficiency. Coated meshes were then used for gravity-driven oil/water separation with oil-water

mixtures and oil-water emulsions in which water passed through the meshes while oil was retained. High water flux and separation efficiency were achieved on the coated meshes which do not require sophisticated preparation methods and only require relatively benign chemicals.

Developing liquid repellent surfaces with good mechanical durability is of great importance for applications where both anti-wetting properties and coating robustness are desired. In Chapter 5, we describe studies that investigated how various types of coatings react to different mechanical impacts on flat or textured surfaces. The surface energy of the coating material, the mechanical properties of the substrate and loading level of coating material were varied among coatings to analyze their respective effects on durability of the coated surface. It was found that tape peeling, a common testing method for coating adhesion, cannot be used as a direct indication of coating adhesion on non-compact or porous surfaces. Rotary abrasion and dynamic impact testing were proved to have significant impact on surfaces with artificial hierarchical structures. While coating thickness is critical for durability in many material applications, it lowers surface robustness most in the case of bending or even folding. General comments and recommendations on formulating a set of comprehensive evaluation methods to evaluate the mechanical durability are also provided so that more direct comparison can be performed among relevant studies in the future.

6.1 Future Work and Recommendations

While significant work has been completed to understand the wetting mechanism on fiber-based materials and create surfaces with controlled wetting properties, this thesis also provides inspiration and support for future work.

Plasma etching is environmentally benign relative to the use of solvents and also possesses unique capabilities for surface modification; therefore, this has been the principal method used in this thesis for generating surface roughness on fibers. Although commercial industrial scale roll-to-roll vacuum reactors that can be used for plasma-based textile processing of 3 - 4 m fabric width have been available for more than 10 years, efforts to incorporate plasma technology in routine textile manufacturing processes have not developed to their full potential because of hurdles such as electrical energy consumption, lack of process understanding and control, and concerns about equipment performance and robustness at industrial scale-up. [215-219] This thesis not only provides a deeper understanding of the plasma process, but also more motivation for the commercialization of plasma technology in such applications. Future studies that address the scalability issues should be explored.

We have demonstrated the effectiveness of using a debonder to fabricate highly amphiphobic paper in Chapter 2. While for applications such as food packaging, antimicrobial properties are desired in addition to liquid repellency. Researchers have reported the antimicrobial effect of quaternary ammonium salts like cetyltrimethylammonium bromide (CTAB) which is also a good pulp debonding agent. [220-222] CTAB can induce superoxide stress in bacteria such as E. coli cells. [223] Montazer et al. applied CTAB on their water and blood repellent nonwoven fabrics that were prepared with fluorochemical based water repellent agents. [222] The antimicrobial property of CTAB was verified through a reduced growth rate of various bacteria including S. aureus, E. coli and P. aeruginosa. Other studies that applied CTAB for antimicrobial purposes include enhancement of antibacterial activity of silver

nanoparticles, use against microbial contaminants in the cane sugar industry, and use in the solution state to inactivate and remove biofilms. [224-226] To create antimicrobial, grease resistant food packaging, CTAB could be added during pulp preparation or used as a dipping solution for prepared paper before the final step of chemistry modification. The dosage effect should also be explored by evaluating the relationship between paper amphiphobicity and antimicrobial performance.

The superamphiphobic paper we fabricated in Chapter 3 has been discussed based on widely acknowledged terminology and consensus in the literature such as the definition of “superamphiphobic” and the requirements for achieving superamphiphobic surfaces. The communication in this field regarding properties of such materials is still somewhat ambiguous and has not been adequately standardized. Some researchers have summarized the related research and attempted to discuss the terminology including “superamphiphobicity”, “super-non-wettable” and “superomniphobic”. [19,21,227,228] However, a clear definition has not been reached or recognized. A thorough review of topics such as “the definition of superamphiphobic”, “the hysteresis criterion”, “choices of the test liquids” and “effects of liquids’ polarity, density on repellency” is in great need and would help establish effective communication between researchers and reduce the tendency of repeatedly reporting works with actually similar wetting performance due to lack of standard evaluation method. A holistic overview of highly cited studies in the field would be provided and topics related information could be categorized and discussed to find the most recognized approaches employed in the literature. Finally, an evaluation system containing the clear definition of important terminology in the field and evaluation techniques and standards would be recommended.

Additionally, the oil-water separation work in Chapter 4 shows great potential to be used in large-scale industrial applications such as off-shore oil spills. However, more investigations are required before the separation system can be put into practical use. A few research groups have started to take into account the complexity of real world oil-water mixture such as salinity effect on interfacial behavior and its interaction with surfactants. [229-231] Salinity, temperature, surfactant contamination, oil composition and liquid pressure in the incoming mixture should be considered to assess the separation potential of our coated meshes in various applications. Further, considering the complexity of marine life and wastewater components, underwater biofouling should also be monitored throughout the operation cycles.

REFERENCES

[1] C.W. Extrand, Model for contact angles and hysteresis on rough and ultraphobic surfaces, Langmuir, 18 (2002) 7991-7999.

[2] P.S. Brown, O.D. Atkinson, J.P. Badyal, Ultrafast oleophobic-hydrophilic switching surfaces for antifogging, self-cleaning, and oil-water separation, ACS Appl Mater Interfaces, (2014).

[3] Y. Cai, L. Lin, Z.X. Xue, M.J. Liu, S.T. Wang, L. Jiang, Filefish-inspired surface design for anisotropic underwater oleophobicity, Adv. Funct. Mater., 24 (2014) 809-816.

[4] C. Corbella, I. Bialuch, M. Kleinschmidt, K. Bewilogua, Up-scaling the production of modified a-c:H coatings in the framework of plasma polymerization processes, Solid State Sciences, 11 (2009) 1768-1772.

[5] M. Grischke, K. Bewilogua, K. Trojan, H. Dimigen, Application-oriented modifications of deposition processes for diamond-like-carbon-based coatings, Surf. Coat. Technol., 74-75 (1995) 739-745.

[6] R.A. Hayn, J.R. Owens, S.A. Boyer, R.S. McDonald, H.J. Lee, Preparation of highly hydrophobic and oleophobic textile surfaces using microwave-promoted silane coupling, J. Mater. Sci., 46 (2011) 2503-2509.

[7] T.Y. Kim, B. Ingmar, K. Bewilogua, K.H. Oh, K.R. Lee, Wetting behaviours of a-c : H : Si : O film coated nano-scale dual rough surface, Chem. Phys. Lett., 436 (2007) 199-203.

[8] Y. Rahmawan, M.W. Moon, K.S. Kim, K.R. Lee, K.Y. Suh, Wrinkled, dual-scale structures of diamond-like carbon (dlc) for superhydrophobicity, Langmuir, 26 (2010) 484-491.

[9] S.A. John, S.J. Yeo, J.O. Cha, S.R. Park, J.Y. Jo, D.H. Cho, Method for fabricating superhydrophobic-material ptfe thin film in solar cell, involves injecting gas inside vacuum chamber, and utilizing chemical vapor deposition technique by controlling substrate temperature and evaporating substrate, in, Univ Kyunghee Ind Coop.

[10] Y.-Y. Zhang, Q. Ge, L.-L. Yang, X.-J. Shi, J.-J. Li, D.-Q. Yang, E. Sacher, Durable superhydrophobic ptfe films through the introduction of micro- and nanostructured pores, Appl. Surf. Sci., 339 (2015) 151-157.

[11] H. Bellanger, T. Darmanin, E.T. de Givenchy, F. Guittard, Chemical and physical pathways for the preparation of superoleophobic surfaces and related wetting theories, Chem. Rev., 114 (2014) 2694-2716.

[12] A. Tuteja, W. Choi, M. Ma, J.M. Mabry, S.A. Mazzella, G.C. Rutledge, G.H. McKinley, R.E. Cohen, Designing superoleophobic surfaces, Science, 318 (2007) 1618-1622.

[13] M.R. Cardoso, R.J. Martins, A. Dev, T. Voss, C.R. Mendonca, Highly hydrophobic hierarchical nanomicro roughness polymer surface created by stamping and laser micromachining, J. Appl. Polym. Sci., 132 (2015).

[14] H.J. Choi, J.H. Shin, S. Choo, S.W. Ryu, Y.D. Kim, H. Lee, Fabrication of superhydrophobic and oleophobic al surfaces by chemical etching and surface fluorination, Thin Solid Films, 585 (2015) 76-80.

[15] T. Darmanin, F. Guittard, Superoleophobic polymers with metal ion affinity toward materials with both oleophobic and hydrophilic properties, J. Colloid Interface Sci., 408 (2013) 101-106.

[16] W. Hao, Z.Z. Shao, Superhydrophobic and highly oleophobic nylon surface, Acta Chim. Sinica, 72 (2014) 1023-1028.

[17] G.N. Ren, Z.Z. Zhang, X.T. Zhu, B. Ge, K. Wang, X.H. Xu, X.H. Men, X.Y. Zhou, A facile method for imparting superoleophobicity to polymer substrates, Applied Physics a-Materials Science & Processing, 114 (2014) 1129-1133.

[18] Z.X. Xue, Y.Z. Cao, N. Liu, L. Feng, L. Jiang, Special wettable materials for oil/water separation, J. Mater. Chem. A., 2 (2014) 2445-2460.

[19] Z.L. Chu, S. Seeger, Superamphiphobic surfaces, Chem. Soc. Rev., 43 (2014) 2784-2798.

[20] H. Zhou, H.X. Wang, H.T. Niu, A. Gestos, T. Lin, Robust, self-healing superamphiphobic fabrics prepared by two-step coating of fluoro-containing polymer, fluoroalkyl silane, and modified silica nanoparticles, Adv. Funct. Mater., 23 (2013) 1664-1670.

[21] A.K. Kota, G. Kwon, A. Tuteja, The design and applications of superomniphobic surfaces, Npg Asia Materials, 6 (2014).

[22] S.J. Pan, A.K. Kota, J.M. Mabry, A. Tuteja, Superomniphobic surfaces for effective chemical shielding, J. Am. Chem. Soc., 135 (2013) 578-581.

[23] X. Deng, L. Mammen, H.J. Butt, D. Vollmer, Candle soot as a template for a transparent robust superamphiphobic coating, Science, 335 (2012) 67-70.

[24] H.F. Meng, S.T. Wang, J.M. Xi, Z.Y. Tang, L. Jiang, Facile means of preparing superamphiphobic surfaces on common engineering metals, J. Phys. Chem. C, 112 (2008) 11454-11458.

[25] J.M. Xi, L. Feng, L. Jiang, A general approach for fabrication of superhydrophobic and superamphiphobic surfaces, Appl. Phys. Lett., 92 (2008).

[26] Y.C. Sheen, Y.C. Huang, C.S. Liao, H.Y. Chou, F.C. Chang, New approach to fabricate an extremely super-amphiphobic surface based on fluorinated silica nanoparticles, Journal of Polymer Science Part B-Polymer Physics, 46 (2008) 1984-1990.

[27] H. Jin, X.L. Tian, O. Ikkala, R.H.A. Ras, Preservation of superhydrophobic and superoleophobic properties upon wear damage, ACS Appl. Mater. Interfaces, 5 (2013) 485-488.

[28] T. Darmanin, F. Guittard, S. Amigoni, E.T. de Givenchy, X. Noblin, R. Kofman, F. Celestini, Superoleophobic behavior of fluorinated conductive polymer films combining electropolymerization and lithography, Soft Matter, 7 (2011) 1053-1057.

[29] D. Xiong, G.J. Liu, L.Z. Hong, E.J.S. Duncan, Superamphiphobic diblock copolymer coatings, Chem. Mater., 23 (2011) 4357-4366.

[30] V.A. Ganesh, S.S. Dinachali, A.S. Nair, S. Ramakrishna, Robust superamphiphobic film from electrospun tio2 nanostructures, ACS Appl. Mater. Interfaces, 5 (2013) 1527-1532.

[31] C. Pereira, C. Alves, A. Monteiro, C. Magen, A.M. Pereira, A. Ibarra, M.R. Ibarra, P.B. Tavares, J.P. Araujo, G. Blanco, J.M. Pintado, A.P. Carvalho, J. Pires, M.F.R. Pereira, C. Freire, Designing novel hybrid materials by one-pot co-condensation: From hydrophobic mesoporous silica nanoparticles to superamphiphobic cotton textiles, ACS Appl. Mater. Interfaces, 3 (2011) 2289-2299.

[32] M. Im, H. Im, J.-H. Lee, J.-B. Yoon, Y.-K. Choi, A robust superhydrophobic and superoleophobic surface with inverse-trapezoidal microstructures on a large transparent flexible substrate, Soft Matter, 6 (2010) 1401-1404.

[33] A. Tuteja, W. Choi, J.M. Mabry, G.H. McKinley, R.E. Cohen, Robust omniphobic surfaces, Proc. Natl. Acad. Sci. U.S.A., 105 (2008) 18200-18205.

[34] L. Li, V. Breedveld, D.W. Hess, Design and fabrication of superamphiphobic paper surfaces, ACS Appl. Mater. Interfaces, 5 (2013) 5381-5386.

[35] W. Choi, A. Tuteja, S. Chhatre, J.M. Mabry, R.E. Cohen, G.H. McKinley, Fabrics with tunable oleophobicity, Adv. Mater., 21 (2009) 2190-2195.

[36] S. Michielsen, H.J. Lee, Design of a superhydrophobic surface using woven structures, Langmuir, 23 (2007) 6004-6010.

[37] J. Li, L. Yan, Q.L. Ouyang, F. Zha, Z.J. Jing, X. Li, Z.Q. Lei, Facile fabrication of translucent superamphiphobic coating on paper to prevent liquid pollution, Chem. Eng. J., 246 (2014) 238-243.

[38] X. Wang, H. Hu, Q. Ye, T. Gao, F. Zhou, Q. Xue, Superamphiphobic coatings with coralline-like structure enabled by one-step spray of polyurethane/carbon nanotube composites, J. Mater. Chem., 22 (2012) 9624-9631.

[39] I. Iavicoli, L. Fontana, V. Leso, A. Bergamaschi, The effects of nanomaterials as endocrine disruptors, Int. J. Mol. Sci, 14 (2013) 16732-16801.

[40] R. Landsiedel, E. Fabian, L. Ma-Hock, W. Wohlleben, K. Wiench, F. Oesch, B. van Ravenzwaay, Toxico-/biokinetics of nanomaterials, Arch. Toxicol., 86 (2012) 1021-1060.

[41] W.-S. Cho, R. Duffin, C.A. Poland, S.E.M. Howie, W. MacNee, M. Bradley, I.L. Megson, K. Donaldson, Metal oxide nanoparticles induce unique inflammatory footprints in the lung: Important implications for nanoparticle testing, Environ. Health Perspect., 118 (2010) 1699-1706.

[42] H. Zhou, H.X. Wang, H.T. Niu, J. Fang, Y. Zhao, T. Lin, Superstrong, chemically stable, superamphiphobic fabrics from particle-free polymer coatings, Advanced Materials Interfaces, 2 (2015).

[43] S.J. Chen, H.Y. Yu, B.C. Yang, Bioactive tio2 fiber films prepared by electrospinning method, J. Biomed. Mater. Res. Part A, 101 (2013) 64-74.

[44] J. Lee, C. Boo, W.H. Ryu, A.D. Taylor, M. Elimelech, Development of omniphobic desalination membranes using a charged electrospun nanofiber scaffold, ACS Appl. Mater. Interfaces, 8 (2016) 11154-11161.

[45] L. Xie, Z. Tang, L. Jiang, V. Breedveld, D.W. Hess, Creation of superhydrophobic wood surfaces by plasma etching and thin-film deposition, Surf. Coat. Technol., 281 (2015) 125-132.

[46] J.P. Youngblood, T.J. McCarthy, Ultrahydrophobic polymer surfaces prepared by simultaneous ablation of polypropylene and sputtering of poly(tetrafluoroethylene) using radio frequency plasma, Macromolecules, 32 (1999) 6800-6806.

[47] N.Y. Cui, N.M.D. Brown, Modification of the surface properties of a polypropylene (pp) film using an air dielectric barrier discharge plasma, Appl. Surf. Sci., 189 (2002) 31-38.

[48] B. Balu, V. Breedveld, D.W. Hess, Fabrication of "roll-off" and "sticky" superhydrophobic cellulose surfaces via plasma processing, Langmuir, 24 (2008) 4785-4790.

[49] B. Balu, J.S. Kim, V. Breedveld, D.W. Hess, Design of superhydrophobic paper/cellulose surfaces via plasma enhanced etching and deposition, Contact Angles, Wettability Adhes., 6 (2009) 235-249.

[50] N.V. Motlagh, R. Khani, S. Rahnama, Super dewetting surfaces: Focusing on their design and fabrication methods, Colloids Surf., A, 484 (2015) 528-546.

[51] Z. Tang, D.W. Hess, V. Breedveld, Fabrication of oleophobic paper with tunable hydrophilicity by treatment with non-fluorinated chemicals, J. Mater. Chem. A., 3 (2015) 14651-14660.

[52] X. Zhu, Z. Zhang, X. Xu, X. Men, J. Yang, X. Zhou, Q. Xue, Facile fabrication of a superamphiphobic surface on the copper substrate, J. Colloid Interface Sci., 367 (2012) 443-449.

[53] Z. Tang, H. Li, D.W. Hess, V. Breedveld, Effect of chain length on the wetting properties of alkyltrichlorosilane coated cellulose-based paper, Cellulose, 23 (2016) 1401-1413.

[54] R. Campos, A.J. Guenthner, A.J. Meuler, A. Tuteja, R.E. Cohen, G.H. McKinley, T.S. Haddad, J.M. Mabry, Superoleophobic surfaces through control of sprayed-on stochastic topography, Langmuir, 28 (2012) 9834-9841.

[55] K. Chiba, K. Kurogi, K. Monde, M. Hashimoto, M. Yoshida, H. Mayama, K. Tsujii, Super water- and highly oil-repellent films made of fluorinated poly(alkylpyrroles), Colloids Surf., A, 354 (2010) 234-239.

[56] A. Diouf, T. Darmanin, S.Y. Dieng, F. Guittard, Superhydrophobic (low adhesion) and parahydrophobic (high adhesion) surfaces with micro/nanostructures or nanofilaments, J. Colloid Interface Sci., 453 (2015) 42-47.

[57] K. Ellinas, A. Tserepi, E. Gogolides, From superamphiphobic to amphiphilic polymeric surfaces with ordered hierarchical roughness fabricated with colloidal lithography and plasma nanotexturing, Langmuir, 27 (2011) 3960-3969.

[58] Y.-C. Sheen, Y.-C. Huang, C.-S. Liao, H.-Y. Chou, F.-C. Chang, New approach to fabricate an extremely super-amphiphobic surface based on fluorinated silica nanoparticles, J. Polym. Sci., Part B: Polym. Phys., 46 (2008) 1984-1990.

[59] A.C. Glavan, R.V. Martinez, A.B. Subramaniam, H.J. Yoon, R.M.D. Nunes, H. Lange, M.M. Thuo, G.M. Whitesides, Omniphobic "r-f paper" produced by silanization of paper with fluoroalkyltrichlorosilanes, Adv. Funct. Mater., 24 (2014) 60-70.

[60] D. Wang, X. Wang, X. Liu, F. Zhou, Engineering a titanium surface with controllable oleophobicity and switchable oil adhesion, J. Phys. Chem. C, 114 (2010) 9938-9944.

[61] N. Chen, D.H. Kim, P. Kovacik, H. Sojoudi, M.H. Wang, K.K. Gleason, Polymer thin films and surface modification by chemical vapor deposition: Recent progress, in: J.M. Prausnitz (Ed.) Annual review of chemical and biomolecular engineering, vol 7, 2016, pp. 373-393.

[62] R. Gordon, Chemical vapor deposition of coatings on glass, J. Non-Cryst. Solids, 218 (1997) 81-91.

[63] W.J. Lackey, S. Vaidyaraman, B.N. Beckloff, T.S. Moss, J.S. Lewis, Mass transfer and kinetics of the chemical vapor deposition of sic onto fibers, J. Mater. Res., 13 (1998) 2251-2261.

[64] N.P. Bansal, R.M. Dickerson, Tensile strength and microstructural characterization of hpz ceramic fibers, Materials Science and Engineering a-Structural Materials Properties Microstructure and Processing, 222 (1997) 149-157.

[65] X. Wu, I. Wyman, G.W. Zhang, J. Lin, Z.Q. Liu, Y. Wang, H. Hu, Preparation of superamphiphobic polymer-based coatings via spray- and dip-coating strategies, Prog. Org. Coat., 90 (2016) 463-471.

[66] Y. Li, Z.Z. Zhang, B. Ge, X.H. Men, Q.J. Xue, A versatile and efficient approach to separate both surfactant-stabilized water-in-oil and oil-in-water emulsions, Sep. Purif. Technol., 176 (2017) 1-7.

[67] W.J. Ma, Z.F. Guo, J.T. Zhao, Q. Yu, F. Wang, J.Q. Han, H. Pan, J.F. Yao, Q.L. Zhang, S.K. Samal, S.C. De Smedt, C.B. Huang, Polyimide/cellulose acetate core/shell electrospun fibrous membranes for oil-water separation, Sep. Purif. Technol., 177 (2017) 71-85.

[68] S.K. Hubadillah, M.H.D. Othman, Z. Harun, A.F. Ismail, M.A. Rahman, J. Jaafar, S.M. Jamil, N.H. Mohtor, Superhydrophilic, low cost kaolin-based hollow fibre membranes for efficient oily-wastewater separation, Mater. Lett., 191 (2017) 119-122.

[69] O. Oribayo, X.S. Feng, G.L. Rempel, Q.M. Pan, Modification of formaldehyde-melamine-sodium bisulfite copolymer foam and its application as effective sorbents for clean up of oil spills, Chem. Eng. Sci., 160 (2017) 384-395.

[70] Q.Y. Cheng, D.D. Ye, C.Y. Chang, L.N. Zhang, Facile fabrication of superhydrophilic membranes consisted of fibrous tunicate cellulose nanocrystals for highly efficient oil/water separation, J. Membr. Sci., 525 (2017) 1-8.

[71] U.B. Gunatilake, J. Bandara, Efficient removal of oil from oil contaminated water by superhydrophilic and underwater superoleophobic nano/micro structured tio2 nanofibers coated mesh, Chemosphere, 171 (2017) 134-141.

[72] Q. Wang, M.G. Yu, G.X. Chen, Q.F. Chen, J.F. Tian, Robust fabrication of fluorine-free superhydrophobic steel mesh for efficient oil/water separation, J. Mater. Sci., 52 (2017) 2549-2559.

[73] T. Zhang, L.Y. Kong, Y.T. Dai, X.J. Yue, J. Rong, F.X. Qiu, J.M. Pan, Enhanced oils and organic solvents absorption by polyurethane foams composites modified with mno2 nanowires, Chem. Eng. J., 309 (2017) 7-14.

[74] J.H. Lee, D.H. Kim, Y.D. Kim, High-performance, recyclable and superhydrophobic oil absorbents consisting of cotton with a polydimethylsiloxane shell, Journal of Industrial and Engineering Chemistry, 35 (2016) 140-145.

[75] H.Z. Sai, R. Fu, L. Xing, J.H. Xiang, Z.Y. Li, F. Li, T. Zhang, Surface modification of bacterial cellulose aerogels' web-like skeleton for oil/water separation, ACS Appl. Mater. Interfaces, 7 (2015) 7373-7381.

[76] Y. Yang, H. Yi, C.Y. Wang, Oil absorbents based on melamine/lignin by a dip adsorbing method, Acs Sustainable Chemistry & Engineering, 3 (2015) 3012-3018.

[77] A.J. Zhang, M.J. Chen, C. Du, H.Z. Guo, H. Bai, L. Li, Poly(dimethylsiloxane) oil absorbent with a three-dimensionally interconnected porous structure and swellable skeleton, ACS Appl. Mater. Interfaces, 5 (2013) 10201-10206.

[78] C.P. Su, H. Yang, S. Song, B. Lu, R. Chen, A magnetic superhydrophilic/oleophobic sponge for continuous oil-water separation, Chem. Eng. J., 309 (2017) 366-373.

[79] Q.L. Ma, H.F. Cheng, A.G. Fane, R. Wang, H. Zhang, Recent development of advanced materials with special wettability for selective oil/water separation, Small, 12 (2016) 2186-2202.

[80] F. Hoshyargar, M. Mahajan, Anuradha, S.V. Bhosale, L. Kyratzis, A.I. Bhatt, A.P. O'Mullane, Superhydrophobic fabrics for oil/water separation based on the metal-organic charge-transfer complex cutcnaq, Chempluschem, 81 (2016) 378-383.

[81] Z.X. Kang, S.S. Wang, L.L. Fan, Z.Y. Xiao, R.M. Wang, D.F. Sun, Surface wettability switching of metal-organic framework mesh for oil water separation, Mater. Lett., 189 (2017) 82-85.

[82] B.T. Song, Simple and fast fabrication of superhydrophobic metal wire mesh for efficiently gravity-driven oil/water separation, Marine Pollution Bulletin, 113 (2016) 211-215.

[83] J.H. Li, H.M. Cheng, C.Y. Chan, P.F. Ng, L. Chen, B. Fei, J.H. Xin, Superhydrophilic and underwater superoleophobic mesh coating for efficient oil-water separation, Rsc Advances, 5 (2015) 51537-51541.

[84] Z.Y. Luo, K.X. Chen, Y.Q. Wang, J.H. Wang, D.C. Mo, S.S. Lyu, Superhydrophilic nickel nanoparticles with core-shell structure to decorate copper mesh for efficient oil/water separation, J. Phys. Chem. C, 120 (2016) 12685-12692.

[85] P.H.H. Duong, T.S. Chung, Application of thin film composite membranes with forward osmosis technology for the separation of emulsified oil-water, J. Membr. Sci., 452 (2014) 117-126.

[86] J.J. Li, Y.N. Zhou, Z.H. Luo, Smart fiber membrane for ph-induced oil/water separation, ACS Appl. Mater. Interfaces, 7 (2015) 19643-19650.

[87] X.T. Zhu, Z.Z. Zhang, B. Ge, X.H. Men, X.Y. Zhou, Q.J. Xue, A versatile approach to produce superhydrophobic materials used for oil-water separation, J. Colloid Interface Sci., 432 (2014) 105-108.

[88] M.M. Liu, J. Li, Z.G. Guo, Polyaniline coated membranes for effective separation of oil-in-water emulsions, J. Colloid Interface Sci., 467 (2016) 261-270.

[89] C. Aulin, S.H. Yun, L. Wagberg, T. Lindstrom, Design of highly oleophobic cellulose surfaces from structured silicon templates, ACS Appl. Mater. Interfaces, 1 (2009) 2443-2452.

[90] T. Darmanin, F. Guittard, One-pot method for build-up nanoporous super oil-repellent films, J. Colloid Interface Sci., 335 (2009) 146-149.

[91] P. Kim, T.S. Wong, J. Alvarenga, M.J. Kreder, W.E. Adorno-Martinez, J. Aizenberg, Liquid-infused nanostructured surfaces with extreme anti-ice and anti-frost performance, Acs Nano, 6 (2012) 6569-6577.

[92] A.K. Kota, Y.X. Li, J.M. Mabry, A. Tuteja, Hierarchically structured superoleophobic surfaces with ultralow contact angle hysteresis, Adv. Mater., 24 (2012) 5838-5843.

[93] T.P.N. Nguyen, R. Dufour, V. Thomy, V. Senez, R. Boukherroub, Y. Coffinier, Fabrication of superhydrophobic and highly oleophobic silicon-based surfaces via electroless etching method, Appl. Surf. Sci., 295 (2014) 38-43.

[94] X.H. Men, X.C. Shi, B. Ge, Y. Li, X.T. Zhu, Y. Li, Z.Z. Zhang, Novel transparent, liquid-repellent smooth surfaces with mechanical durability, Chem. Eng. J., 296 (2016) 458-465.

[95] A. Milionis, I.S. Bayer, E. Loth, Recent progress in evaluating mechanical durability of liquid repellent surfaces, in: K.L. Mittal (Ed.) Advances in contact angle, wettability and adhesion, vol 2, 2015, pp. 211-258.

[96] A. Milionis, E. Loth, I.S. Bayer, Recent advances in the mechanical durability of superhydrophobic materials, Adv. Colloid Interface Sci., 229 (2016) 57-79.

[97] M. Paven, R. Fuchs, T. Yakabe, D. Vollmer, M. Kappl, A.N. Itakura, H.J. Butt, Mechanical properties of highly porous super liquid-repellent surfaces, Adv. Funct. Mater., 26 (2016) 4914-4922.

[98] Z. Chu, S. Seeger, Robust superhydrophobic wood obtained by spraying silicone nanoparticles, Rsc Advances, 5 (2015) 21999-22004.

[99] H.D. Wang, H. Zhou, A. Gestos, J. Fang, T. Lin, Robust, superamphiphobic fabric with multiple self-healing ability against both physical and chemical damages, ACS Appl. Mater. Interfaces, 5 (2013) 10221-10226.

[100] Z. Geng, J.H. He, An effective method to significantly enhance the robustness and adhesion-to-substrate of high transmittance superamphiphobic silica thin films, J. Mater. Chem. A., 2 (2014) 16601-16607.

[101] X. Zhang, W.Z. Zhu, G.J. He, P.Y. Zhang, Z.J. Zhang, I.P. Parkin, Flexible and mechanically robust superhydrophobic silicone surfaces with stable cassie-baxter state, J. Mater. Chem. A., 4 (2016) 14180-14186.

[102] X. Deng, L. Mammen, Y.F. Zhao, P. Lellig, K. Mullen, C. Li, H.J. Butt, D. Vollmer, Transparent, thermally stable and mechanically robust superhydrophobic surfaces made from porous silica capsules, Adv. Mater., 23 (2011) 2962-+.

[103] A. Davis, Y.H. Yeong, A. Steele, E. Lothand, G. de Combarieau, Durability of a superhydrophobic nanocomposite coating under extended replicated rain impact, 2012.

[104] R. Ramachandran, K. Sobolev, M. Nosonovsky, Dynamics of droplet impact on hydrophobic/icephobic concrete with the potential for superhydrophobicity, Langmuir, 31 (2015) 1437-1444.

[105] A. Davis, Y.H. Yeong, A. Steele, E. Loth, I.S. Bayer, Nanocomposite coating superhydrophobicity recovery after prolonged high-impact simulated rain, Rsc Advances, 4 (2014) 47222-47226.

[106] H. Sojoudi, M. Wang, N.D. Boscher, G.H. McKinley, K.K. Gleason, Durable and scalable icephobic surfaces: Similarities and distinctions from superhydrophobic surfaces, Soft Matter, 12 (2016) 1938-1963.

[107] Z.Q. Shi, I. Wyman, G.J. Liu, H. Hu, H.L. Zou, J.W. Hu, Preparation of water-repellent cotton fabrics from fluorinated diblock copolymers and evaluation of their durability, Polymer, 54 (2013) 6406-6414.

[108] Y. Yoo, J.B. You, W. Choi, S.G. Im, A stacked polymer film for robust superhydrophobic fabrics, Polymer Chemistry, 4 (2013) 1664-1671.

[109] H.X. Wang, Y.H. Xue, J. Ding, L.F. Feng, X.G. Wang, T. Lin, Durable, self-healing superhydrophobic and superoleophobic surfaces from fluorinated-decyl polyhedral oligomeric silsesquioxane and hydrolyzed fluorinated alkyl silane, Angew. Chem. Int. Ed., 50 (2011) 11433-11436.

[110] J.P. Zhang, B.C. Li, L. Wu, A.Q. Wang, Facile preparation of durable and robust superhydrophobic textiles by dip coating in nanocomposite solution of organosilanes, Chem. Commun., 49 (2013) 11509-11511.

[111] G.H. Xi, J. Wang, G.Y. Luo, Y.H. Zhu, W.C. Fan, M.Q. Huang, H.Q. Wang, X.D. Liu, Healable superhydrophobicity of novel cotton fabrics modified via one-pot mist copolymerization, Cellulose, 23 (2016) 915-927.

[112] T.H. Kim, S.H. Ha, N.S. Jang, J. Kim, J.H. Kim, J.K. Park, D.W. Lee, J. Lee, S.H. Kim, J.M. Kim, Simple and cost-effective fabrication of highly flexible, transparent superhydrophobic films with hierarchical surface design, ACS Appl. Mater. Interfaces, 7 (2015) 5289-5295.

[113] S. Hoshian, V. Jokinen, S. Franssila, Robust hybrid elastomer/metal-oxide superhydrophobic surfaces, Soft Matter, 12 (2016) 6526-6535.

[114] S.S. Latthe, P. Sudhagar, A. Devadoss, A.M. Kumar, S.H. Liu, C. Terashima, K. Nakata, A. Fujishima, A mechanically bendable superhydrophobic steel surface with self-cleaning and corrosion-resistant properties, J. Mater. Chem. A., 3 (2015) 14263-14271.

[115] V. Saceviciene, M. Juciene, V. Bieliuniene, V. Cepauskiene, V. Urbelis, Investigation of the wettability of the hydrophobic textile after mechanical treatments, Proceedings of the Estonian Academy of Sciences, 64 (2015) 118-123.

[116] D.T. Ge, L.L. Yang, C.B. Wang, E. Lee, Y.Q. Zhang, S. Yang, A multi-functional oil-water separator from a selectively pre-wetted superamphiphobic paper, Chem. Commun., 51 (2015) 6149-6152.

[117] G. Zhang, J. Hu, G. Liu, H. Zou, Y. Tu, F. Li, S. Hu, H. Luo, Bi-functional random copolymers for one-pot fabrication of superamphiphobic particulate coatings, J. Mater. Chem. A., 1 (2013) 6226-6237.

[118] J.P. Joseleau, V. Chevalier-Billosta, K. Ruel, Interaction between microfibrillar cellulose fines and fibers: Influence on pulp qualities and paper sheet properties, Cellulose, 19 (2012) 769-777.

[119] R.S. Seth, The measurement and significance of fines - their addition to pulp improves sheet consolidation, Pulp & Paper-Canada, 104 (2003) 41-44.

[120] P. Fatehi, K. Outhouse, H.N. Xiao, Cationic alkoxylated amine surfactant as a debonding agent for papers made of sulfite-bleached fibers, Ind. Eng. Chem. Res., 48 (2009) 749-754.

[121] P. Fatehi, K.C. Outhouse, H.N. Xiao, Y.H. Ni, Debonding performance of various cationic surfactants on networks made of bleached kraft fibers, Ind. Eng. Chem. Res., 49 (2010) 11402-11407.

[122] M. Talaeipoor, R. Imani, Effects of debonding agents and refining on the properties of deinked pulp, Tappi J., 7 (2008) 12-14.

[123] T.L. Lu, G.Z. Liang, Z. Guo, Preparation and characterization of organic-inorganic hybrid composites based on multiepoxy silsesquioxane and cyanate resin, J. Appl. Polym. Sci., 101 (2006) 3652-3658.

[124] E.W. Washburn, Note on a method of determining the distribution of pore sizes in a porous material, Proc. Natl. Acad. Sci. U.S.A., 7 (1921) 115-116.

[125] M.J. Moura, P.J. Ferreira, M.M. Figueiredo, Mercury intrusion porosimetry in pulp and paper technology, Powder Technol., 160 (2005) 61-66.

[126] A. Koubaa, Z. Koran, Measure of the internal bond strength of paper/board, Tappi J., 78 (1995) 103-112.

[127] K. Niskanen, J. Sirvio, R. Wathen, Tensile strength of paper revisited, 2005.

[128] D. Wu, S.-z. Wu, Q.-D. Chen, S. Zhao, H. Zhang, J. Jiao, J.A. Piersol, J.-N. Wang, H.-B. Sun, L. Jiang, Facile creation of hierarchical pdms microstructures with extreme underwater superoleophobicity for anti-oil application in microfluidic channels, Lab on a Chip, 11 (2011) 3873-3879.

[129] W.Z. Fan, J. Qian, F. Bai, Y.B. Li, C.W. Wang, Q.Z. Zhao, A facile method to fabricate superamphiphobic polytetrafluoroethylene surface by femtosecond laser pulses, Chem. Phys. Lett., 644 (2016) 261-266.

[130] S. Barthwal, Y.S. Kim, S.H. Lim, Mechanically robust superamphiphobic aluminum surface with nanopore-embedded microtexture, Langmuir, 29 (2013) 11966-11974.

[131] Y.W. Sun, L.L. Wang, Y.Z. Gao, D.M. Guo, Preparation of stable superamphiphobic surfaces on ti-6al-4v substrates by one-step anodization, Appl. Surf. Sci., 324 (2015) 825-830.

[132] W. Kwak, W. Hwang, Facile method for preparing superoleophobic surfaces with hierarchical microcubic/nanowire structures, Nanotechnology, 27 (2016).

[133] A. Steele, I. Bayer, E. Loth, Inherently superoleophobic nanocomposite coatings by spray atomization, Nano Lett., 9 (2009) 501-505.

[134] Y. Wang, B. Bhushan, Wear-resistant and antismudge superoleophobic coating on polyethylene terephthalate substrate using sio2 nanoparticles, ACS Appl. Mater. Interfaces, 7 (2015) 743-755.

[135] T.I. Wong, H. Wang, F.K. Wang, S.L. Sin, C.G. Quan, S.J. Wang, X.D. Zhou, Development of a highly transparent superamphiphobic plastic sheet by nanoparticle and chemical coating, J. Colloid Interface Sci., 467 (2016) 245-252.

[136] X. Men, X. Shi, B. Ge, Y. Li, X. Zhu, Y. Li, Z. Zhang, Novel transparent, liquid-repellent smooth surfaces with mechanical durability, Chem. Eng. J., 296 (2016) 458-465.

[137] L.M. Wang, T.J. McCarthy, Covalently attached liquids: Instant omniphobic surfaces with unprecedented repellency, Angew. Chem. Int. Ed., 55 (2016) 244-248.

[138] T. Jiang, Z.G. Guo, W.M. Liu, Biomimetic superoleophobic surfaces: Focusing on their fabrication and applications, J. Mater. Chem. A., 3 (2015) 1811-1827.

[139] S.Y. Lee, Y. Rahmawan, S. Yang, Transparent and superamphiphobic surfaces from mushroom-like micropillar arrays, ACS Appl. Mater. Interfaces, 7 (2015) 24197-24203.

[140] S. Peng, W. Deng, A simple method to prepare superamphiphobic aluminum surface with excellent stability, Colloids Surf., A, 481 (2015) 143-150.

[141] K. Ellinas, M. Chatzipetrou, I. Zergioti, A. Tserepi, E. Gogolides, Superamphiphobic polymeric surfaces sustaining ultrahigh impact pressures of aqueous high-and low-surface-tension mixtures, tested with laser-induced forward transfer of drops, Adv. Mater., 27 (2015) 2231-2235.

[142] L. Li, S. Roethel, V. Breedveld, D.W. Hess, Creation of low hysteresis superhydrophobic paper by deposition of hydrophilic diamond-like carbon films, Cellulose, 20 (2013) 3219-3226.

[143] X.L. Tian, T. Verho, R.H.A. Ras, Moving superhydrophobic surfaces toward real-world applications, Science, 352 (2016) 142-143.

[144] E. Pierce, F.J. Carmona, A. Amirfazli, Understanding of sliding and contact angle results in tilted plate experiments, Colloids Surf., A, 323 (2008) 73-82.

[145] L. Jiang, Z. Tang, R.M. Clinton, D.W. Hess, V. Breedveld, Fabrication of highly amphiphobic paper using pulp debonder, Cellulose, 23 (2016) 3885-3899.

[146] H.J. Lee, C.R. Willis, C.A. Stone, Modeling and preparation of a super-oleophobic non-woven fabric, J. Mater. Sci., 46 (2011) 3907-3913.

[147] T. Wang, J. Cui, S. Ouyang, W. Cui, S. Wang, A new approach to understand the cassie state of liquids on superamphiphobic materials, Nanoscale, 8 (2016) 3031-3039.

[148] F. Li, M. Du, Q. Zheng, Dopamine/silica nanoparticle assembled, microscale porous structure for versatile superamphiphobic coating, Acs Nano, 10 (2016) 2910-2921.

[149] D. Kim, H. Im, M.J. Kwak, E. Byun, S.G. Im, Y.K. Choi, A superamphiphobic sponge with mechanical durability and a self-cleaning effect, Sci. Rep., 6 (2016).

[150] L. Xu, D. Zhu, X. Lu, Q. Lu, Transparent, thermally and mechanically stable superhydrophobic coating prepared by an electrochemical template strategy, J. Mater. Chem. A., 3 (2015) 3801-3807.

[151] A.C. Wolfaardt, L.G. Underhill, R. Altwegg, J. Visagie, A.J. Williams, Impact of the treasure oil spill on african penguins spheniscus demersus at dassen island: Case study of a rescue operation, Afr. J. Marine Sci., 30 (2008) 405-419.

[152] S.M. Murphy, R.H. Day, J.A. Wiens, K.R. Parker, Effects of the exxon valdez oil spill on birds: Comparisons of pre- and post-spill surveys in prince william sound, alaska, Condor, 99 (1997) 299-313.

[153] B. Wang, W.X. Liang, Z.G. Guo, W.M. Liu, Biomimetic super-lyophobic and super-lyophilic materials applied for oil/water separation: A new strategy beyond nature, Chem. Soc. Rev., 44 (2015) 336-361.

[154] L. Yang, C.T. Lai, Biological treatment of mineral oil in a salty environment, Water Sci. Technol., 42 (2000) 369-375.

[155] S. Sabir, Approach of cost-effective adsorbents for oil removal from oily water, Crit. Rev. Env. Sci. Technol., 45 (2015) 1916-1945.

[156] M.A. Hubbe, O.J. Rojas, M. Fingas, B.S. Gupta, Cellulosic substrates for removal of pollutants from aqueous systems: A review. 3. Spilled oil and emulsified organic liquids, Bioresources, 8 (2013) 3038-3097.

[157] L. Feng, Z.Y. Zhang, Z.H. Mai, Y.M. Ma, B.Q. Liu, L. Jiang, D.B. Zhu, A super-hydrophobic and super-oleophilic coating mesh film for the separation of oil and water, Angew. Chem. Int. Ed., 43 (2004) 2012-2014.

[158] T.T. Lim, X.F. Huang, Evaluation of kapok (ceiba pentandra (l.) gaertn.) as a natural hollow hydrophobic-oleophilic fibrous sorbent for oil spill cleanup, Chemosphere, 66 (2007) 955-963.

[159] Y.Z. Cao, X.Y. Zhang, L. Tao, K. Li, Z.X. Xue, L. Feng, Y. Wei, Mussel-inspired chemistry and michael addition reaction for efficient oil/water separation, ACS Appl. Mater. Interfaces, 5 (2013) 4438-4442.

[160] W.B. Zhang, Y.Z. Zhu, X. Liu, D. Wang, J.Y. Li, L. Jiang, J. Jin, Salt-induced fabrication of superhydrophilic and underwater superoleophobic paa-g-pvdf membranes for effective separation of oil-in-water emulsions, Angew. Chem. Int. Ed., 53 (2014) 856-860.

[161] M.H. Tai, J. Juay, D.D. Sun, J.O. Leckie, Carbon-silica composite nanofiber membrane for high flux separation of water-in-oil emulsion - performance study and fouling mechanism, Sep. Purif. Technol., 156 (2015) 952-960.

[162] X. Du, X. Huang, X.Y. Li, X.M. Meng, L. Yao, J.H. He, H.W. Huang, X.J. Zhang, Wettability behavior of special microscale zno nail-coated mesh films for oil-water separation, J. Colloid Interface Sci., 458 (2015) 79-86.

[163] J.C. Gu, P. Xiao, J. Chen, J.W. Zhang, Y.J. Huang, T. Chen, Janus polymer/carbon nanotube hybrid membranes for oil/water separation, ACS Appl. Mater. Interfaces, 6 (2014) 16204-16209.

[164] D.H. Kim, M.C. Jung, S.H. Cho, S.H. Kim, H.Y. Kim, H.J. Lee, K.H. Oh, M.W. Moon, Uv-responsive nano-sponge for oil absorption and desorption, Sci. Rep., 5 (2015).

[165] D. Hu, X.Y. Li, L. Li, C.F. Yang, Designing high-caliber nonwoven filter mats for coalescence filtration of oil/water emulsions, Sep. Purif. Technol., 149 (2015) 65-73.

[166] Y.L. He, J.H. Li, K. Luo, L.F. Li, J.B. Chen, J.Y. Li, Engineering reduced graphene oxide aerogel produced by effective gamma-ray radiation-induced self-assembly and its application for continuous oil-water separation, Ind. Eng. Chem. Res., 55 (2016) 3775-3781.

[167] P.S. Brown, O. Atkinson, J.P.S. Badyal, Ultrafast oleophobic-hydrophilic switching surfaces for antifogging, self-cleaning, and oil water separation, ACS Appl. Mater. Interfaces, 6 (2014) 7504-7511.

[168] J. Yang, L.T. Yin, H. Tang, H.J. Song, X.N. Gao, K. Liang, C.S. Li, Polyelectrolyte-fluorosurfactant complex-based meshes with superhydrophilicity and superoleophobicity for oil/water separation, Chem. Eng. J., 268 (2015) 245-250.

[169] X.Y. Zhu, W.T. Tu, K.H. Wee, R.B. Bai, Effective and low fouling oil/water separation by a novel hollow fiber membrane with both hydrophilic and oleophobic surface properties, J. Membr. Sci., 466 (2014) 36-44.

[170] S.S. Shen, K.P. Liu, X.J. Zhou, R.B. Bai, I. Destech Publicat, Study in oil/water separation with a novel hollow fiber membrane showing hydrophilic and oleophobic surface properties, International Conference on Energy, Environment and Chemical Engineering (Iceece 2015), (2015) 29-33.

[171] Z.G. Xu, Y. Zhao, H.X. Wang, H. Zhou, C.X. Qin, X.G. Wang, T. Lin, Fluorine-free superhydrophobic coatings with ph-induced wettability transition for controllable oil-water separation, ACS Appl. Mater. Interfaces, 8 (2016) 5661-5667.

[172] J. Yang, H.J. Song, X.H. Yan, H. Tang, C.S. Li, Superhydrophilic and superoleophobic chitosan-based nanocomposite coatings for oil/water separation, Cellulose, 21 (2014) 1851-1857.

[173] A.M. Kietzig, S.G. Hatzikiriakos, P. Englezos, Patterned superhydrophobic metallic surfaces, Langmuir, 25 (2009) 4821-4827.

[174] D. Pappas, A. Bujanda, J.D. Demaree, J.K. Hirvonen, W. Kosik, R. Jensen, S. McKnight, Surface modification of polyamide fibers and films using atmospheric plasmas, Surf. Coat. Technol., 201 (2006) 4384-4388.

[175] R.V. Lakshmi, P. Bera, C. Anandan, B.J. Basu, Effect of the size of silica nanoparticles on wettability and surface chemistry of sol-gel superhydrophobic and oleophobic nanocomposite coatings, Appl. Surf. Sci., 320 (2014) 780-786.

[176] M. Wolfs, T. Darmanin, F. Guittard, Versatile superhydrophobic surfaces from a bioinspired approach, Macromolecules, 44 (2011) 9286-9294.

[177] A.K. Kota, G. Kwon, W. Choi, J.M. Mabry, A. Tuteja, Hygro-responsive membranes for effective oil-water separation, Nat. Commun., 3 (2012).

[178] T. Young, An essay on the cohesion of fluids, Philos. Trans. R. Soc., 95 (1805) 65-87.

[179] L. Yan, J. Li, W.J. Li, F. Zha, H. Feng, D.C. Hu, A photo-induced zno coated mesh for on-demand oil/water separation based on switchable wettability, Mater. Lett., 163 (2016) 247-249.

[180] M.A. Gondal, M.S. Sadullah, M.A. Dastageer, G.H. McKinley, D. Panchanathan, K.K. Varanasi, Study of factors governing oil-water separation process using tio2 films prepared by spray deposition of nanoparticle dispersions, ACS Appl. Mater. Interfaces, 6 (2014) 13422-13429.

[181] C.L. Zhou, J. Cheng, K. Hou, A. Zhao, P.H. Pi, X.F. Wen, S.P. Xu, Superhydrophilic and underwater superoleophobic titania nanowires surface for oil repellency and oil/water separation, Chem. Eng. J., 301 (2016) 249-256.

[182] T. Yu, G.L. Xu, X.W. Wang, J. Yang, J. Hu, Fabrication of oil-water separation filter paper by simple impregnation with fluorinated poly-acrylate emulsion, Bioresources, 9 (2014) 4421-4429.

[183] J. Prystupa, Fluorine-a current literature review. An nrc and atsdr based review of safety standards for exposure to fluorine and fluorides, Toxicol. Mech. Methods, 21 (2011) 103-170.

[184] Y.Z. Cao, N. Liu, W.F. Zhang, L. Feng, Y. Wei, One-step coating toward multifunctional applications: Oil/water mixtures and emulsions separation and contaminants adsorption, ACS Appl. Mater. Interfaces, 8 (2016) 3333-3339.

[185] K. Rohrbach, Y. Li, H. Zhu, Z. Liu, J. Dai, J. Andreasen, L. Hu, A cellulose based hydrophilic, oleophobic hydrated filter for water/oil separation, Chem. Commun., 50 (2014) 13296-13299.

[186] U.C. Paul, D. Fragouli, I.S. Bayer, A. Athanassiou, Functionalized cellulose networks for efficient oil removal from oil-water emulsions, Polymers, 8 (2016).

[187] B. Chakrabarty, A.K. Ghoshal, M.K. Purkait, Ultrafiltration of stable oil-in-water emulsion by polysulfone membrane, J. Membr. Sci., 325 (2008) 427-437.

[188] J. Zhong, X.J. Sun, C.L. Wang, Treatment of oily wastewater produced from refinery processes using flocculation and ceramic membrane filtration, Sep. Purif. Technol., 32 (2003) 93-98.

[189] H. Ju, B.D. McCloskey, A.C. Sagle, Y.H. Wu, V.A. Kusuma, B.D. Freeman, Crosslinked poly(ethylene oxide) fouling resistant coating materials for oil/water separation, J. Membr. Sci., 307 (2008) 260-267.

[190] X.F. Wang, X.M. Chen, K. Yoon, D.F. Fang, B.S. Hsiao, B. Chu, High flux filtration medium based on nanofibrous substrate with hydrophilic nanocomposite coating, Environ. Sci. Technol., 39 (2005) 7684-7691.

[191] Z. Shi, W.B. Zhang, F. Zhang, X. Liu, D. Wang, J. Jin, L. Jiang, Ultrafast separation of emulsified oil/water mixtures by ultrathin free-standing single-walled carbon nanotube network films, Adv. Mater., 25 (2013) 2422-2427.

[192] W.B. Zhang, Z. Shi, F. Zhang, X. Liu, J. Jin, L. Jiang, Superhydrophobic and superoleophilic pvdf membranes for effective separation of water-in-oil emulsions with high flux, Adv. Mater., 25 (2013) 2071-2076.

[193] Y. Si, Q.X. Fu, X.Q. Wang, J. Zhu, J.Y. Yu, G. Sun, B. Ding, Superelastic and superhydrophobic nanofiber-assembled cellular aerogels for effective separation of oil/water emulsions, Acs Nano, 9 (2015) 3791-3799.

[194] P.C. Chen, Z.K. Xu, Mineral-coated polymer membranes with superhydrophilicity and underwater superoleophobicity for effective oil/water separation, Sci. Rep., 3 (2013).

[195] N.A. Gomez, R. Abonia, H. Cadavid, I.H. Vargas, Chemical and spectroscopic characterization of a vegetable oil used as dielectric coolant in distribution transformers, J. Braz. Chem. Soc., 22 (2011) 2292-2303.

[196] H. Dong, Z. Zhang, M.-H. Lee, D.W. Mueller, R.F. Reidy, Sol-gel polycondensation of methyltrimethoxysilane in ethanol studied by si-29 nmr spectroscopy using a two-step acid/base procedure, J. Sol-Gel Sci. Technol., 41 (2007) 11-17.

[197] H.J. Dong, M. Lee, R.D. Thomas, Z.P. Zhang, R.F. Reidy, D.W. Mueller, Methyltrimethoxysilane sol-gel polymerization in acidic ethanol solutions studied by si-29 nmr spectroscopy, J. Sol-Gel Sci. Technol., 28 (2003) 5-14.

[198] C.J. Brinker, Hydrolysis and condensation of silicates - effects on structure, J. Non-Cryst. Solids, 100 (1988) 31-50.

[199] M. Davydova, A.D. Pereira, M. Bruns, A. Kromka, E. Ukraintsev, M. Hirtz, C. Rodriguez-Emmenegger, Catalyst-free site-specific surface modifications of

nanocrystalline diamond films via microchannel cantilever spotting, Rsc Advances, 6 (2016) 57820-57827.

[200] M.Y. Bashouti, M. Pietsch, K. Sardashti, G. Bronstrup, S.W. Schmitt, S.K. Srivastava, J. Ristein, J. Arbiol, H. Haick, S. Christiansen, Hybrid silicon nanowires: From basic research to applied nanotechnology, in: X. Peng (Ed.) Nanowires - recent advances, InTech, 2012.

[201] W.T. Choi, K. Oh, P.M. Singh, V. Breedveld, D.W. Hess, Wettability control of stainless steel surfaces via evolution of intrinsic grain structures, J. Mater. Sci., 51 (2016) 5196-5206.

[202] P.J. Launer, Infrared analysis of organosilicon compounds: Spectra-structure correlations, in: B. Arkles, G.L. Larson (Eds.) Silicon compounds: Silanes & silicones, Gelest, Inc., Morrisville, PA, 2013, pp. 175-178.

[203] W. Barthlott, C. Neinhuis, Purity of the sacred lotus, or escape from contamination in biological surfaces, Planta, 202 (1997) 1-8.

[204] A. Steele, I. Bayer, E. Loth, Adhesion strength and superhydrophobicity of polyurethane/organoclay nanocomposite coatings, J. Appl. Polym. Sci., 125 (2012) E445-E452.

[205] F.J. Wang, S. Lei, J.F. Ou, M.S. Xue, W. Li, Superhydrophobic surfaces with excellent mechanical durability and easy repairability, Appl. Surf. Sci., 276 (2013) 397-400.

[206] J. Wu, J. Li, B. Deng, H. Jiang, Z. Wang, M. Yu, L. Li, C. Xing, Y. Li, Self-healing of the superhydrophobicity by ironing for the abrasion durable superhydrophobic cotton fabrics, Sci. Rep., 3 (2013).

[207] L. Xiong, L.L. Kendrick, H. Heusser, J.C. Webb, B.J. Sparks, J.T. Goetz, W. Guo, C.M. Stafford, M.D. Blanton, S. Nazarenko, D.L. Patton, Spray-deposition and photopolymerization of organic-inorganic thiol-ene resins for fabrication of superamphiphobic surfaces, ACS Appl. Mater. Interfaces, 6 (2014) 10763-10774.

[208] I.S. Bayer, On the durability and wear resistance of transparent superhydrophobic coatings, Coatings, 7 (2017).

[209] N. Cohen, A. Dotan, H. Dodiuk, S. Kenig, Superhydrophobic coatings and their durability, Mater. Manuf. Processes, 31 (2016) 1143-1155.

[210] J.H. Zhi, L.Z. Zhang, Y.Y. Yang, J. Zhu, Mechanical durability of superhydrophobic surfaces: The role of surface modification technologies, Appl. Surf. Sci., 392 (2017) 286-296.

[211] I. Malavasi, I. Bernagozzi, C. Antonini, M. Marengo, Assessing durability of superhydrophobic surfaces, Surface Innovations, 3 (2015) 49-60.

[212] H.J. Lee, K. Park, Variable wettability control of a polymer surface by selective ultrasonic imprinting and hydrophobic coating, Colloid. Polym. Sci., 294 (2016) 1413-1423.

[213] F.Z. Chen, J.L. Song, Y. Lu, S. Huang, X. Liu, J. Sun, C.J. Carmalt, I.P. Parkin, W.J. Xu, Creating robust superamphiphobic coatings for both hard and soft materials, J. Mater. Chem. A., 3 (2015) 20999-21008.

[214] L. Jiang, Z.G. Tang, R.M. Clinton, V. Breedveld, D.W. Hess, Two-step process to create "roll-off" superamphiphobic paper surfaces, ACS Appl. Mater. Interfaces, 9 (2017) 9195-9203.

[215] S. Samal, Thermal plasma technology: The prospective future in material processing, Journal of Cleaner Production, 142 (2017) 3131-3150.

[216] G. Bonizzoni, E. Vassallo, Plasma physics and technology; industrial applications, Vacuum, 64 (2002) 327-336.

[217] I.B. Matveev, S.I. Serbin, N.V. Washchilenko, Plasma-assisted treatment of sewage sludge, Ieee Transactions on Plasma Science, 44 (2016) 3023-3027.

[218] M.S. Li, Z.P. Zhao, M.X. Wang, Controllable modification of polymer membranes by lddlt plasma flow: Membrane module scale-up and hydrophilic stability, Chem. Eng. Sci., 122 (2015) 53-63.

[219] V.E. Messerle, E.I. Karpenko, A.B. Ustimenko, Plasma assisted power coal combustion in the furnace of utility boiler: Numerical modeling and full-scale test, Fuel, 126 (2014) 294-300.

[220] R. Bagherzadeh, M. Montazer, M. Latif, M. Sheikhzadeh, M. Sattari, Evaluation of comfort properties of polyester knitted spacer fabrics finished with water repellent and antimicrobial agents, Fibers and Polymers, 8 (2007) 386-392.

[221] M.H. Ly-Chatain, S. Moussaoui, A. Vera, V. Rigobello, Y. Demarigny, Antiviral effect of cationic compounds on bacteriophages, Frontiers in Microbiology, 4 (2013).

[222] M. Montazer, F. Rangchi, Simultaneous antimicrobial, water and blood repellent finishing of disposal nonwovens using ctab and fluorochemical, Tekstil Ve Konfeksiyon, 19 (2009) 128-132.

[223] K. Nakata, T. Tsuchido, Y. Matsumura, Antimicrobial cationic surfactant, cetyltrimethylammonium bromide, induces superoxide stress in escherichia coli cells, Journal of Applied Microbiology, 110 (2011) 568-579.

[224] D. Goyal, G.S.S. Saini, R. Kumar, Role of surfactants on the optical, morphological and antimicrobial properties of silver nanoparticles, Materials Focus, 6 (2017) 96-100.

[225] M. Simoes, L.C. Simoes, M.J. Vieira, Species association increases biofilm resistance to chemical and mechanical treatments, Water Res., 43 (2009) 229-237.

[226] M. Ueno, F. Yokoya, Formulation of culture-medium for growth of microbes from the sugar-cane industry and use of cetyltrimethylammonium bromide as antimicrobial agent, Revista De Microbiologia, 25 (1994) 261-269.

[227] M.N. Valipour, F.C. Birjandi, J. Sargolzaei, Super-non-wettable surfaces: A review, Colloids Surf., A, 448 (2014) 93-106.

[228] S. Yang, X. Jin, K.S. Liu, L. Jiang, Nanoparticles assembly-induced special wettability for bio-inspired materials, Particuology, 11 (2013) 361-370.

[229] A.J. Worthen, L.M. Foster, J.N. Dong, J.A. Bollinger, A.H. Peterman, L.E. Pastora, S.L. Bryant, T.M. Truskett, C.W. Bielawski, K.P. Johnston, Synergistic formation and stabilization of oil-in-water emulsions by a weakly interacting mixture of zwitterionic surfactant and silica nanoparticles, Langmuir, 30 (2014) 984-994.

[230] L.F. Zhang, G.J. He, D.F. Ye, N.N. Zhan, Y.S. Guo, W.J. Fang, Methacrylated hyperbranched polyglycerol as a high-efficiency demulsifier for oil-in-water emulsions, Energy & Fuels, 30 (2016) 9939-9946.

[231] Z.K. Zhao, C.G. Bi, Z.S. Li, W.H. Qiao, L.B. Cheng, Interfacial tension between crude oil and decylmethylnaphthalene sulfonate surfactant alkali-free flooding systems, Colloids Surf., A, 276 (2006) 186-191.